Investigating the material characteristics and fatigue life of 18CrNiMo7-6 carburized steel pinions affected with grinding-induced burns

Rear axle driveline of heavy-duty trucks

Master Thesis

Sahith Kokkirala

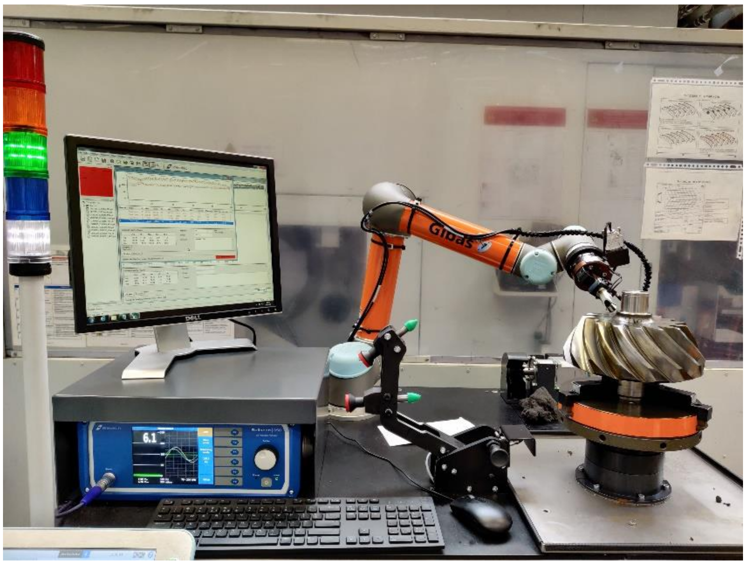

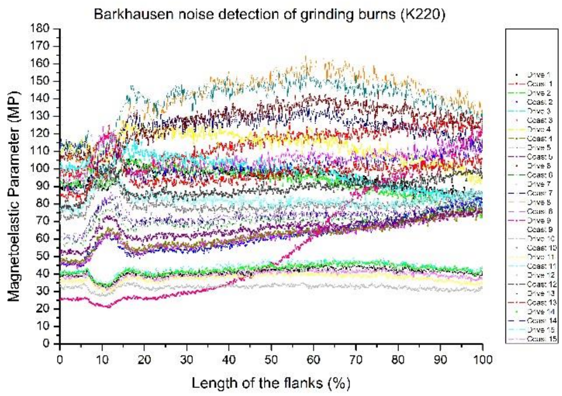

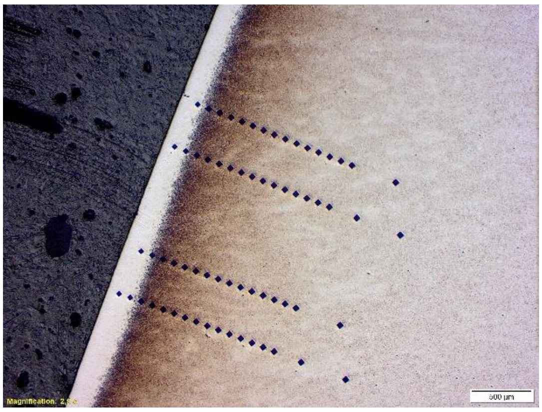

TU Delft

DAF
A PACCAR COMPANY

Investigating the material characteristics and fatigue life of 18CrNiMo7-6 carburized steel pinions affected with grinding-induced burns

Rear axle driveline of heavy-duty trucks

by

Sahith Kokkirala

in partial fulfillment of the requirements for the degree of

Master of Science

in Materials Science and Engineering at the Delft University of Technology, to be defended publicly

on **25 November, 2020**

Student number:	4893670
Project duration:	December, 2019 – November, 2020
Thesis Supervisors:	
Dr. Jilt Sietsma,	Delft University of Technology
Dr. Mark Van Drogen,	DAF Trucks NV
Ir. Han Spijkerman,	DAF Trucks NV
Thesis committee:	
Dr. Jilt Sietsma,	Delft University of Technology (Chair)
Dr. S.E. Offerman,	Delft University of Technology
Dr. Pina Mecozzi,	Delft University of Technology
Ir. Han Spijkerman,	DAF Trucks NV

TU Delft Delft University of Technology

DAF A PACCAR COMPANY

Acknowledgement

The success and final outcome of this project required a lot of guidance and assistance from many people and I am extremely privileged to have got this all along the completion of my project. I take this opportunity to express my profound sense of gratitude to all those who helped me through the duration of this work.

This thesis was done at the DAF Trucks NV for 12 months period. Firstly, I would like to specially thank my supervisor at the university, Prof. Dr. Jilt Sietsma for being supportive at every step throughout the period. Secondly, I would like to thank my supervisors at DAF Trucks NV, Dr. Mark Van Drogen and Ir. Han Spijkerman, for giving me the opportunity to work on this highly interesting and mentally stimulating project. Their inputs and technical insights at various stages, their support during the COVID -19 pandemic, their belief in me all played a huge role in me getting over the line with this study. The fun and insightful discussions we regularly had in the labs and online meetings are something that I'll hold onto and cherish for the entirety of my life.

I would like to specially thank the production engineers at DAF Trucks, Marcel Van Dooren and Giel Talsma, for their insight into the Barkhausen Noise, X-ray diffraction and pinions set up for the experiments. I would also like to thank Hans van Ettinger, Martie Buijtels from quality department for their help with the preparation of the samples and Theo Mossip, Maria Montero and Frank Druyts from central labaratory for their help with the Scanning Electron Microscope observation. I'd also like to thank the product development testing engineers Gijs Strang and Koen Willems for their support in the axle test. This project was also made so much more easier because of all the other staff including operators, production supervisors at the Engine plant who made working at DAF Trucks a highly memorable and enjoyable time. A special thanks to my friends in Delft for making my weekends memorable.

I would like to express my sincere gratitude to my parents and brother for always being there and supporting me through every decision I've taken in my life and for being a constant source of motivation. Finally, I thank God for blessing me with the required mental fortitude and direction to complete the thesis.

Sahith Kokkirala
Delft, November 25, 2020

Contents

List of Figures

List of Tables

Nomenclature

γ_R	Retained Austenite
BCC	Body Centered Cubic
BCT	Body Centered Tetragonal
BN	Barkhausen Noise
CCT	Continous Cooling Transformation
FCC	Face Centered Cubic
HRC	Hardness Rockwell C
HV	Vickers Hardness
Hz	Hertz
kgf	Kilogram force
M_f	Martensite finish temperature
M_s	Martensite start temperarure
MP	Magneto-elastic Parameter
NDT	Non Destructive Testing
nm	Nanometer
OM	Optical Microscope
RA	Retained Austenite
Rz	Surface Roughness
SAE	Society of Automotive Engineers
SEM	Scanning Electron Microscope
V_{pp}	Voltage peak to peak
XRD	X-Ray Diffraction

Abstract

Carburized steel grades are widely used in applications where high hardness at the surface is required in combination with good core toughness as well as high fatigue resistance. The process of carburizing lower to medium carbon steel can generally provide this combination of properties and has been practiced for several decades. Such steel is very essential in the vehicle power-trains. The carburized 18CrNiMo7-6 pinions are ground to obtain high dimensional precision after the carburization, quenching and tempering heat treatment process.

During the grinding process, thermal damage is developed due to the high localised heat energy at the contact zone of grinding wheel and pinion. The developed thermal damage is known as grinding induced burn. The burns are observed when temperature reaches above the tempering range (i.e. 210° C) and the intensity of the grinding-induced burn is in relation with the thermo-mechanical affects of the grinding process. The nital etch process is used to identify the burns using ISO 14104:2017 standard and the process detects using the discoloration developed on the burn site caused by the chemical attack. The information about the intensity of detected burns are not known in the nital etch method. However, the intensity of the grinding-induced burns can be measured using magnetoelastic parameter of Barkhausen Noise (BN) technique which functions in relation with the microstructure and stress state of the material.

The present study aims to investigate microstructural features of grinding-induced burns of varying BN intensities, to evaluate the service life testing of the thermally damaged pinions and the effect of varying grinding parameters on the generation of grinding induced burns. The microstructure characterization is done by optical microscope, vickers hardness, scanning electron microscope, X-ray diffraction and correlate the obtained results with the BN signals. The increased pinion speed and reduced grinding cycles are observed in the favouring of increasing localized heat input at the contact zone of grinding wheel and pinion causing the BN signals to increase. 3 samples of varying intensities of grinding induced burns are detected using BN and are characterized. The obtained results gave a good correlation with the barkhausen noise signals. As the heating rate at the grinding contact zone increased above the tempering range, the BN signals also increased due to the enhanced domain wall movement with the softer microstructure which is observed due to the retained austenite decomposition and carbon diffusion from the tempered martensitic phase. The further increase in temperature above the austenitization range led to the re-hardening burn. The freshly formed structure is brittle and hard untempered martensite at the surface surrounded by the softer tempering burn which might be detrimental during the pinion functioning. The axle test results of the tempered burn pinion observed the transformation of retained austenite to martensitic structure during the cyclic loading which eventually enhanced the surface properties by increase in hardness from 621 HV1 to 676 HV1 at 0.1 mm depth and generating -600 ± 6.6 MPa compressive residual stress due to the volume expansion. This transformation resulted in the grinding induced burn pinion to survive the axle test without failure.

Keywords— Grinding-induced burns, Carburized Steel, 18CrNiMo7-6 steel, Pinions, Tempered Martensite, Barkhausen Noise, Nital Etching, Vickers Hardness (HV), Optical Microscope, Scanning Electron Microscope, X-ray diffraction

1
Introduction

The driveline of commercial trucks typically consists of an engine, gear box, drive shaft, final drive and axle shaft. The final drive consists of pinion and crown gears to transmit the power flow with 90° turn from the drive shaft to the axle shaft where rear wheels are connected as shown in figure 1.1. The mechanical component drive pinion gear in the truck rear assembly has an important role in transmitting uniform and continuous rotational motion to the crown gear with the help of precised ground tooth without failure. The pinion is designed to have high load carrying capacity at higher torque with minimal size, weight and required to maintain high contact fatigue strength with high wear resistance as they are the most stress prone component of the truck [57]. Figure 1.2 illustrates the pinion gear and the components on it.

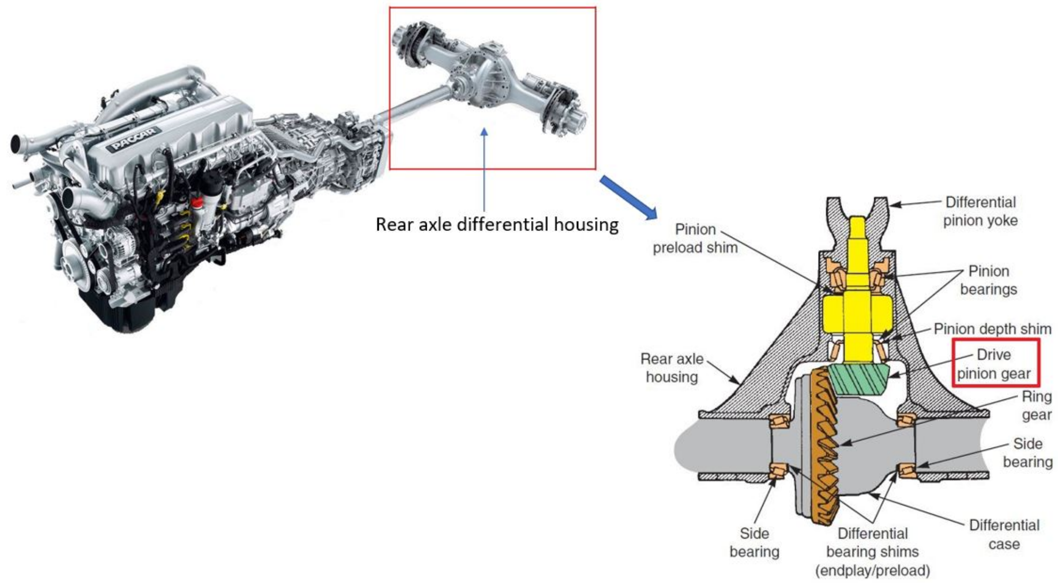

Figure 1.1: DAF Trucks driveline and rear axle differential housing (DAF Trucks website)

In accordance with the American Gear Manufacturers Association (AGMA), the ideal pinion should operate vibration-free with crown gear, good transmission ratio, high impact strength, excellent heat distortion control after quenching heat treatment during production, gear geometry in accordance with crown gear and optimum metallurgical quality [6]. To make these features possible for the smooth operation of the truck, case carburization is performed on the low carbon steel pinions followed by grinding process to achieve a soft tough core and a hard wear-resistant case to resist contact and bending fatigue failures [51].

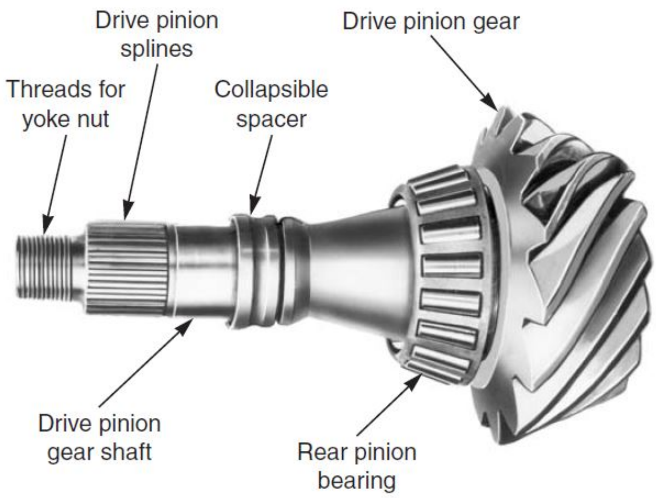

Figure 1.2: The Pinion gear focused in the present research (General Motors)

Carburized pinions are ground to obtain the high dimensional accuracy after the heat treatment and required surface roughness on the work piece. In the grinding process, abrasive grains of the grinding wheel interacts with the pinions to remove a few microns of depth from the surface by converting the high energy input into heat [47]. With the proper coolant flow, feed rate and depth of cut, low temperature grinding is observed on the pinion tooth surfaces. This precision finishing process offer smooth operation, excellent meshing effectiveness which runs more quietly and with higher transmission efficiency than pinions without ground. Due to these characteristics, they can handle high loads and used when large torques are required in rear axle differentials of the trucks. The grinding process eliminates the surface imperfections and increases the surface contact area and this increase in surface contact area can hold heavier loads and reduce premature failures [60].

In the grinding process due to the high localized heat energy involved per unit volume at the contact zone of grinding wheel and pinion tooth surface, local thermal degradation known as grinding burns is observed when the temperature of pinion tooth surface rises above the tempering temperature due to improper grinding parameters [24]. The observed grinding burns results in varying thermal damages, metallurgical transformations in the surface and sub-surface layers of the case-hardened pinions depending on the rise in temperature at the contact zone and deterioration of hardness, heat treated microstructure, wear resistance, fatigue strength of the component is observed as the unfavorable residual stresses are introduced into the pinion [1]. The potential issues of the grinding burn pinions are the premature failure and service unpredictability of the truck rear assembly.

The study focuses on the detection of pinion grinding burns using Barkhausen Noise (BN) technique, characterization of the grinding burns to study its material properties and perform the fatigue life testing on the pinions at rear axle test rig to understand the lifetime of a certain degree of grinding burn.

Firstly, detection of the grinding burns are performed using Stresstech Barkhausen Noise machine to evaluate the ground pinion. The elastic stresses and microstructure of the material influences the Barkhausen Noise signal. An amplitude signal is emitted in the end referred as Magnetoelastic Parameter (MP) by the BN sensor. Magnetoelastic interaction is the interaction between elastic properties and domain structure/magnetic properties of the material. With the help of increased or decreased amplitude of Barkhausen Noise MP values, the tempered and re-hardened grinding burns can be detected. The non-destructive detection machine helps to vary the grinding parameters to lower the heat input into the material for the next-in-line pinions to be grinded. The understanding of safe range of Barkhausen noise signals is to be analyzed with required material characterization technique's.

Secondly, characterization techniques like Vickers hardness, optical microscope, X-ray diffraction, Scanning electron microscope is to be performed on the varying degrees of grinding burns to understand its degradation process. As of now, there is only qualitative understanding of correlation between the BN signal and the material properties. There is a need to evaluate if there is way to quantitatively correlate the BN signals and material hardness, Residual stresses and retained austenite fractions.

Finally, fatigue is the dominant failure type in gears and the gear loading capacity is basically limited by different failure modes. In rotating bodies (Crown, pinion gears) high cyclic contact pressure loads develop and simultaneous rolling and sliding is observed due to the relative motion between them. The initiation of micropits in the burn surface is studied to analyze the failure initiation.

In the next chapter, the theoretical background on the carburized steel heat treatment is studied to understand the phase transformation from the low carbon steel to the case carburized steel. The production process of pinions at DAF Trucks is discussed from the raw forged to the final grinding finish process. The focus is next given to the grinding process and its behaviour in creating the grinding burns. In chapter 3 the problem statement and research questions are presented, along with the research objectives. Chapter 4 explains about the methodology of the experiments performed. The results and discussions are reported in chapter 5. Finally conclusion and future recommendations are focused in chapter 6.

2

Theoretical Background

The theoretical background aims to introduce the reader to grinding burns mechanism in pinions by discussing the various related subjects. Firstly, an introduction to the case carburized heat treatment process, phase transformation and manufacturing process of pinion will be discussed followed by the main topic the grinding process. The second section of the background focused on the mechanism and creation of grinding burns with respective to the microstructural effects. Additionally, distinction between the mechanical and thermal aspects of the grinding process will be made. Thirdly, the Barkhausen Noise detection technique of the grinding burns will be investigated and the detailed study is made. Finally, the pinion failure modes are discussed and the effect of residual stresses and retained austenite due to the grinding burns on the initiation of the micropitting are studied. This will give the reader on overview of the grinding burns and it's detrimental effects.

2.1. Carburized Pinions

Carburization is a notable diffusion-driven thermochemical process of enhancing the highly stressed pinion surface properties used in the heavy trucks driveline [52]. After the forging and machining fabrication, low carbon steel (< 0.25% C) pinions are carburized to enhance the surface properties by converting into a composite material consisting of high carbon steel (0.6% C - 1.5% C) case and low carbon steel core. The improved surface will be wear resistant and develops high fatigue strength with ≈50 to 60 HRC whereas the soft or ductile core with ≈40 - 45 HRC helps to prevent catastrophic failure of the pinion like tooth root breakage from the impact loading [60]. It is thus important to understand the general background of carburization, quenching and tempering heat treatment process as it gives a good initiation point to understand the microstructure features and manufacturing process of DAF Trucks pinions.

Table 2.1 shows the chemical composition of the **18CrNiMo7-6** steel forged pinion received from the supplier. The research is focused on the grinding burn characteristics of the carburized steel version made for the pinions to withstand the failures.

Steel grade	**C%**	**Si (max)%**	**Mn%**	**P (max)%**	**S%**	**Cr%**
18CrNiMo7-6	0.176	0.40	0.50-0.90	0.025	0.005-0.020	1.50-1.80
	Mo%	**Ti%**	**Cu (max)%**	**Nb (max)%**	**Sn (max)%**	**Sb (max)%**
	0.25-0.3	≤ 0.005	0.25	0.040	0.030	0.006
	O (max)%	**Al%**	**Ni%**	**N (p.p.m)**		
	0.0025	0.02-0.05	1.40-1.70	110-150		

Table 2.1: Chemical composition in wt% of 18CrNiMo7-6 steel pinion

2.1.1. Carburization, Quenching and Tempering

To transform the low carbon steel pinions to carburized pinions, the pinions will undergo carburization, quenching and tempering heat treatment to produce the final desired product with the required material properties. This section gives a clear understanding on the basics of pinion heat treatment process. Figure 2.1 illustrates the example of pinion heat treatment process with temper-

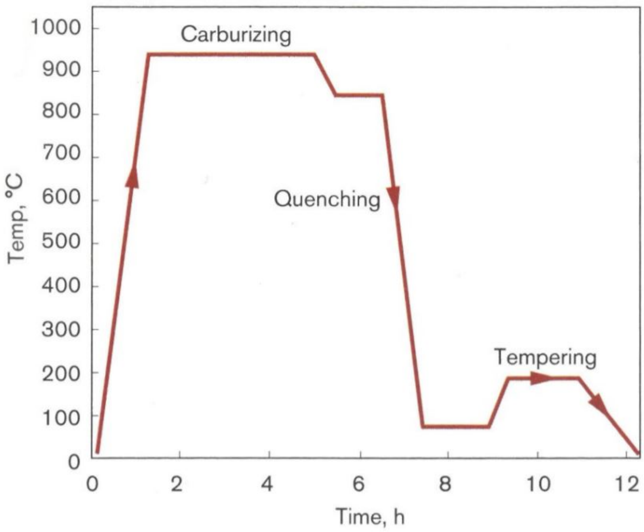

Figure 2.1: Pinion heat treatment process [56]

ature and time.

Carburizing

The first step of case hardening or carburizing is to place the pinions in the furnace and heat it above the austenitizing temperature around 980°C, to obtain the high carbon solubility. The body-centered cubic (BCC) ferrite/pearlite structure transforms to face-centered cubic (FCC) austenite, and hence the structure has homogeneous single phase containing all the carbon. During the gas carburization, the pinions are subjected to the high carbon atmosphere (i.e 0.8% C - 1% C) above austenitization temperature through dissociation of endothermic natural gas (CO). Carbon diffuses into the pinion surface and interacts with the FCC lattice structure of the steel [34]. The following process not only dependent on carbon concentration inside the furnace but also highly dependent on temperature and time as given in equation 2.1 [5] [27]

$$d = \phi\sqrt{t} \tag{2.1}$$

where d = total case depth in inches, t = carburizing time in hours at temperature with saturated austenite at the surface and ϕ = proportionality factor of material that varies with the carburizing temperature. The value of ϕ is approximately 0.025 for low carbon steels which are gas carburizing at 980° C. Figure 2.2 illustrates the carburizing and diffusion process.

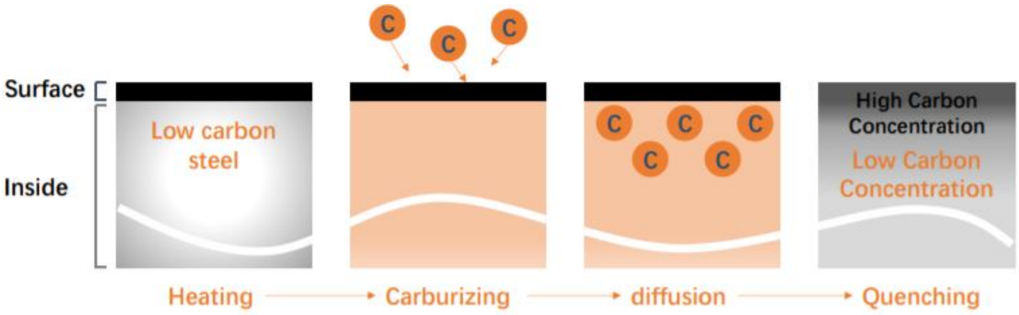

Figure 2.2: Carbon diffusion process in carburizing and quenching [33]

The 2 stage boost-diffuse carburization process illustrated in the figure 2.3 is the most typical and provides good control of the carbon profile on the surface. In the boost stage, high carbon concentration at the surface is developed and during the diffuse stage, the carbon potential accelerates the diffusion into the surface [17]. The result of this two stage process is a reduction of the carbon concentration at the surface while increasing the depth of carbon absorption. The initial carbon percentage on the surface is around 1.36%. As the diffusion process starts, the carbon potential on the surface deducts to around 0.6 - 0.75% but has increased case depth than the initial condition. The oil temperature in the quenching process determines the case hardness, microstructure, and surface uniformity. [43].

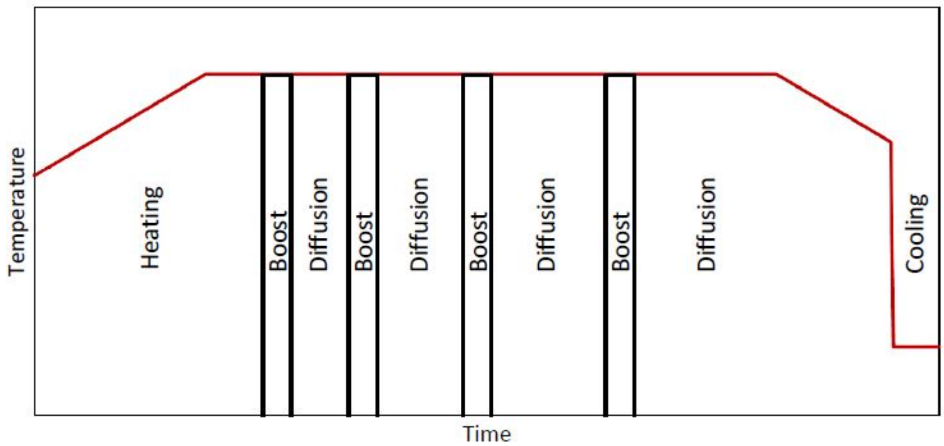

Figure 2.3: Boost and diffusion process [17]

Quenching

Quenching is the process of rapidly cooling the components from the austenitizing temperature, typically from 860°C for steel. In the industrial furnaces, the temperature is reduced from 980°C to 860°C in the time span of around 120 minutes and kept hold for 10 minutes. This is done to reduce the quenching distortion and thermal cracking of heavy components like pinions. To transform the material to martensite, the cooling rate is to be high enough compared to bainite and ferrite and it also depends on the grain size and chemical composition of the steel of the parent FCC austenite phase[50]. Oil is used as the quenching medium in the industries to reduce the cracking probability for large components as the martensite start (M_s) to martensite finish (M_f) transition is slow when compared to water quenching, furnace cooling and this behaviour delivers the required hardness, residual stresses, retained austenite values from the case to core [28]. In the first stage when the pinions are quenched in oil, the surface temperature of the pinion is so high that the oil begins to evaporate and generates a blanket of vapor or thin film at the material surface [34]. At this particular stage, radiation is the source of heat transfer, which is slow. The next stage is the boiling stage and during this stage, the thin blanket breaks-down and bubbles nucleation begins, which increases the heat transfer [34][28]. The bubbles are easily carried out by the agitated quenching oil, which prevents the soft spots on the gears. The convection is observed only when the surface temperature get below the boiling point of the oil [28]. The oil quenching provides a enough cooling rate to produce a BCT martensite case layer and core with low carbon martensite or lower bainite. High cooling rates may lead to high retained austenite fraction or quench distortion [33]. Steels are said to have a good hardenability when the martensitic microstructure is observed even for a low cooling rate [42].

Tempering

Carburized pinions are often given low temperature tempering after quenching, ranging around 190 to 200° C for 2 hours to minimize the internal stresses. The tempering temperature has an effect on surface hardness and core hardness. As the tempering temperature increases, the case hardness decreases due to the carbon diffusion from the BCT martensite. The martensite gets it properties like hardness and brittle nature from the strain-induced by the interstitial atoms, which distorts the metal lattice [60]. So to obtain the required industrial properties, the hardened gears are heat treated (tempered) to improve ductility, toughness which delays the fatigue failures. The carbon gradient across the case to the core attained after the carburization process resulted in variation of microstructure in the pinions. The microstructure varies from the surface to the core with the twinned plate martensite on the surface due to the high carbon levels and the lath martensite in the low carbon range [25]. During the tempering of case hardened pinions, each of these different carbon levels microstructures from the surface to the core responds differently resulting in property changes throughout the case depth. An in-depth understanding of the microstructural processes taking place upon tempering of martensite becomes thus of fundamental priority. From the literature, the tempering of martensites are divided into 5 steps [8]:

Tempering stage	**Phenomenon**	**Temperature range**
Pre-Precipitation	Cluster formation + Segregation	until 80°C
Stage 1	Precipitation of ϵ or η Carbides	80°C - 200°C
Stage 2	Transformation of γ_R	200°C - 300°C
Stage 3	Precipitation of θ	300°C - 400°C
Stage 4	Coarsening, recovery, re-crystallization	500°C - 700°C

Table 2.2: Stages of Tempering in ferrous martensite

- **I) Pre-precipitation stage** : The initial stage begins in the temperature range between ambient room temperature and 80°C. The process involves with the slight decrease in material volume. At this initial stage, the carbon atoms are segregated to grain boundaries, lattice defects and this subsequently involves the carbon atoms clustering in these regions [41].

- **II) First stage of tempering** : The range of temperature of this stage to occur is between 80 and 200°C and is associated with the transition carbide precipitation (first discovered by Jack [40] and referred to as ϵ carbide and later as η carbide by Nagakura [8]) homogeneously throughout the martensite structure. The precipitates formed are also called primary hardening as they enhance the strength of the material by forming fine carbides [53]. Due to the increase in temperature, the formed precipitates tends to reduce the material strength as they appear to coarsen. The morphology of carbides are reported to look like platelike or rodlike and suggested that the alloy composition might effect it's shape. The ϵ carbide nucleation mechanism is not well established and that the iron atoms movement produced by the interstitial carbon atoms favouring the nucleation as a possible mechanism. [42].

- **III) Second stage of tempering** : The range of temperature of this stage to occur is between 200 and 300°C. This stage is associated with the retained austenite (γ_R) transformation to ferrite (α) and an orthorhombic cementite (θ, M_3C carbide) with different tempering times and temperatures (Figure 2.4). After tempering until 1 hour at 250° C, the retained austenite transformation is completed. At the austenite/martensite interface the decomposition begins. In high alloy steels, the decomposition is not observed during the tempering as the γ_R is stabilized [65].

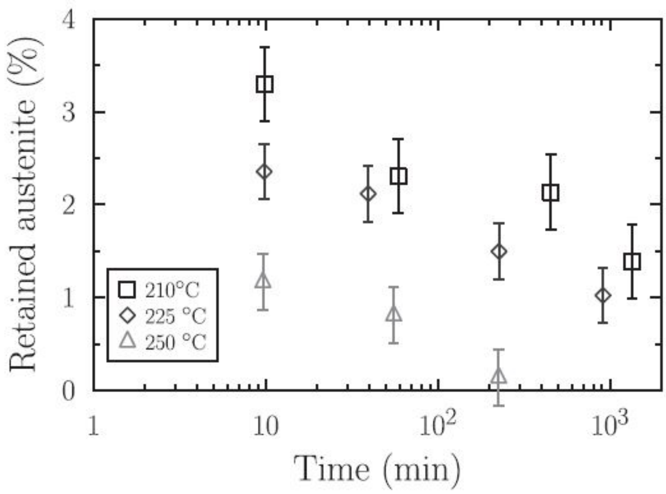

Figure 2.4: Retained austenite volume fraction, measured by X-ray diffraction, as a function of time upon tempering at indicated temperature a 0.3 wt.%C lath martensite

- **IV) Third stage of tempering** : The range of temperature of this stage to occur is between 300 and 400°. The η- Carbides formed dissolve as the precipitation of cementite begins and contribute carbons atoms to the θ particles. The initial platelike cementite morphology tends to coarsening and spheroidisation of cementite particles with the increase in temperature [53]. This phenomenon is known as Oswald ripening where the smaller particles shrink and disappear in the matrix for the selective growth of larger θ particles. The hardness is reduced due to the subsequent morphology change in the θ particles during tempering. High slowdown effects on the tempering rate by the alloying elements is observed and retard the coarsening of the θ particles until certain time.

- **V) Fourth stage of tempering** : The cementite particles dissolution is associated in the fourth stage of tempering. This process occurs at high temperature range 500° - 700° C as it is a diffusion controlled. Due to the recrystallization process, the martensite boundaries are replaced by the ferrite equiaxed grains [8]. In the higher carbon content steels, the final process is the gradual ferrite growth and the cementite dissolution.

Figure 2.5 illustrates the hardness behaviour of varying carbon content which is tempered for 1hr from 100 - 700° C. As stated above, the hardness decreases from the first stage to the final stage of tempering due to diffusion observed at respective stages.

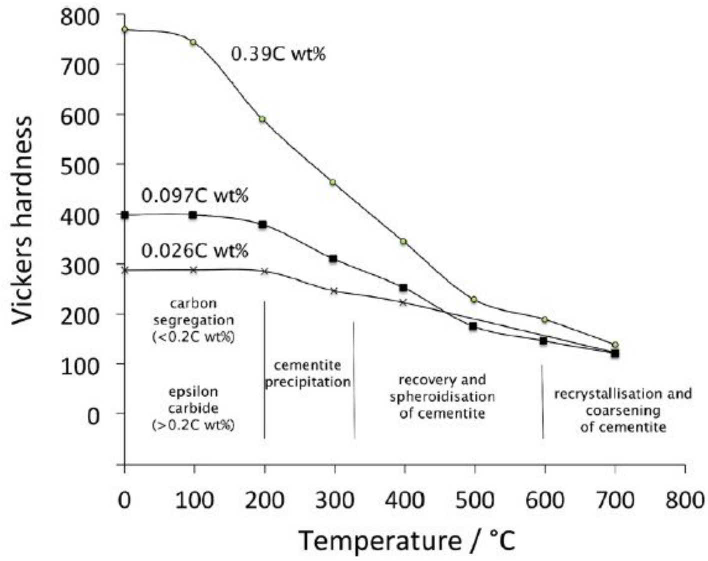

Figure 2.5: Vickers hardness with tempered time 1hr at 100-700° C [21]

2.1.2. Austenite to Tempered Martensite phase transformation

This subsection explains about the microstructural transformation from ferrite/pearlite → Austenite → Tempered martensite. The forged ferrite/pearlite microstructure is heated above austenitization temperature in the heat treatment furnace and martensite (BCT) microstructure is formed by rapidly cooling from the austenite (FCC) phase. This process is termed as quenching as explained earlier. As the austenite phase has high carbon solubility (Slightly above 2%), the carburization process is performed in this phase [25]. The high solubility of carbon in austenite when compared to ferrite makes the possibility of martensite structure in carbon steel. As the cooling rate is high, the carbon atoms don't have time to diffuse, this makes it as "Diffusionless transformation" [60]. The carbon atoms are present in the interstitial positions of the parent austenite (FCC) phase and remain trapped in the martensite. Steel martensite is therefore a supersaturated solid solution of interstitial carbon atoms in a body centred tetragonal metal lattice consisting of iron and other alloying elements [20]. The tetrahedral distortion of the martensite is caused as the interstitials favoured to dominantly occupy only one form of octahedral interstices. Martensite hardness depends predominantly on solution hardening effect of carbon which increases with increasing of carbon content. Figure 2.6 represents the austenite to martensite transformation.

Upon cooling to the M_s temperature, the initial martensite plates or lath are formed depending on carbon concentration. In low carbon steels M_s is high and depends on the alloy composition, but as the carbon percentage increases M_s temperature decreases progressively. Also the Cr, Si and Ni influence the M_s temperature [25] [42] [60]. The martensite crystals grow swiftly in steel at nearly the speed of sound before they encounter an obstacle like prior austenite grain boundary once the nucleation barrier has been overcome [8]. Below the M_f temperature, further cooling does not effect in increase of martensite fraction. Figure 2.7 represents the martensite fraction changes with

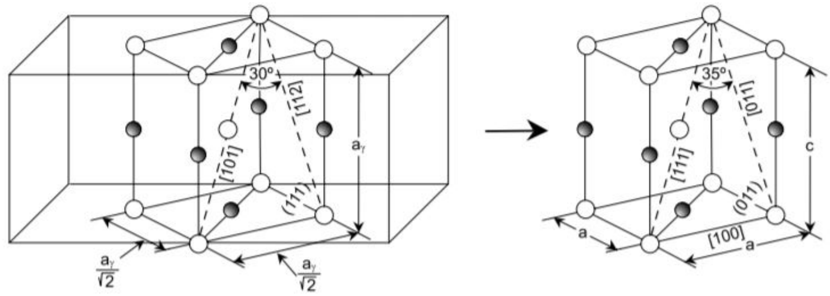

Figure 2.6: Schematic representation of the $\gamma \rightarrow \alpha'$ correspondence according to Bain Iron atoms are indicated by white spheres while possible interstitial sites for carbon atoms are indicated by grey spheres [14]

temperature during cooling in steel. It also illustrates the possible microstructures with varying cooling speeds. Particularly in medium and high carbon steels, due to the low M_s some fraction of austenite is retained below M_f. The retention of austenite is attributed to the high stresses between the martensite plates that form, which tend to suppress growth or thickening of existing plates [8].

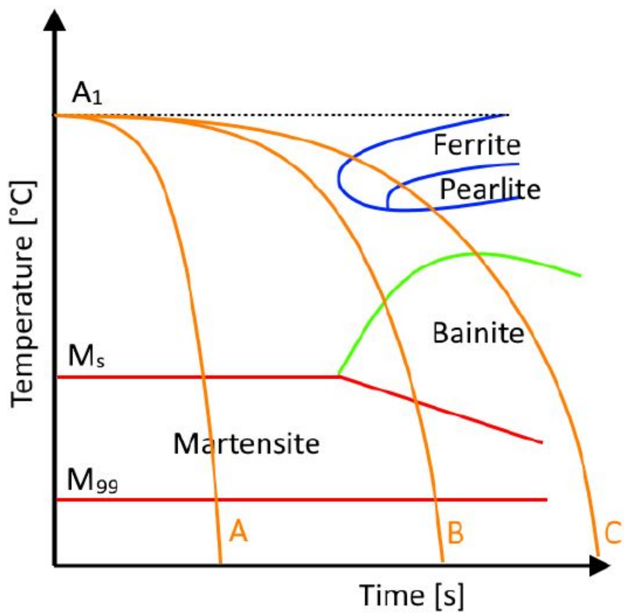

Figure 2.7: A schematic continuous Cooling Transformation (CCT) diagram for steel [62]. The cooling trajectories are indicated in orange, while the martensite, ferrite/pearlite and bainite regions are indicated in red, blue and green respectively. The cooling rate decreases as the cooling trajectory reaches further to the right

Koistinen and Marbuger [38] determined an empirical equation connecting both martensite volume fraction and temperature below M_s. After observing the retained austenite values in various alloys at different quenching temperatures, both the authors demonstrated that the transformed martensite volume fraction is a function of the difference between the M_s temperature and the lowest quench temperature according to the equation 2.2.

$$V_\alpha(T_q) = 1 - exp(-\alpha(M_s - T_q)) \tag{2.2}$$

V_α = Volume fraction of martensite, M_s = Martensite start temperature, T_q = lowest quench temperature reached, $\alpha \approx 0.01111$, regardless the chemical composition. But the recent transformation kinetics however showed that α has to be a function of composition [22].

The M_s temperature of an alloy depends on its chemical composition [63]. The following empirical dependence of the M_s temperature on alloying substances was provided by Andrews [4].

$$M_s(^\circ C) = 539 - 423x_C - 30.4x_{Mn} - 17.7x_{Ni} - 12.1x_{Cr} - 7.5x_{Mo} \tag{2.3}$$

The elements symbol x_i represent the weight percentage of the particular composition and the dominant effect of carbon is observed on the M_s temperature.

The transformation of martensite is achieved by a crystallographic misfit of iron(Fe) and carbon (C) atoms between the parent austenite lattice and the growing martensite. Due to this misfit, high shear stresses resulted at the interface of the martensite growth [41]. At this growing interface, dislocations are formed to accommodate these shear stresses. Therefore, a high density of dislocations is observed in a fully martensite microstructure.

Martensite generally classifies between plate and lath martensite which depends on the carbon percentage, alloying composition and transformation process. Plate martensites contains both fine mechanical twins and dislocation tangles and favoured to have a low M_s due to its high carbon content (eg, $M_s \leq 100^\circ$ C). Lath martensites, on the other hand contain few twins and high dislocation densities and likely to have high M_s due to its low carbon content ($M_s \geq 300^\circ$ C) [26]. Plate and lath martensites are formed through an athermal process and the fraction of martensite volume is only a dependent of temperature but not time. Figure 2.8 represents the morphologies of plate and lath martensite.

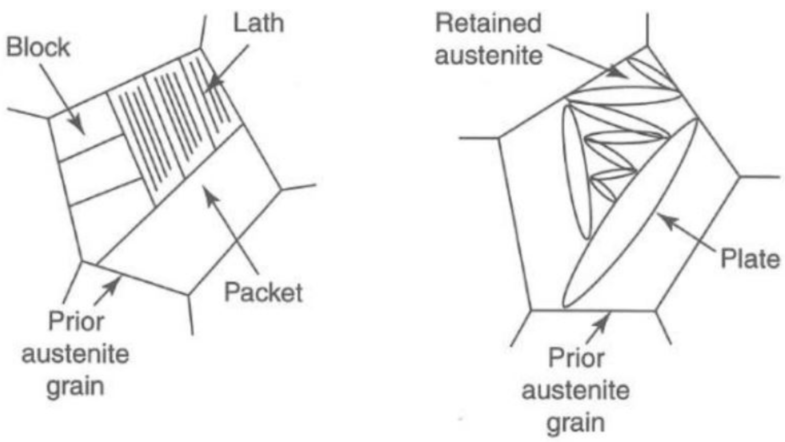

Figure 2.8: Schematic plate and lath martensite morphology [26]

Several factors contribute to the brittleness of martensite. Firstly, the shear transformation from austenite to martensite causes a high dislocation density. Plasticity upon subsequent mechanical loading will remain low since the motion of dislocations is hindered by the high density of other dislocations and interstitial carbon in the BCT lattice [20]. Secondly, straining of the BCT lattice is required to accommodate carbon at its octahedral interstitial sites. This, in addition to shearing during the martensitic transformation, can lead to residual stresses in the material.

2.1.3. The microstructural features of pinions

After understanding the whole case hardening process of steel in the sections above, this section deals with the heat treatment process and the obtained microstructure features of pinions at DAF trucks. The forged raw component has Pearlite-Ferrite annealed soft microstructure and the chemical composition is mentioned in the table 2.1 above. After the milling operation, the pinions are sent to furnace to harden the structure with carburization technique by producing a case hardened layer and subsequent quenching is done.

Alloy	**Carburization Heat treatment**	**Furnace cooling**	**Oil quenching**	**Tempering**
18CrNiMo7-6	980°C in 50 min hold for 40 min	860°C in 120 min hold for 10 min	80°C	210°C for 1 hr and Air cooled

Table 2.3: Heat treatment process of pinions

Table 2.3 gives an overview of the heat treatment process of the pinions at DAF Trucks. The pinions are heated in the furnace until 980°C, so that the soft Pearlite-Ferrite structure completely transforms into an austenitic (FCC) single phase and then kept hold at >980°C for 40 min. Carburization process is done by endothermic natural gas by introducing carbon into the surface due to the austenite high carbon solubility and produce case hardened layer with 0.68%C at the surface and 0.35% at the end of case depth as shown in Figure 2.9. Then the pinions are cooled to 860°C in 120 min and kept hold for 10 min at that temperature to produce a case depth of 1.9 mm. Pinions are then oil quenched at 80°C. The fast cooling oil quenching creates martensite layer and this transformation increases the volume of the material. During this cooling process, the austenite (FCC) structure will transform to martensite (BCT) crystal. This rapid transformation doesn't give enough time for the carbon trapped in the BCT to diffuse which causes high distortion in the structure and this process makes the steel hard and brittle [65].

The pinions are tempered until 210°C and kept for 60 min to relieve the internal stresses, increase the toughness and then they are air cooled [8]. This tempering temperature is in between stage I and stage II phenomenon. During the tempering process as mentioned above, the trapped supersaturated carbon(C) atoms move out of the spaces between the iron(Fe) atoms in the martensite to form the α BCC structure with epsilon carbides. The structure still looks similar to martensite as it is a low tempering process below 250°C. Due to this movement of carbon atoms, the strain within the martensite is relieved and this process also transforms the fraction of retained austenite present into martensite upon cooling. At the expense of reduced strength, the tempering results in an increase of the steel toughness [42].

The final product after the turning, milling, heat treatment and grinding operations has a case carburized tempered martensite microstructure with hardening depth about 1.9 mm (550 HV) and carbon percentage varying from 0.68% at the surface to 0.35% at 1.9 mm. Figure 2.9 illustrates the variation of carbon concentration from the surface to the core. The hardness is between 58 and 62 HRC until the depth of 1.1 mm from the surface. The hardness evaluation is done using Vickers hardness (HV1) beginning from 0.1 mm depth and then the results are converted into HRC values. The tempered martensite microstructure in the case hardened layer will improve fatigue life during the operation of pinions when compared to the untempered brittle martensite.

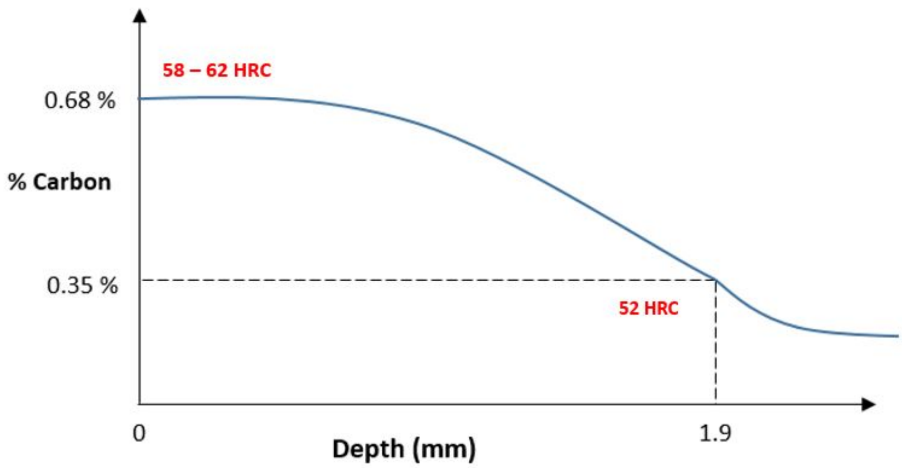

Figure 2.9: % of Carbon in case hardening depth of 18CrNiMo7-6 Low carbon steel

2.1.4. The manufacturing process of pinions at DAF Trucks

The overview of the production process from the raw material to the finished case hardened product is illustrated in figure 2.10. The forged pinions are centered and drilled at the top and bottom of the pinion shaft to perform the turning operation. The turning operation reduces the diameter to the specified dimension and gives a smooth, shiny finish. The spline rolling is done at the pinion shaft to assemble the differential pinion yoke. The CNC teeth milling is done on the pinion to produce the tooth flanks. As this operation produces rough edges on the tooth flank, deburring is done to remove those rough and sharp edge marks. The deburred pinions are heat treated in the oven and washed to make the product clean and to prevent corrosion. After the heat treatment, metal blasting helps to mechanically clean the surface to remove oil and dirt contaminants on the pinions. Hard turning operation is done to reduce distortion caused due to heat treatment and give a required dimension on the pinion shaft. Grinding operation is done to manufacture a precise tooth dimension and required surface roughness to reduce friction on the tooth flanks.

Figure 2.11 illustrates the pinions after the major manufacturing steps at DAF Trucks plant. The soft machining is performed during the ferrite/pearlite microstructure and hard machining after the heat treatment comprising tempered martensite, retained austenite. After the whole soft and hard machining process, tooth profile check is done to find the errors in the tooth gap and any dimensional instability. The pinion is then checked for any grinding burns with the help of Barkhausen noise and then etched with 4% HNO_3 + 96% ethanol to see the visibility of the burn. Finally, the product is then washed again to prevent the corrosion and delivered.

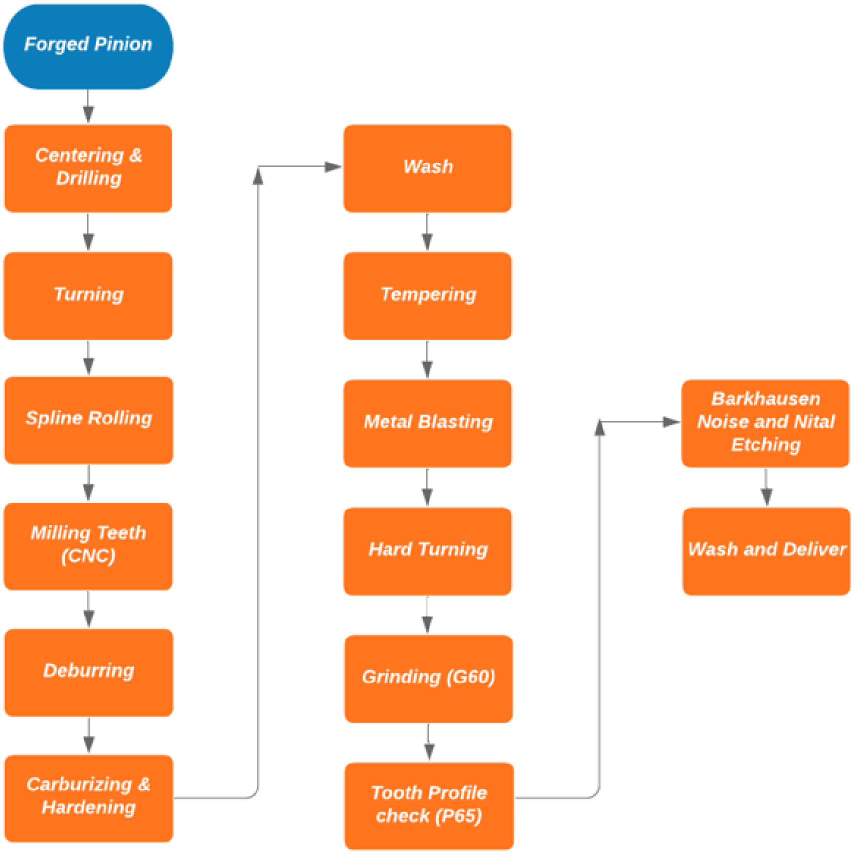

Figure 2.10: Production process of the pinion from the forged raw material to the final case hardened structure

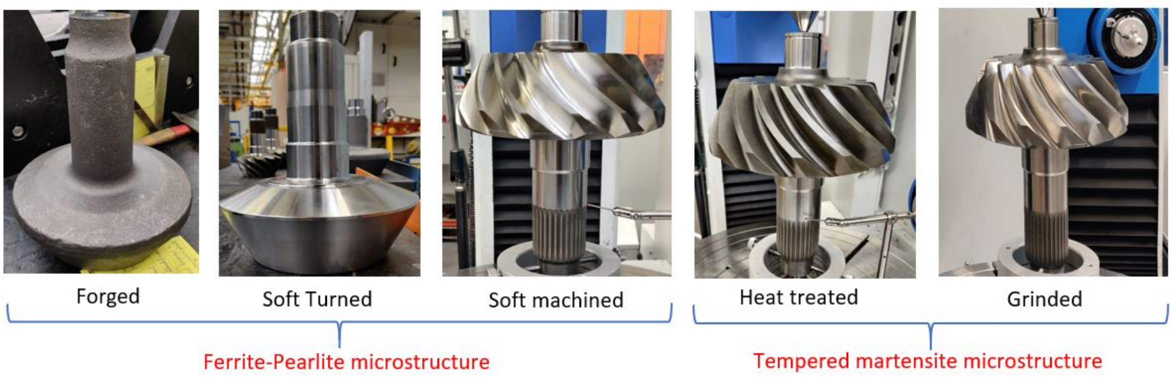

Figure 2.11: Pinions after the major manufacturing steps

2.2. Grinding

As the main focus of the thesis work is to investigate the effects of grinding burns on the failure of carburized pinions, grinding operation is given much importance to understand it's behaviour on the material properties. Gear grinding is a precision finishing process which uses 3M Cubitron II ceramic aluminium oxide abrasive particles to remove small variations on the gear teeth. Due to the precise gear geometry after the grinding operation, the ground pinions offer smooth operation, excellent meshing effectiveness which runs more quietly and with higher transmission efficiency than pinions without ground [64]. Due to these characteristics, they can handle high loads and used when large torques are required in rear axle differentials of the trucks. The grinding process eliminates the surface imperfections and increases the surface contact area. This increase in surface contact area can hold heavier loads and reduce premature failures. Generation grinding in the spiral bevel gear machining is a discontinuous grinding process and the process is done tooth by tooth. Figure 2.12 is a generation grinding process done on pinions at DAF Trucks.

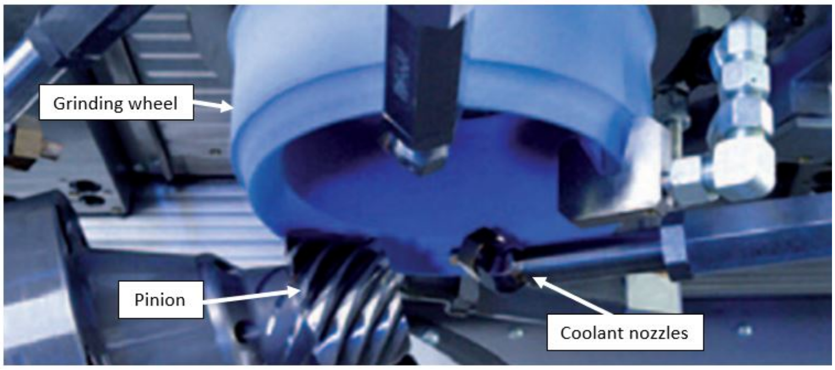

Figure 2.12: Generation grinding by 3M Cubitron II grinding wheel (3M Company)

In the manufacturing process of pinions as discussed in the above section, the grinding operation is performed during the final stage to produce high accuracy components with low surface roughness (2μm - 6μm) , required topography and tooth profile [12]. The grinding-induced burns caused during the final manufacturing stage develop a major concern which affects the pinion's performance, residual stresses and retained austenite therefore the fatigue strength [67]. Low-temperature grinding helps us to improve fatigue life and compressive residual stresses. This is due to the mechanical grinding force applied to the surface which has a similar effect to shot peening. Conversely, localised high-temperature gear grinding produces tensile residual stresses that reduce fatigue strength [58].

2.2.1. Theory

Figure 2.13 illustrates the process of grinding. When a piece of grit is brought into contact with the workpiece it starts by rubbing a short distance on the surface as the normal force (F_n) builds up. When the pressure is high enough, the grit plows down into the material and pushes the material in front of it. This pushing produces shear forces in the material. Finally a chip starts to form and the grit now cuts through the material. The negative rake angle gives a stronger edge to the grit, but builds up higher shear forces in the workpiece. The cutting itself is done by thousands of grits bonded together into a grinding wheel, the matrix holds the grits together. The matrix is adjusted so that it is strong enough to hold the grits but still porous enough to enable transport of cooling fluid to and chips away from the working area [37]. The interesting nature of the grinding wheel is it's self-sharpening property. When the grits break, the newly created edges on the grit makes the grinding

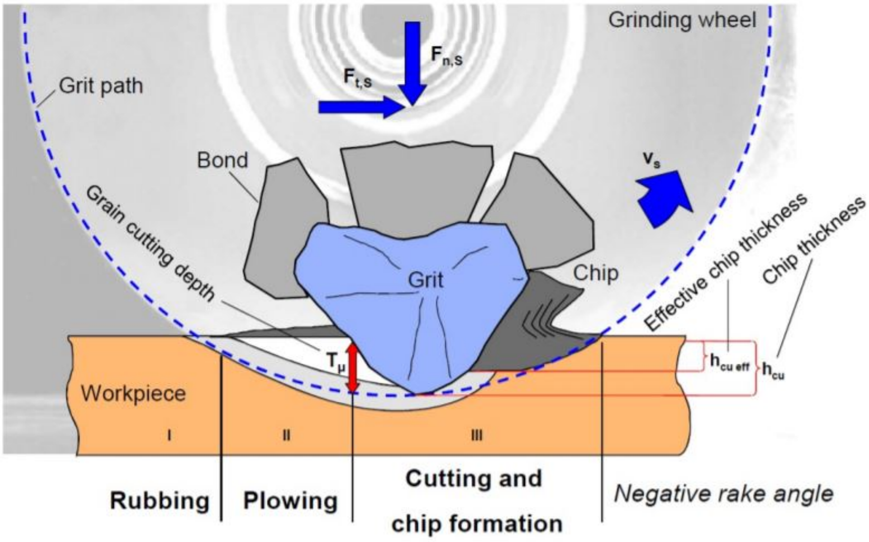

Figure 2.13: Grit removing a chip from the workpiece. The three phases rubbing, plowing and cutting are demonstrated [37]

easier and effective. However, to maintain the control over the grinding process, dressing is done on the grinding wheel. this will help to control the parameters like surface finish, power consumption, forces and temperature at the contact of the wheel and workpiece. A diamond material is used to dress the grinding wheel to remove the worn-out grits [47]. The main function of the bonds covering the grit is to hold the grits together until they are dulled enough and removed.

2.2.2. The effect of process variables on the grinding operation

The main process variables during the grinding operation includes feed rate, cutting speed, grinding wheel and coolant fluid. During the grinding process, there will be a compromise between the quality of the product and the productivity in the given time[49]. There is a limited knowledge on the combination of all process variables interaction on the grinding parameters. Each process variable is studied individually to understand its effect on the surface roughness impact, hardness and residual stresses [66].

Feed Rate

To obtain the higher productivity, increased material removing rate is performed on the workpiece with the combination of feed rate and infeed. This impacts a lot on the surface and residual stresses of the workpiece due to the higher loads subjected to the individual abrasive grit of the grinding wheel on to the workpiece. This generates an increased temperature and impacts the wear of grinding wheel which ultimately affects the ground pinion quality [66].

Cutting speed

The cutting speed which centrally affects the final surface finish of the pinion has very high significance. Research shows that when there is a much abrasive grain interaction on the pinion due to high cutting speed of the wheel, a decrease in surface roughness is observed due to the lower ploughing height of the grains [10]. The cutting speed affects the depth of cut, cutting forces and mechanical stresses on the abrasive grains. Even though the surface finish is enhanced with the high cutting speed, a higher wear rate is observed on the grinding wheel which eventually increases the thermal stresses[37].

Grinding wheel

The shape and geometry of the abrasive grains on the grinding wheel is very important for the heat dissipation process. There are many materials like silicon carbide, cubic boron nitride, aluminium oxide are used for the abrasive grains depending on the application of the product requirement. For the current study, 3M Cubitron II Precision Shaped Grains (PSG) made up of sintered aluminium oxide is focused. Figure 2.14 illustrates the shape of the grains. The distinguished feature of the grinding wheel is the triangular shaped grains. The specific triangular shaped geometry minimizes the elastic and plastic deformation zones at the contact. The heat conduction on the workpiece is much lowered compared to the irregular shaped grains as shown in figure 2.15 [3].

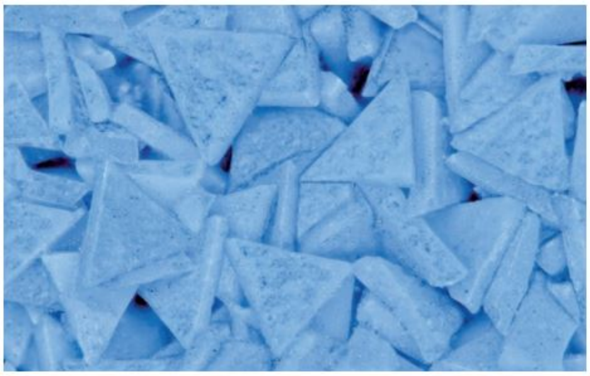

Figure 2.14: 3M Cubitron II sintered aluminium oxide PSG [3]

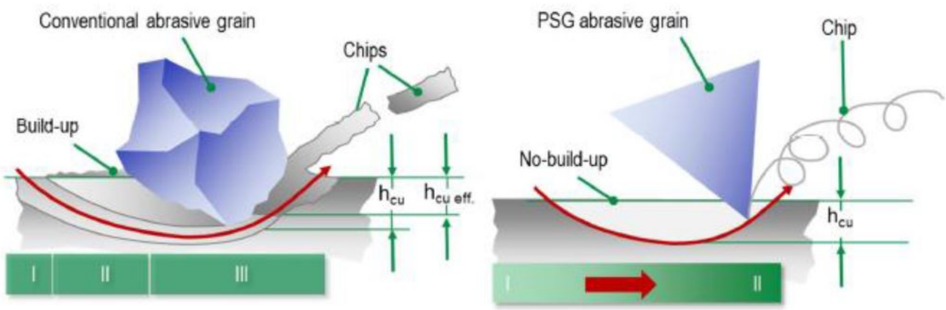

Figure 2.15: Comparison between the conventional and PSG chip formation and the build up [3]

Coolant fluid

To limit the heat generation at the contact zone between the pinion and grinding wheel, coolant fluid is used. Through it's lubricating nature, the coolant deducts the friction in the contact zone. Instead of the pinion, the coolant reduces the heat energy by conducting into itself [29]. So the more cooler the fluid, the higher the heat transfer. Finally, the important function of the coolant is to flush away the chips generated from the grinding operation. if the chips clog, they eventually dull the grinding wheel generating much heat input into the pinion [18]. The coolant used in the grinding zone basically undergo nucleate boiling and this process increased the heat transfer between the pinion and the coolant fluid. Due to the rise in the temperature, the nucleate boiling is converted to film boiling. This film boiling develops a vapour between the pinion and the coolant fluid and acts a insulator by preventing the transfer of heat to the coolant fluid. This mechanism quickly rises the temperature and thermal damage is observed on the surface of the pinion. So to function the coolant fluid effectively, the pinion temperature should not exceed the coolant's film boiling temperature [59].

2.3. Mechanism of grinding induced burns

During grinding operation, there is large energy involved per unit volume while chipping off the material, which results in a rapid localised heating of the grinding zone. Due to this rapid heating, the pinion surface can be thermally damaged causing the deterioration of residual compressive stresses, hardness and heat-treated microstructure [42]. The actual rise in temperature during the grinding operation is affected by a range of factors, including the size, type of workpiece and abrasive hardness on the grinding wheel, method of coolant supply, grinding speeds, feed rate and grinding wheel dressing conditions [44]. Around 60% - 95% of the heat generated during the grinding operation directly conducts the pinion surface and when this crosses the critical tempering temperature phase transformation temperature, grinding burn is observed on the surface resulting in the microstructural change, reduction in hardness and high tensile residual stresses [24].

2.3.1. Thermal and mechanical effects during grinding

Considering the thermal and mechanical loading on the pinion surface, the grinding operation is termed as an external short-time local thermo-mechanical load process. The resulting load is obtained from the contact between the pinion surface and the single sintered Al_2O_3 triangular PSG of the grinding wheel. By the multiplicity of the grains on the grinding wheel and its high velocities, the pinion surface can experience a local flash temperature[48]. Jermolajev.S, Epp.J et al [30], studied the material modifications caused by thermal and mechanical loading during the grinding process on 16MnCr5 hardened steel and concluded that the depth of the grinding burn zones will vary for different maximum contact temperatures and contact time. Due to the hydrostatic pressure of 5000 MPa on the workpiece, the thermodynamic equilibrium temperature (Ac_1) on the tempered martensite microstructure comes down to 620°C for the above mentioned composition as there is a shift in Gibbs free energy. The calculated contact time to create the grinding burns are around 0.75 - 1.00 second depending on the depth of cut on the workpiece. Figure 2.16 illustrates the maximum contact temperature and the contact time of the workpiece investigated.

2.3.2. Microstructural degradation due to grinding burns

Case hardened steels have relatively higher carbon content on the surface and can easily be thermally damaged by rough grinding at high temperatures. At the high temperatures, the surface material experiences plastic strain and thermal expansion. When the material is cooled, the surface contracts and causes tensile stresses on the surface [69]. Due to this, the microstructure and hardness measurement of the pinion changes in the case hardening depth. Grinding induced burns and surface cracks will reduce the strength properties, surface quality of the pinions and make it difficult to fully exert the superior property like fatigue strength. When pinions are exposed to heavy loads and high speeds, the local stress concentration on the gear surface is easy to trigger and the fatigue strength is significantly reduced, which makes the pinion vulnerable to spalling and other

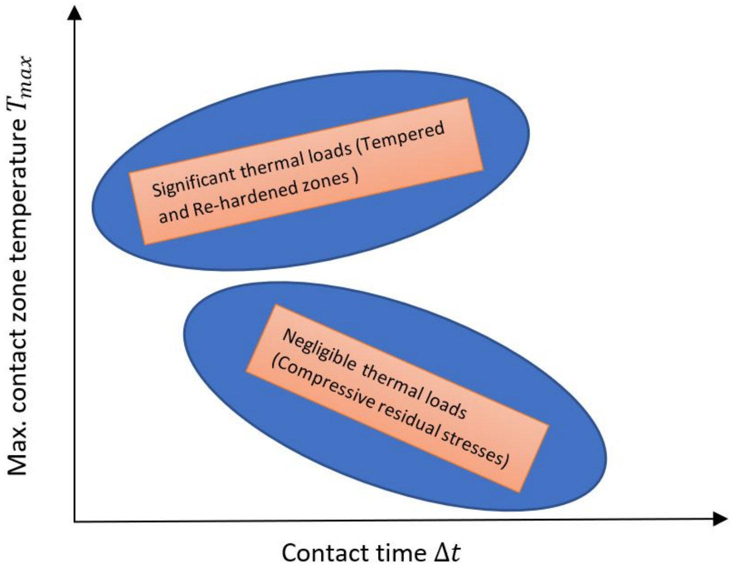

Figure 2.16: T_{max}-Δt diagram [30]

detrimental phenomena during the work cycle and eventually the entire pinion fail [67]. In the following sections, we will be discussing the thermal damages. Classification of grinding defects into four categories [64] :

- Oxidation burn
- Thermal softening
- Residual tensile stresses
- Phase transformations leading to re-hardening burn

Oxidation burn causes discolouration of the workpiece on the surface and occurs without any metallurgical damage to the workpiece. It is observed on the case of pinion or near to the grinding area, where the conductive temperature is high. When the grinding temperatures exceed the tempering temperature of 210°C, there is a reduction in hardness properties due to thermal softening. Residual stresses can be caused by mechanical or thermal effects. Mechanical effects contribute to residual compressive stresses on the surface which is beneficial [7]. The residual tensile stress is induced by the work piece's thermal expansion beyond its yield stress, which puts the material near the surface under constant tension. As the grinding temperature reaches the austenitizing range, there is a change in the material's metallurgical phase and the subsequent cooling by coolant produce a re-hardening burn. This forms a thin layer of brittle, hard, untempered martensite. Figure 2.17 illustrates the various intensities of thermal damage and gives a rough idea of the relative temperatures with each other. T_{amb} is the temperature where the oxidation burn is observed and the intensity of the burn increases with increasing temperature until T_{aust} which is austenitization temperature.

Figure 2.18 illustrates the difference between the Re-hardened zone and the Tempered burn. The white etched region is the freshly formed martensite upon cooling during the grinding process and has high hardness values. This region is prone to crack initiation due to the brittle nature. The dark etched region is the tempered burn zone and has very low hardness due to the 3rd or 4th stage tempering creating a softer microstructure by the carbon dissociation from the BCT martensite to the austenite phase.

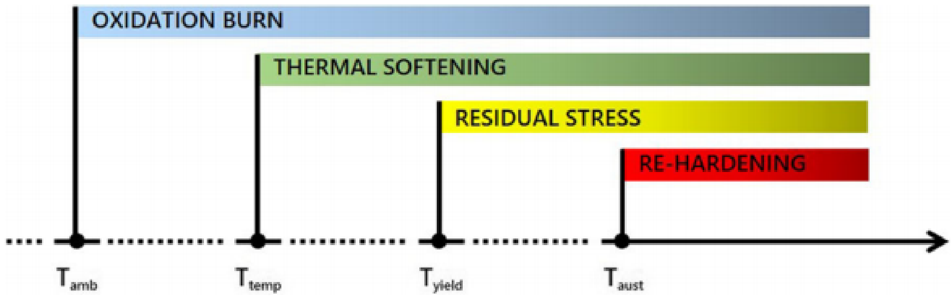

Figure 2.17: Different types of thermal damage and the relative temperatures at which they occur [7]

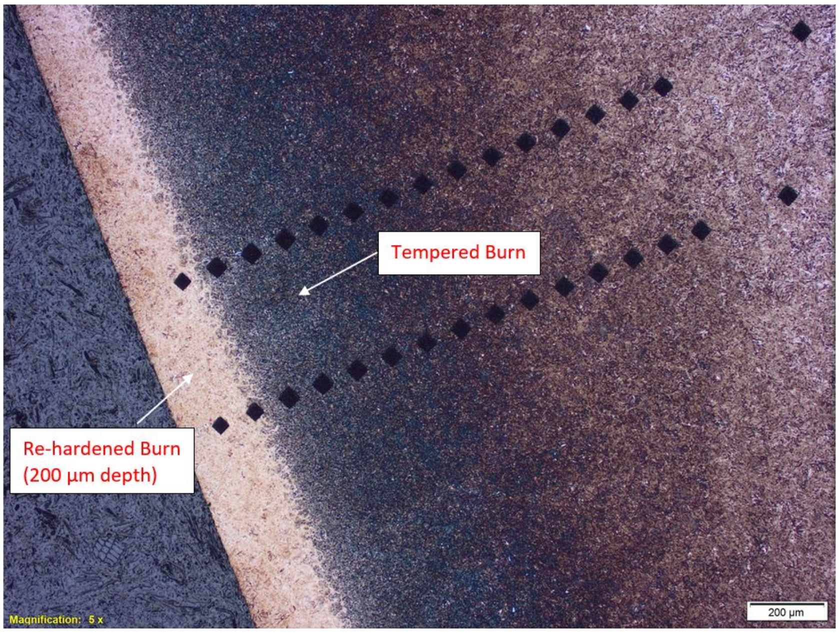

Figure 2.18: Re-hardened burn surrounded by the tempered burn

2.4. Barkhausen Noise

The detection process of grinding burns is very important to maintain the quality of the pinions. Barkhausen Noise is a non-destructive detection technique used in the production. It is a micro-magnetic method and the signals are influenced by the elastic stresses and microstructure of the material.

2.4.1. Principle

The concept of ferromagnetic domains was proposed by Weiss in 1907. These domains are microscopic and magnetically ordered regions that resemble bar magnets within the material [36], see figure 2.19. Each domain is magnetised in a crystallographic easy direction which is [1 0 0], [0 1 0] and [0 0 1] for steel. Between the domains, there are walls, where the direction of magnetisation usually turns 90° or 180°. These walls are known as Domain walls or Bloch walls. In the domain walls, the magnetic spins rotate at a rate that minimizes the total energy. Irreversible movement of domain walls because of an applied magnetic field can be observed with a conducting coil. This effect is known as Barkhausen Noise and was discovered in 1919 by Professor Barkhausen at the University

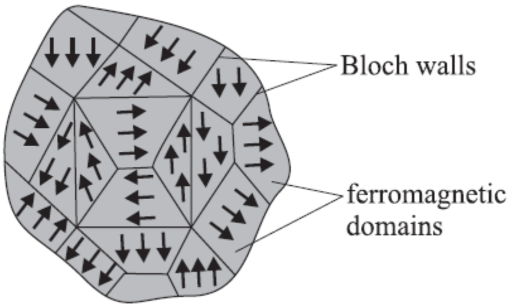

Figure 2.19: Magnetic domains and Bloch walls[36]

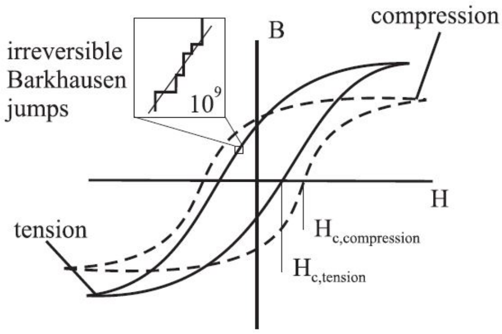

Figure 2.20: Schematic presentation of magnetic hysteresis graph [36]

of Dresden [36]. His theory proposes that a change in an external magnetic field would result in a step-wise change of domain orientation inside a ferromagnetic material. This effect also depends on the hardness of the material and suggested a test method to measure the effect of steel hardness [35]. In a ferromagnetic material, there will be isolated regions with different magnetic properties known as magnetic inclusions and dislocations. This dislocations and inclusions pin the domain walls by lowering the domain wall energy and through the magnetoelastic coupling respectively [13]. Other inclusions, grain boundaries, precipitates and voids also pin to the domain walls. The pinning of domain walls will make the movement irreversible. once the energy barrier or pinning energy is overcome, the walls move in abrupt steps that causes discontinuous changes in the flux density called Barkhausen Jumps which can be seen in the hysteresis loop in Figure 2.20. The jumps emit an electrical pulse that can be detected by a coil of conducting wire placed nearby. Barkhausen Noise is a collection of all the electric pulses generated. The amplitude of this signal is referred to as Magnetoelastic Parameter (MP). Magnetoelastic interaction is the interaction between elastic properties and domain structure/magnetic properties of the material [31]. It is possible to calculate the measurement depth by using the case hardened depth equation:

$$\delta = \sqrt{\frac{1}{\pi \upsilon \sigma \mu}} \tag{2.4}$$

where δ = Penetration depth, υ = Frequency, σ = Conductivity and μ = Permeability.
By changing the frequency range analyzed for the Barkhausen Noise, it is then to possible to measure from different depths. The penetration depth decreases with increasing frequency

2.4.2. Influence of hardness and residual stresses on Barkhausen Noise

When a material is case hardened to increase its hardness, the dislocation density increases and this increase in dislocation density will increase the energy needed to induce the domain wall motion [31]. Magneto-elastic parameter (MP) is effected by precipitates, dislocations, grain boundaries and residual stresses which impede the motion of domain walls. Magnetoelastic interaction is the interaction between elastic properties and domain structure/magnetic properties of the material. As a result of magnetoelastic interaction, in materials with positive magnetic anisotropy (iron, most steels and cobalt), compressive stresses and increasing hardness will decrease the intensity of Barkhausen Noise while tensile stresses and decreasing hardness increase the intensity of signals. Bloch walls (BW) interfere with the stress state as well as microstructure features (such as dislocations, carbides, grain boundaries, non-ferromagnetic particles, etc.) that pin the BW motion [31]. The high intensity Barkhausen Noise signal of over-tempered surfaces after grinding is mainly associated with reduced dislocations density that is thermally initiated by elevated temperatures, which in turn correspond with decreased pinning strength. Grinding induced burns decreases the hardness property and increases tensile stress at the surface. With the help of increased or decreased amplitude of Barkhausen Noise MP values, the tempered and re-hardened grinding burns can be detected. Figure 2.21 illustrates the principle and influence of Barkhausen Noise measurements.

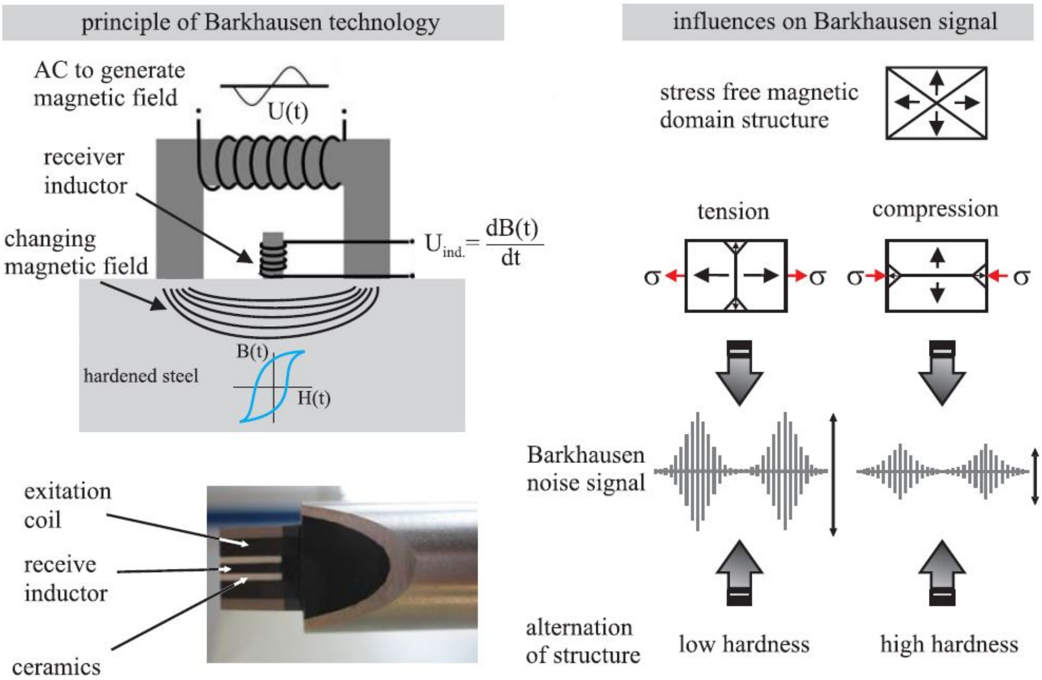

Figure 2.21: Principle and influence of Barkhausen Signal measurement[36]

2.5. Pinion fatigue failures

Fatigue is the dominant failure type in gears and the gear loading capacity is basically limited by different failure modes [11]. In rotating bodies (crown, pinion gears) high cyclic contact pressure loads develop and simultaneous rolling and sliding is observed due to the relative motion between them [16]. Figure 2.22 represents a schematic illustration of gear tooth interaction (Start and end of gear tooth contact). Rolling and sliding direction of gear tooth contact is observed between driving (pinion) and driven (crown gear). This contact between the gears make its profile to transmit continuous rotary and uniform motion [57]. This combined mechanical load of the parts essentially determines the likelihood of surface contact fatigue to grow and tends to give a basic understanding of the phenomenon referred to as rolling-sliding contact fatigue (RSCF).

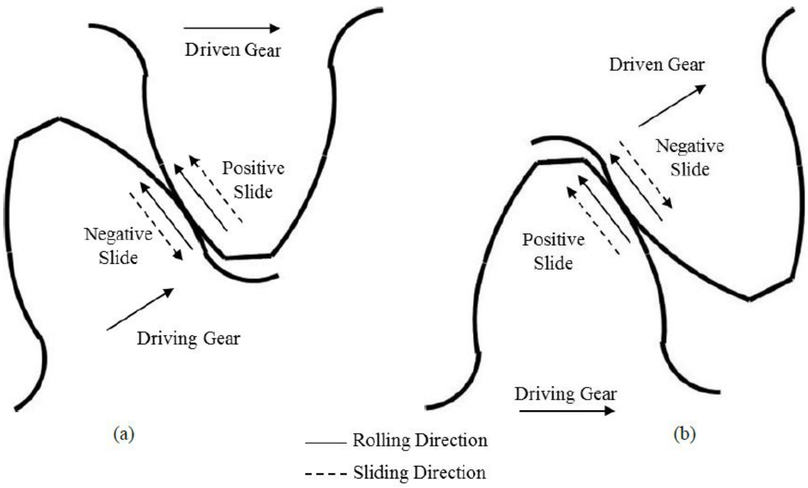

Figure 2.22: Schematic illustration of gear tooth interaction. (a) Start of contact. (b) End of contact [54]

The failure modes in the pinion are majorly influenced by it's design, working conditions, material properties and the lubricant conditions [11]. The failure of pinions can basically be divided into fatigue and non-fatigue related material failures modes, mainly due to tribological problems in the lubricated contact, for example scuffing (Adhesive wear) [67]. The further differentiation of failure modes are also possible based on the initiation site like on pinion flank or tooth root and also based on the surface crack initiation site or sub-surface sites in the pinion [9].

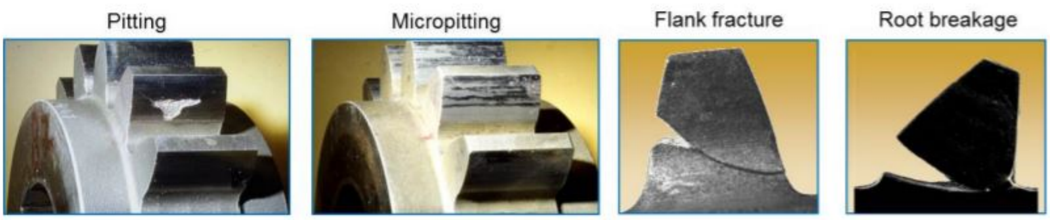

Figure 2.23: Prominent gear failure modes [67]

Figure 2.23 illustrates the prominent gear failure modes in relation with material fatigue. Surface pitting and tooth root failure are the typical mode of failures characterised based on the crack propagation in the material and they basically initiate at the surface or sub-surface [9]. Hertzian contact stresses in the gear contact (Crown and pinion) strongly influence the pitting load capacity and the bending stresses observed in the root fillet is related to the tooth root strength [67][68]. Spalling is observed due to pitting fatigue, which increases friction and wear and reduces the load bearing capacity of a tooth before fracture occurs.[68]. Due to the unfavorable lubricating conditions, micro-pitting which is also considered as mode of fatigue failure is very often noticed at the surface of the loaded gear flank and distribution of the crack is limited to near-surface region. This can also give rise to flank initiated bending fatigue failure [23]. Further, the contact load at the surface of the tooth flank introduces stresses into the material until certain depth. As these stresses are exceeding the local material strength, crack initiation and the final failure is observed below the surface. This is referred to as Tooth interior fatigue fracture (TIFF), sub-surface fatigue or tooth flank fracture [67].

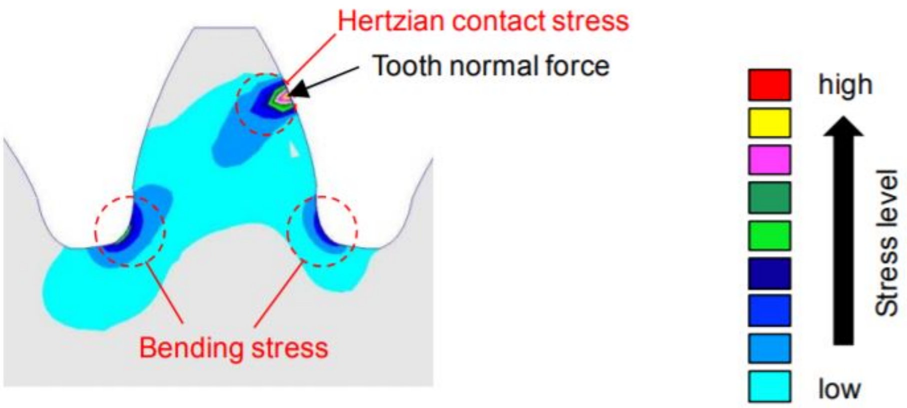

Figure 2.24: Schematic distribution of stress inside a gear tooth indicating highly loaded areas (Hertzian contact stress at tooth flank, bending stress at tooth root) [67]

Figure 2.24 illustrates the schematic stress distribution within a pinion gear tooth suggesting high stress zones. The normal forces at the tooth flank causes contact stresses and the tooth root is influenced by bending stresses as shown in figure 2.24. This form of gear failure results in a total gear tooth fracture or multiple adjacent tooth breakage. The mechanism of pinion failure under tensile stress corresponds to 3 stages: crack initiation, propagation and final fracture. The pinion tooth functions as a short cantilever loading beam [15]. Fatigue cracks initiate at tooth radii because of cyclic nature of gear tooth loading. [68].

The retained austenite is expected to have a detrimental effect in the high cycle fatigue regime as it tends to have lower hardness values [70]. The retained austenite and residual stresses effect on rolling and sliding contact fatigue (RSCF) in 18CrNiMo7-6 carburized steel has not been fully established and is, therefore, a key test variable for this research on their behaviour on fatigue life and damage.

3
Problem Statement

The thesis is in collaboration with DAF Trucks NV, a truck manufacturer which produces light, medium and heavy-duty trucks. The company also manufactures rear axle differentials (crown and pinion gears) at it's production site. During the production of the pinions, grinding induced burns are detected after the grinding finishing process. The detection is done using nital etching and when the tooth surface turns dark, there is an indication of burn as shown in figures 3.1 and 3.2. Recently the barkhausen noise equipment is introduced in the production site for non-destructive testing of the pinions to detect the grinding burns. However, there is a need to understand the barkhausen noise signal behaviour with the pinions and how actually the Barkhausen signals are correlated with the deteriorated material properties due to the grinding induced burns. To understand this behaviour, material characterization of the different intensities of barkhausen noise signals is to be done and the obtained results are to be analyzed.

Even though we understand that the grinding induced burns degrade the material residual stresses and hardness properties due to the thermo-mechanical loading, there is no knowledge on how the burns affect the fatigue life of the pinions in the functioning of the truck as they were never tested and thus requires further investigation. Whenever there is a certain intensity of the grinding burn is noticed, the pinions are scrapped and there is a huge loss in time, material and money. So this research is also focused on the axle testing which gives an overview of the material degradation like crack initiation and growth due to rolling sliding contact stresses on the grinding burn tooth surfaces.

The project is in collaboration with central lab, production plant and product development departments of the DAF Trucks NV. TU Delft is involved in validating few of the residual stresses and retained austenite measurements in the Materials Science and Engineering laboratory using X-Ray diffraction and Electron Back Scattered Diffraction (EBSD) techniques.

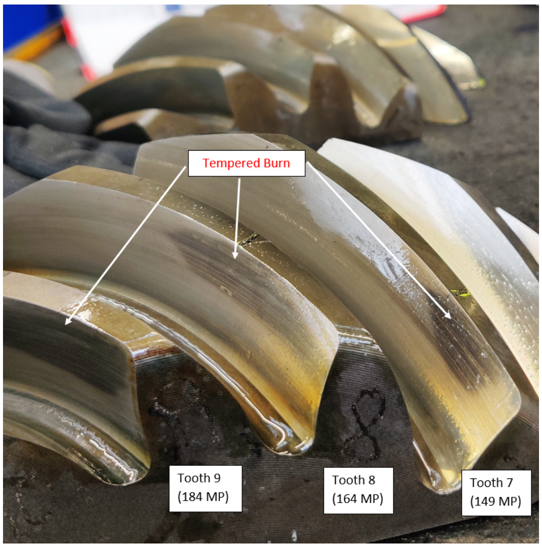

Figure 3.1: Grinding induced burn etched with Nital

Figure 3.2: Crossectional view of the burn

3.1. Research questions

The problems regarding the detection, material characterization and fatigue life of the grinding induced burns pinions led to the following research questions:

- How the different grinding parameters are effecting the material deformation and the generation of grinding-induced burns?
- Investigating the material characteristics of the different intensities of tempered and re-hardened grinding burns and set an accepting safe limit of Barkhausen noise signals.
- How the grinding induced burn microstructure is initiating the micropitting and affecting the fatigue lifetime of pinions?

3.2. Objectives

In order to answer the research questions, the following objects are formulated:

- Categorize the pinions into different grades and generate them accordingly in the production plant with the help of engineers.
- To perform the Barkhausen Noise analyses on various categorized pinions and on different locations of the tooth flank to understand the deformation.
- To Understand the formation mechanism of tempered and re-hardened burn on the tooth surface.
- To understand the effect of residual stresses and retained austenite in relation with barkhausen noise signals.
- Perform the axle fatigue testing of grinding burn pinions in the DAF Trucks test rig to understand the real time lifetime.

4

Methodology and Experiments

4.1. General specifications

The pinions used for the experimental study are hypoid gears and connected to a 11 or 13 litre 6-cylinder inline diesel engine (DAF MX-11, DAF MX-13) driveshaft. The pinion has 15 tooth connected to 36 tooth crown gear with a gear ratio of 2.40 and belong to the 1347 axle configuration. The first two numbers '13' indicate the designed nominal load in tonne and the last two numbers '47' indicate the designed nominal torque in kNm. Even though the number suggests 47 kNm, the axles are designed for 46 kNm nominal torque with 23 kNm at each rear wheel. The dimensions of the pinions used in the investigation are shown in figure 4.1. The material composition of the pinions is mentioned in table 2.1. The microstructure constituents of high carbon plate martensite, retained austenite at the surface and low carbon lath martensite in the core.

Table 4.1 gives the information about the pinion parameters.

Parameters	**Pinion**
Base material	18CrNiMo7-6
No. of teeth	15
Gear ratio with crown wheel	2.40
Module (mm)	9.6038
Face width (mm)	84.4652
Addendum (mm)	13.1852
Whole depth (mm)	25.2803
Pitch diameter (mm)	189.7
Mean spiral angle	40.5898 degrees
Normal pressure angle (Coast)	22.2721 degrees
Normal pressure angle (Drive)	20.7279 degrees

Table 4.1: Pinion parameters

To grind the pinions, 99DA Cubitron II with 3M precision-shaped grain is used. Figure 4.3 illustrates the discontinuous generation grinding process. The grinding wheel material is constant throughout the sample generation but the grinding parameters are varied to understand its relation with

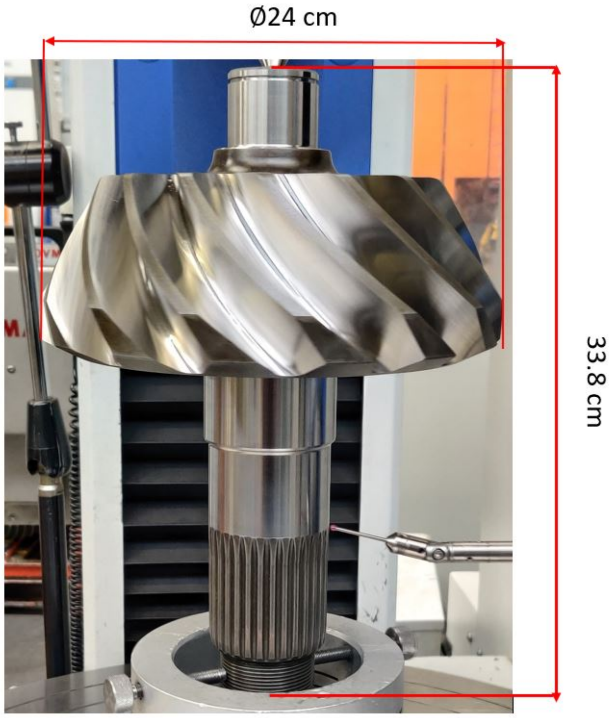

Figure 4.1: The dimensions of pinions used in experimental study. The diameter of the pinion is 24 cm and length of the pinion is 33.8 cm

microstructure characterization. The grinding wheel has a certain nomenclature to describe its characteristics. 99DA80 F15VPH601W is the specific number of the grinding wheel. Figure 4.2 illustrates the characteristics of the grinding wheel. The geometry of the grinding wheel is: diameter = 385 mm, wheel width = 37.5 mm and height = 99 mm.

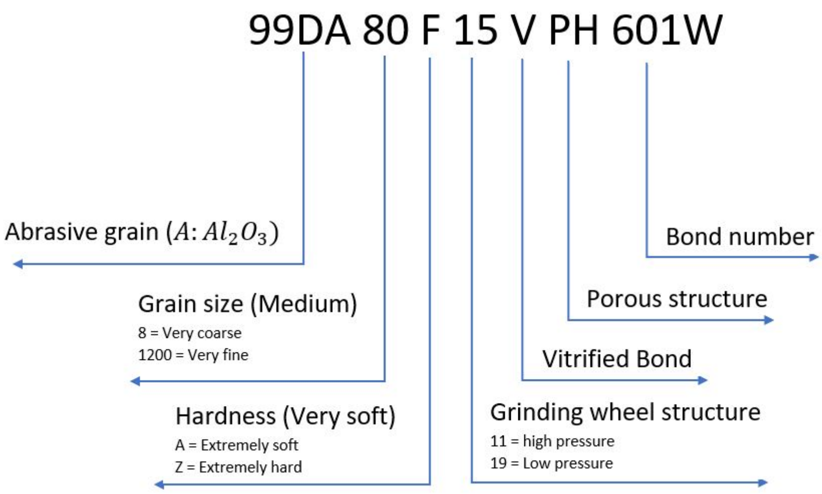

Figure 4.2: 3M Cubitron II grinding wheel nomenclature

Figure 4.3: Discontinuous generation grinding of pinion using 3M Cubitron II grinding wheel (3M company)

4.2. Methodology

To investigate the research questions, specific experimental methodology is planned. The study is done on 7 pinions with specific parameters mentioned in the table 4.2. In the table the grinding determines the number of cycles required to remove 0.300 mm from the surface and the pinion speed (°/sec) explains the movement of the pinion during the grinding process. The higher the pinion speed, the faster the process and the table also includes the heat treatment performed batch schedule. The month and year determines the heat treatment schedule performed in the furnace. Figure 4.4 illustrates the design of experimental samples for the project and the number mentioned in the brackets is the unique product number of each sample. Totally 7 pinions are used in this study. The pinion from the heat treatment furnace (W466) is examined to understand the material characteristics of the pinion which isn't ground. the grinding can take place normally in a controlled manner or abusive grinding process. 2 pinions are generated by varying pinion speed and grinding cycles. A651 represents 2 cycle process and V431 represents 3 cycle process. Finally the characterization of axle tested pinion P009 is performed to compare its behaviour with grinding burn axle test material characteristics K041 (drive test) and K905 (coast test). K220 pinion is the pinion generated by abusive grinding process unexpectedly. So the concrete reason to this abusive behaviour is not known yet. The characterization is done on this pinion to evaluate the material properties.

The material removal rate after the grinding process on the pinion tooth is around 0.250 mm to 0.300 mm irrespective of the grinding cycles and pinion speed. The only difference observed is the grinding time. For 2 cycles it is around 7 minutes, 3 cycles around 10 minutes and for 5 cycles the process is around 20 minutes.

7 Samples	Grinding cycles	Pinion speed (°/sec)	Grinding burns	Heat treatment batch
W466	Not ground	Not ground	Not ground	July 2020
V431	3	3.75, 3.75, 3.25	No	July 2020
A651	2	4.50, 3.5	No	August 2020
P009	5	Not available	No	August 2018
K220	2	4.50, 3.50	Yes	May 2019
K041	2	3.75, 3.25	Yes	July 2019
K905	2	3.75, 3.25	Yes	July 2019

Table 4.2: Samples with varying pinion speed

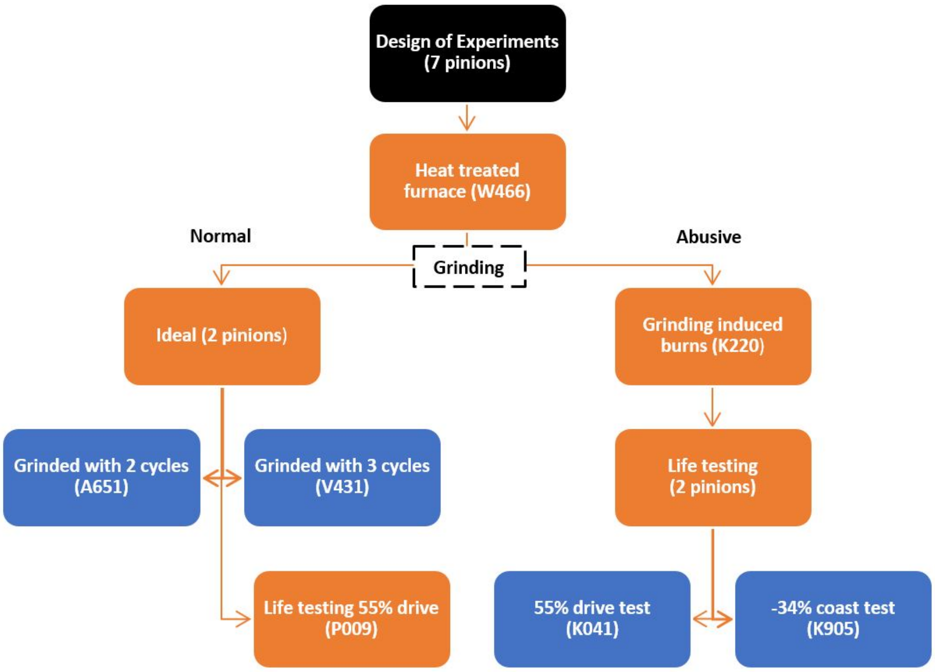

Figure 4.4: Design of experiments flowchart for 7 pinions

4.3. Experimental characterization

The experimental characterization begins with the detection process. Barkhausen noise analysis is performed on the pinions and then followed by nital etch on the tooth. One tooth from each pinion is cut and sectioned to investigate the material behaviour. The sample tooth is then characterized with Vickers hardness (HV), microscopical analysis and X-ray diffraction analysis.

4.3.1. Barkhausen Noise

The pinions after the grinding process are tested for the detection of grinding-induced burns using Barkhausen noise machine as a NDT quality control to observe the qualitative microstructural and residual stress variations. Figure 4.5 illustrates the Barkhausen noise setup at the DAF production plant. The main components are Rollscan 350 digital Barkhausen noise analyser, Barkhausen robotic hand, sensor and viewscan software which displays the final output on the computer. Optimum magnetic field strength is needed to achieve maximum sensitivity, which is dependent on the voltage and the frequency generated by the sensor. If the field is too strong or poor, the result of the signal to Noise ratio will be either saturated or poor in sensing the signal which is not recommended. 300 Hz frequency and 5 Vpp voltage is selected to achieve the maximum sensitivity. The frequency is inversely proportional to the measured depth as mentioned in equation 4.1. So as the frequency increases, the measuring signal depth decreases. As shown in the figure 4.5, The sensor scans 9 cm along the surface of the pinion. The time to scan and receive the signals for one flank is around 5-7 seconds and the overall measurement on all the 30 flanks (drive and coast) consumes about 8-10 minutes considering the pinion movement.

$$\delta = \sqrt{\frac{1}{\pi \upsilon \sigma \mu}} \tag{4.1}$$

where δ = Penetration depth, υ = Frequency, σ = Conductivity and μ = Permeability.

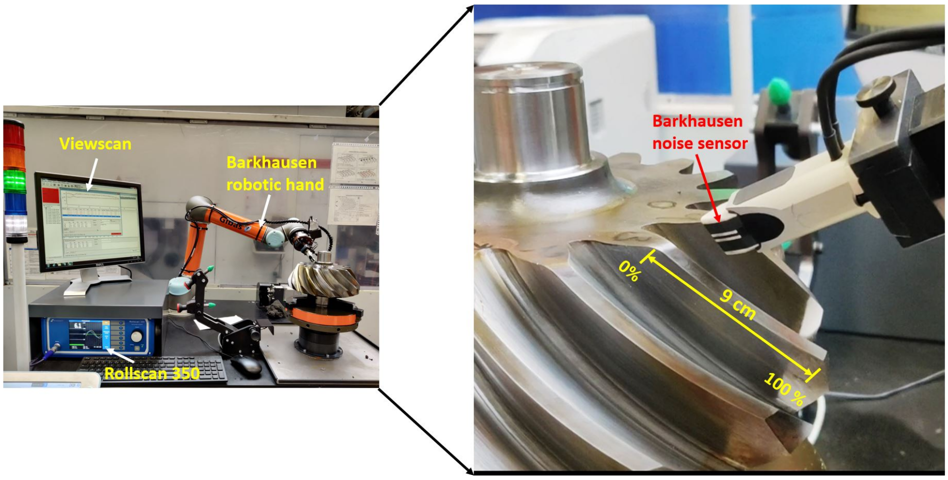

Figure 4.5: Barkhausen Noise machine in detecting the grinding-induced burns

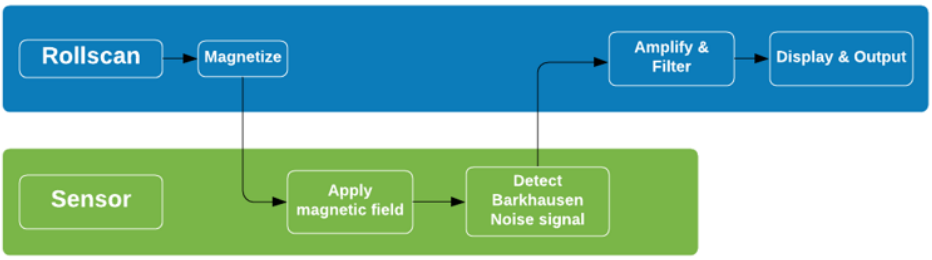

Figure 4.6: System flow chart of Rollscan 350 [2]

With the selected 300 Hz frequency, the grinding burns are detected at around 60-70 microns depth from the surface. When the robot sensor receives the required path, voltage and frequency parameters from the operator utilizing Rollscan 350, the magnetic field is applied by the black brittle ferrite structure and the signals are received by the white receiving poles on the sensor as shown in figure 4.5. The signals are then filtered and displayed on the Viewscan software as shown in Barkhausen noise system flowchart figure 4.6.

The detection process can be done on 3 levels called as high, middle and low as represented in the figure 4.7 (**a**). The 3 colors indicates the different path levels (high, middle and low) and the operator selects the input path parameter. This is an interesting feature in understanding the material stresses and microstructure pattern at 3 different levels and analyze the temperature distribution along the tip to the root direction after the grinding process. During the grinding process, depending on the coolant flow, grinding wheel movement, temperature distribution varies from tip to root. The path patterns on the drive and coast are slightly different. On the drive side the sensor paths don't go below the pinion pitch line, whereas on the coast side, the lowest BN level is below the pitch line. Due to this difference in the signal path levels on the drive and coast, the MP values are not comparable and have to be analyzed separately.

An example of the obtained BN signal of a tooth on drive side is shown in figure 4.7 (**b**). The X-axis indicates the length of the measured flank in 0 to 100 % length of a middle level. Throughout the flank, 200 signal points are detected by the sensor. The signals detected are the root mean square or effective voltage values of the noise spectrum and notified as Magnetoelastic parameter (MP). The

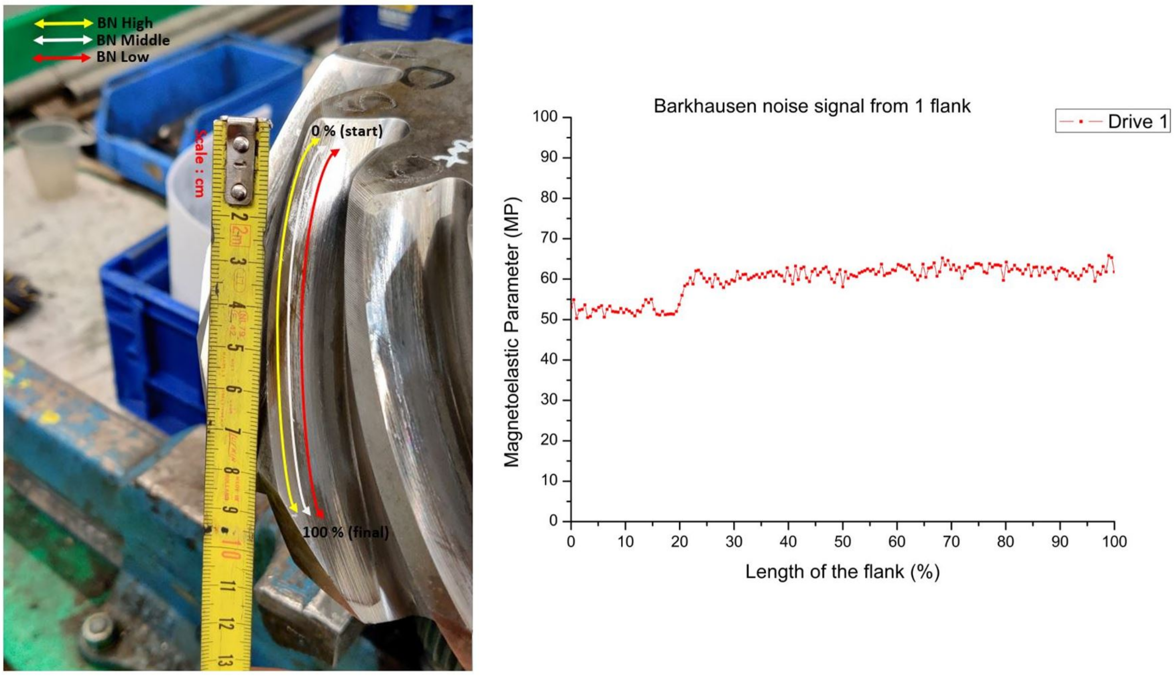

Figure 4.7: (**a**) Barkhausen sensor path on 3 levels; (**b**): BN signal output as shown in viewscan software of 1 flank

MP values are indicated on Y-axis and indicates if the flank is affected with grinding-induced burns or not depending on the measured MP value. As this flank has an average value of 57 MP - 60 MP, it is considered to be a flank with no grinding burns. The problem arises if it crosses the signal of 100 MP as it indicates the microstructural variations due to the high localized heat energy input in the grinding operation.

4.3.2. Nital etch

After the NDT detection with the Barkhausen noise machine, the pinion flanks with high MP values are etched with Nital solution (96% Ethanol + 4% HNO_3). This verifies whether the flank is affected with the burn. The pinion is placed on a specific rotating table to perform the etching process. The tooth to be etched is degreased with a paper cloth and rinsed with ethanol. A cotton ball is picked up with a holder and dipped in the nital etch solution. With a normal pressure, the cotton ball immersed in nital solution is rubbed along the flank for 30 seconds. At the burn site, dark grey discolouration is observed and the remaining area of the flank will be in uniform grey colour as seen in figure 4.8. The flank is again rinsed with ethanol to neutralize the effect and WD40 oil is sprayed on the flank in the final step to prevent corrosion.

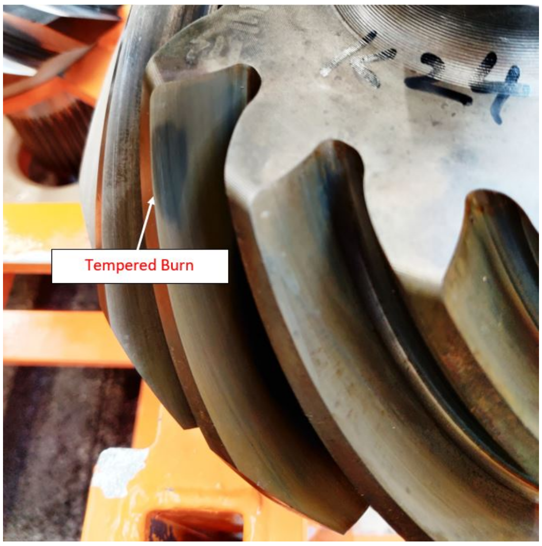

Figure 4.8: Example of tempered burn observed with nital etch

4.3.3. Sample preparation

To prepare the samples for microstructural and hardness analysis, the pinions are cut using a Struers Exotom-150 cutting machine (figure 4.9) with a feed rate of 0.10 mm/s using the Exicut offset mode. This low feed rate helps to cut the pinions without significant heat generation to avoid microstructural change during operation . Then the tooth cross-sectional cut will be mounted in a 4cm diameter Bakelite resin. To prepare that, the cut sample is placed in a Struers citoPress-5 filled with durofast epoxy resin near to the cut sample and Bakelite phenol resin far from the sample and heated to 180°C at 200 bar pressure for 3 minutes to melt the resin and liquid cooled for another 3 minutes to form a hard sample (Figure 4.10). The prepared sample is now polished in 3 steps for 20 minutes using Struers LaboForce-3 machine. The first polishing step is done for 10 minutes on MD Piano 220 disc with water as a lubricant, the second polishing step is done for 5 minutes on MD Allergo resin bonded diamond disc with 9μ water-based diamond suspension as a coolant lubricant and the last step of fine polishing is done for 5 minutes with 3μ water-based diamond suspension as a coolant lubricant (Figure 4.11). The sample is cleaned with ethanol and dried at ambient temperature with a dryer. The properly polished surface has a shiny mirror finish without any scratches as shown in figure 4.12.

Figure 4.9: the Struers Extom-150 cutting machine uses a feed rate of 0.10 mm/s is used

Figure 4.10: The Struers CitoPress-5 machine is used to mount the cut sample into the resin

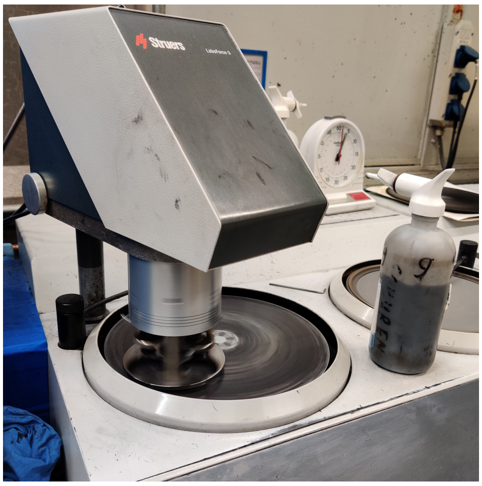

Figure 4.11: The Struers LaboForce-3

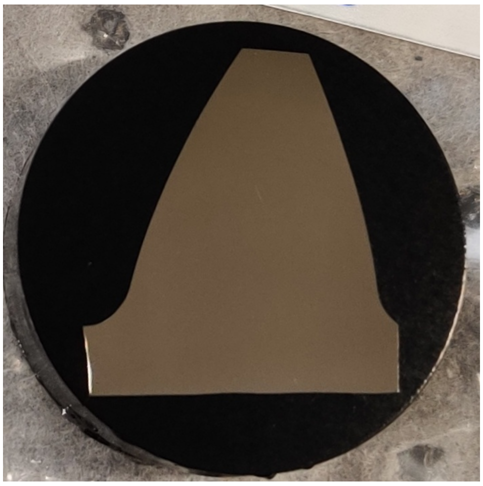

Figure 4.12: Final polished sample

4.3.4. Vickers hardness

Vickers hardness testing is done on the cross-sectional view of the tooth to evaluate the case depth and burn depth from the surface using Wilson Hardness testing machine. The measurement is done by performing a series of step-wise hardness impressions in the form of a right pyramid with a square base and an angle of 136° between opposite face from the edge of the crossection to the core of the tooth with diamond indentor at 8 different locations (Figure 4.14 with yellow lines represents high, middle, low and root level on both drive and coast side of the sample, where the hardness measurements are done). The yellow lines also indicates the BN sensor pattern of high, middle and low levels and this analysis helps to find the relation between hardness and BN MP values at particular path levels. The figure 4.15 represents the Vickers hardness impressions. On each location there are total of 33 indentations with 30 indentations until 1.5 mm depth and the remaining 3 indentations until 2.150 mm depth. Figure 4.13 illustrates the measurement standard followed for the investigation. The HV1 1 kgf load is normally applied for 10 seconds to create an impression. Then the Vickers hardness is calculated optically by measuring the diagonal length's of the impression left by indentor and the measurements are calculated to HV.

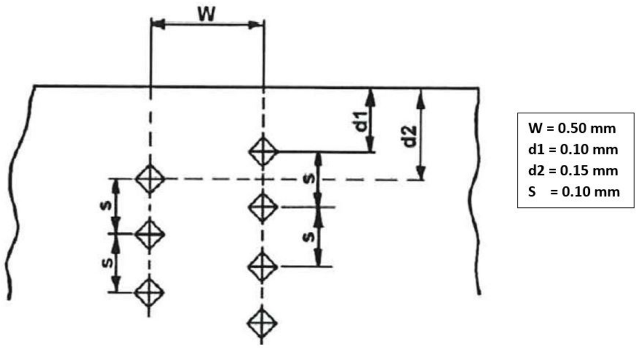

Figure 4.13: Vickers hardness standard for the minimum distances between the indentations

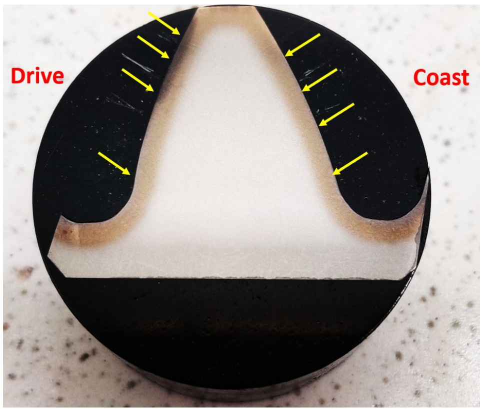

Figure 4.14: Vickers hardness impression locations on the sample

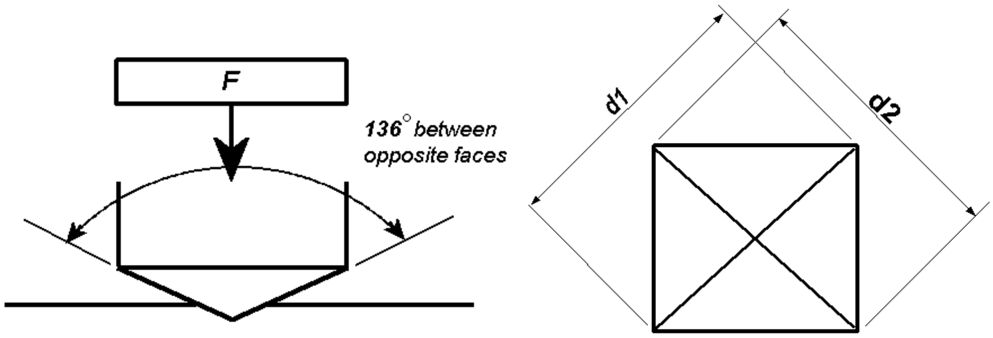

Figure 4.15: Vicker's Hardness impressions on the sample

$$HV = \frac{2Fsin\frac{136^{\circ}}{2}}{d^2} \tag{4.2}$$

where,
F = Load in kgf
b = Arithmetic mean of the two diagonals, d1 and d2 in mm.

4.3.5. Microstructural analysis

To analyse the microstructure morphology, the samples are studied in optical microscopy and Scanning Electron Microscopy (SEM). To be able to recognize microstructural features in the Leica digital optical microscope, the samples are etched. This is performed by immersing the sample in the 96% Ethanol and 4% Nitric acid (HNO_3) solution for 8-10 seconds and rinse it off with ethanol followed by drying. The purpose of the etching is to get a surface with contrast between different microstructural features that can be observed under a microscope such that microstructural features can be examined. Scanning Electron Microscopy (SEM) is used to characterize the tempered burn and re-hardened burn morphology with secondary electron imaging. The micropits formed after the fatigue testing are also evaluated on the surface and cross-section of the pinion tooth.

4.3.6. X-ray diffraction (XRD)

Residual stresses and retained austenite fractions in the samples are measured with Stresstech Xstress 3000 G2R diffractometee. Figure 4.16 illustrates the X-ray diffraction setup. The 3 major components in the setup are XRD unit where the measurement is performed, electropolishing unit where the depth profile is created by removing surface layers in microns and the Xtronic software where the final calculated output is shown.

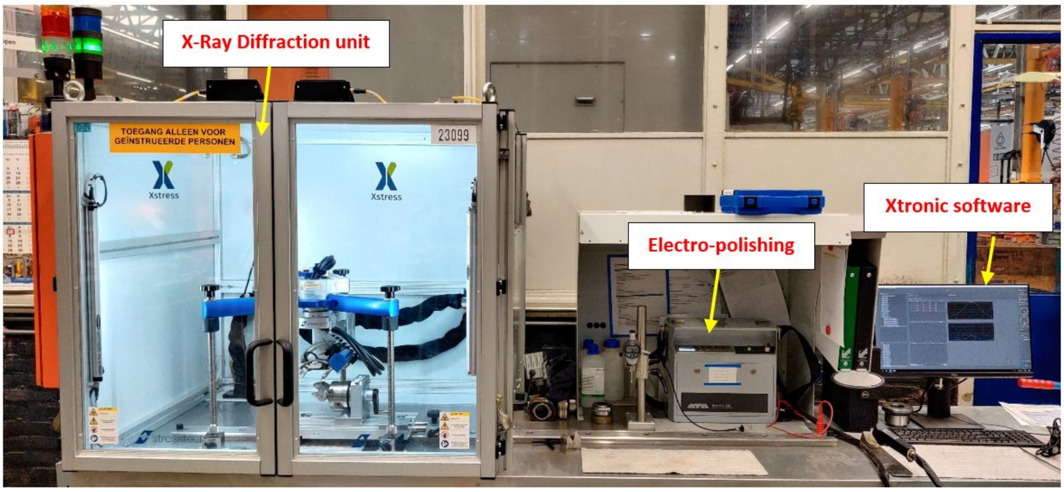

Figure 4.16: X-Ray diffraction set up at the DAF Trucks production plant

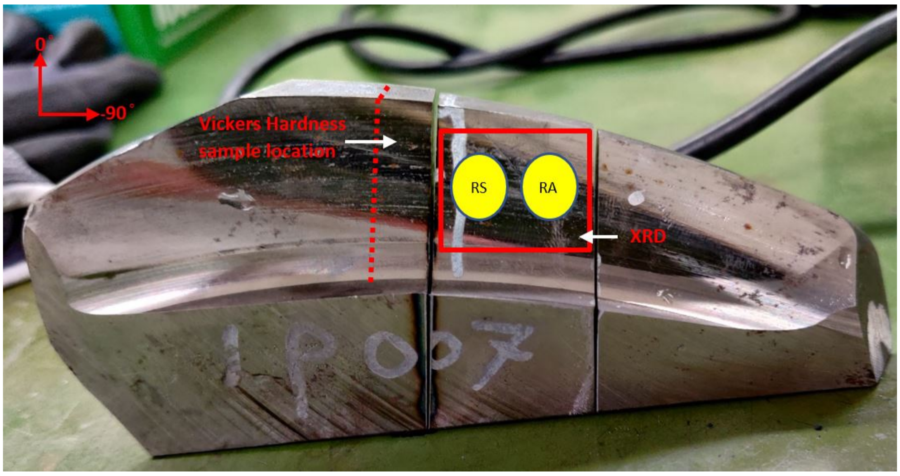

Figure 4.17: XRD residual stress(RS) and retained austenite (RA) location on the pinion tooth.

Figure 4.17 illustrates the locations where the analysis is performed on the gear tooth. The particular selected red box location is prone to high stresses as it lies in the crown/pinion contact pattern. outside the red box, the microstructural observations and Vickers hardness tooth crossection is taken. -90°and 0°represent the XRD rotational angle to measure the residual stresses.

In residual stress measurement, 2 position sensitive detectors (PSD) are used at 156.4°diffraction angle on the arc shaped detector holder to measure BCC/BCT [211] interplanar lattice spacing as shown in figure 4.18. Modified Chi (χ) measuring mode is used for the stress determination. In this mode, the lattice spacing (d) is measured for 11 tilt angles (ϕ = -18.4°, -26.6°, -33.2°, -39.2°, -45°, 0°, 18.4°, 26.6°, 33.2°, 39.2°, 45°). 2 rotation angles -90°and 0°are used to measure the stress on the longitudinal and transverse direction of the gear tooth. Cr Kα radiation is created at 30 kV and 8 mA and 3mm collimator diameter is used to measure the sample with a wavelength of 0.229 nm. The depth profile of residual stress measurements are created until 0.5 mm from the surface with 9 measuring points (surface, 0.01 mm, 0.02 mm, 0.03 mm, 0.05 mm, 0.1 mm, 0.2 mm, 0.3 mm, 0.5 mm). The material removal is done using electro-polishing by applying the current of 1.5 Ampere. The whole process is done when the electrolyte is pumped onto the surface. The exposure time determines the removal depth removing 10 microns from the surface it requires around 7-8 seconds. This can be measured using the depth measuring gauge. In addition, Full width half maximum (FWHM) of the 211 diffracted peaks are also plotted.

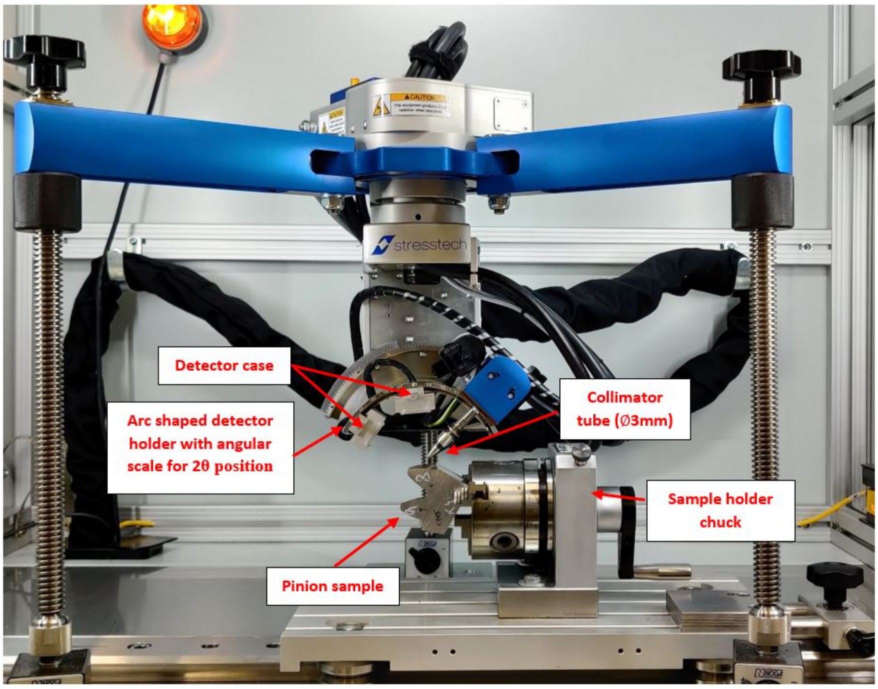

Figure 4.18: XRD components

To measure the retained austenite fraction, the whole set-up has to be modified. The diffractometer is changed and the collimator is tilted 45 degrees normal to the sample. Figure 4.19 and 4.20 illustrate the diffractometer setup and the varying detection of collimator. Four peaks for 2 different phases (Austenite and Martensite) are measured to calculate the retained austenite fraction at the irradiated area. Cr Kα radiation is created at 30 kV and 8 mA and 3 mm collimator diameter

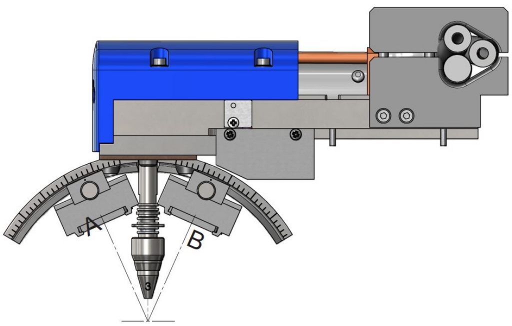

Figure 4.19: Residual stress collimator setup

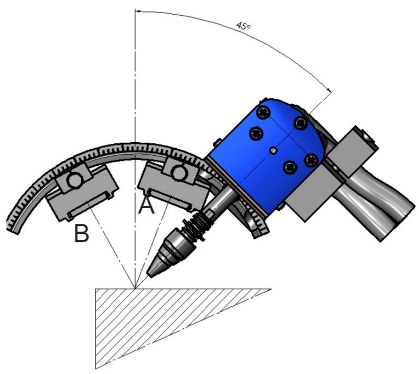

Figure 4.20: Retained austenite collimator setup

Phases	hkl	2θ	R
Ferrite/Martensite	200	106.1	18.9
	211	156.4	183.1
Austenite	200	80	26.4
	220	130	51.5

Table 4.3: Retained austenite parameters

is used to measure the sample. Additionally vanadium filters are placed at the detectors to reduce Kβ radiation. The x-ray diffracted intensity from each phase is proportional to the volume fraction of that particular phase which is the area under the peak above background. The four peaks measured are 200A (2θ = 80°), 220A (2θ = 130°), 211M (2θ = 156.4°) and 200M (2θ = 106.1°). Here A = Austenite phase and M = Martensite/Ferrite phase. Similar to residual stresses depth profiles, retained austenite fractions are also measured in the mentioned depth profile. Gaussian curve fitting method is used to analyze the retained austenite fractions. The formula to calculate the RA volume fraction (V_γ) of the numerous ferrite/martensite and austenite peaks for randomly crystallographic orientation of the phases is equation 4.4:

$$V_\alpha + V_\gamma = 1 \tag{4.3}$$

$$V_\gamma = \frac{\left(\frac{1}{q}\sum_{j=1}^{q}\frac{I_{\gamma j}}{R_{\gamma j}}\right)}{\left[\left(\frac{1}{p}\sum_{i=1}^{p}\frac{I_{\alpha i}}{R_{\alpha i}}\right)+\left(\frac{1}{q}\sum_{j=1}^{q}\frac{I_{\gamma j}}{R_{\gamma j}}\right)\right]} \tag{4.4}$$

I_γ = Integrated intensity per angular diffraction peak hkl in the γ-phase, I_α = Integrated intensity per angular diffraction peak hkl in the α-phase, R is proportional to the theoretical integrated intensity, V_α = volume fraction of the ferrite/martensite phase.

In the end, figure 4.21 demonstrates the Xtronic software results of residual stress and retained austenite measurements.

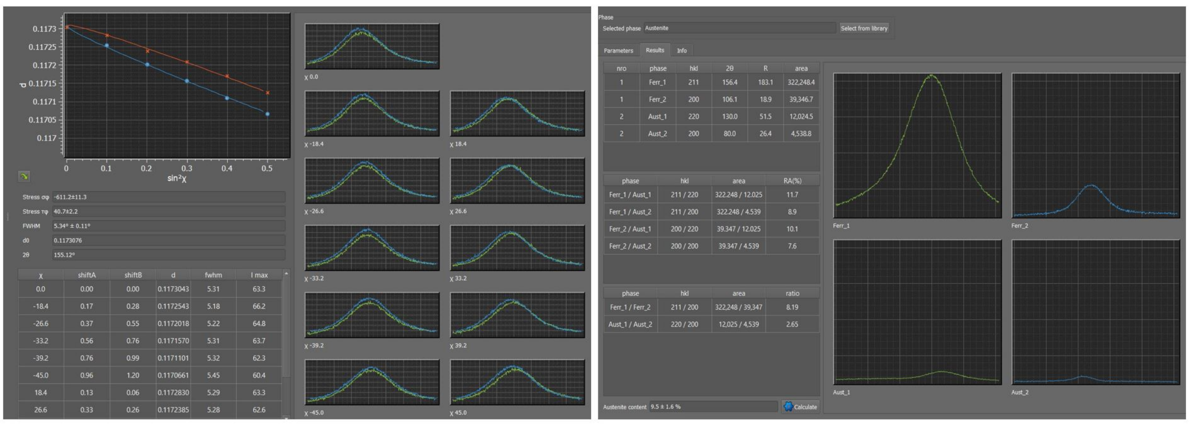

Xtronic Residual stress results Xtronic Retained austenite results

Figure 4.21: Xtronic results template for residual stress and retained austenite measurements.

4.3.7. Service lifetime test

The service lifetime (fatigue resistance) of the pinions with grinding-induced burns are tested on axle test rig setup at the DAF testing department. The failure of the gear tooth is mostly observed due to the bending stresses (tooth root breakage) and contact stresses (tooth face damage). As the grinding burns degrade the tooth flank surfaces, the axle testing is limited to contact stresses to observe pitting or spalling due to the burns. Two pinions with a specific intensity of grinding burns are selected and axle test is performed individually for drive (forward loading) and coast (backward loading) flanks to observe the fatigue behaviour.

Figure 4.22 illustrates the axle test setup. The pinions are placed in the shown axle housing. The oil level is approximately 10 liters and maintained at 80°C in the differential housing. Chevron Delo Syn-Gear XPD 75W85 gear oil is used for the test. The test parameters are plotted for torque (y-axis) vs number of load cycles (x-axis) with constant amplitude testing. one load cycle is defined as the two gears transmit the load from one tooth to the another. So each tooth of the pinion is loaded once for every pinion revolution. Reference torque level is to be selected as an input parameter to observe the contact stress lifetime on the pinion. This is an important factor as different torque loads contribute to test different failure modes. The nominal torque (T_{nom}) of the axle is 46000 Nm and the ideal torque test level to perform the contact stresses at drive flank is 55% of T_{nom} and coast flank is -34% of T_{nom}. The torque level difference for the drive test and coast test is due to an amplitude factor of around -1.5. The amplitude factor is dependent on the area of pinion/crown wheel contact patterns between the drive and coast flank of the hypoid gears. A reference speed level is determined considering the reference torque level and maximum power of the test rig. As the testing is done for torque Versus number of load cycles, the relation between the torque and the stress level is to be determined:

$$\sigma = c \cdot T_{D_S}^{m} \tag{4.5}$$

σ = contact stresses (n/m^2); $T_{D_S}^{m}$ = drive shaft torque; m = transformation factor from stress to torque domain (m= 0.28), c = constant

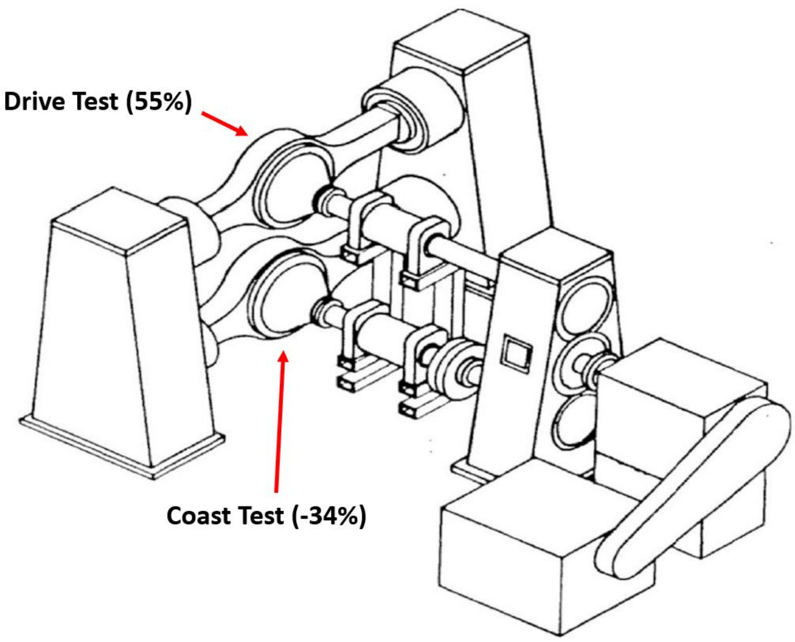

Figure 4.22: Axle test rig schematic at DAF Trucks for the drive test and coast test

5

Results and Discussions

This chapter describes the results and discussions of the mentioned 3 research questions in chapter 3. For each question, firstly the results are explained and summarized followed by the discussion section.

5.1. Part 1: Effect of varying pinion speed and grinding cycles during the grinding operation on material characterization

In this section, the results of 3 samples obtained from Barkhausen noise, Vickers hardness, optical microscopy, scanning electron microscopy, x-ray diffraction are examined in a detailed manner. The Barkhausen noise variation with the microstructure, residual stress and retained austenite is thoroughly analysed and compared with each other. The 3 samples analysed in this section are mentioned in table 4.2.

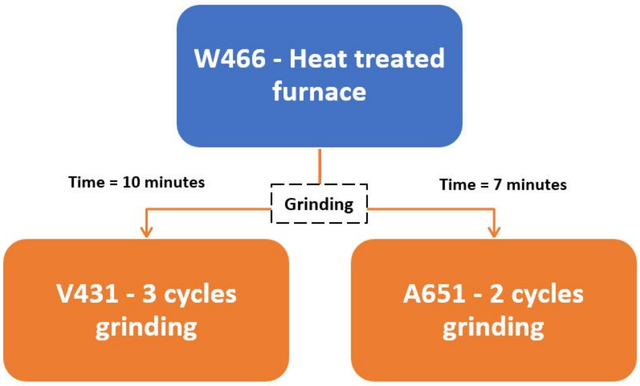

Figure 5.1: 3 samples parameters used in the present question.

Figure 5.1 illustrates the sample flow chart and the respective parameters. All the 3 pinions heat treatment process is similar as mentioned in table 2.3. W466 heat-treated furnace pinion represents the sample from the furnace which isn't ground. V431 represent the 3 cycles grinding process which have been ground for 10 minutes and A651 represent 2 cycles grinding process with 7 minutes operation time with parameters mentioned in table 5.1.

Parameters	V431 - 3 cycle grinding	A651 - 2 cycle grinding
Pinion speed (deg/sec)	3.75 °/s	4.5 °/s
	3.75 °/s	3.5 °/s
	3.25 °/s	

Table 5.1: Pinion speed at two different grinding operations.

5.1.1. Barkhausen noise analysis

The Barkhausen noise analysis of the drive (15 flanks) and coast (15 flanks) of W466 furnace is plotted in figure 5.2. Each graph represents the BN signal peaks along the flank for 15 tooth. Length of the flank in (%) is plotted on the x-axis and magnetoelastic parameter (MP) of BN is plotted on the Y-axis. The figure 5.2 (**A**) illustrates drive side of the pinion measurement on low, middle and high levels of the flank and the figure 5.2 (**B**) illustrates the coast side of the pinion tooth on low, middle & high levels as explained in figure 4.7.

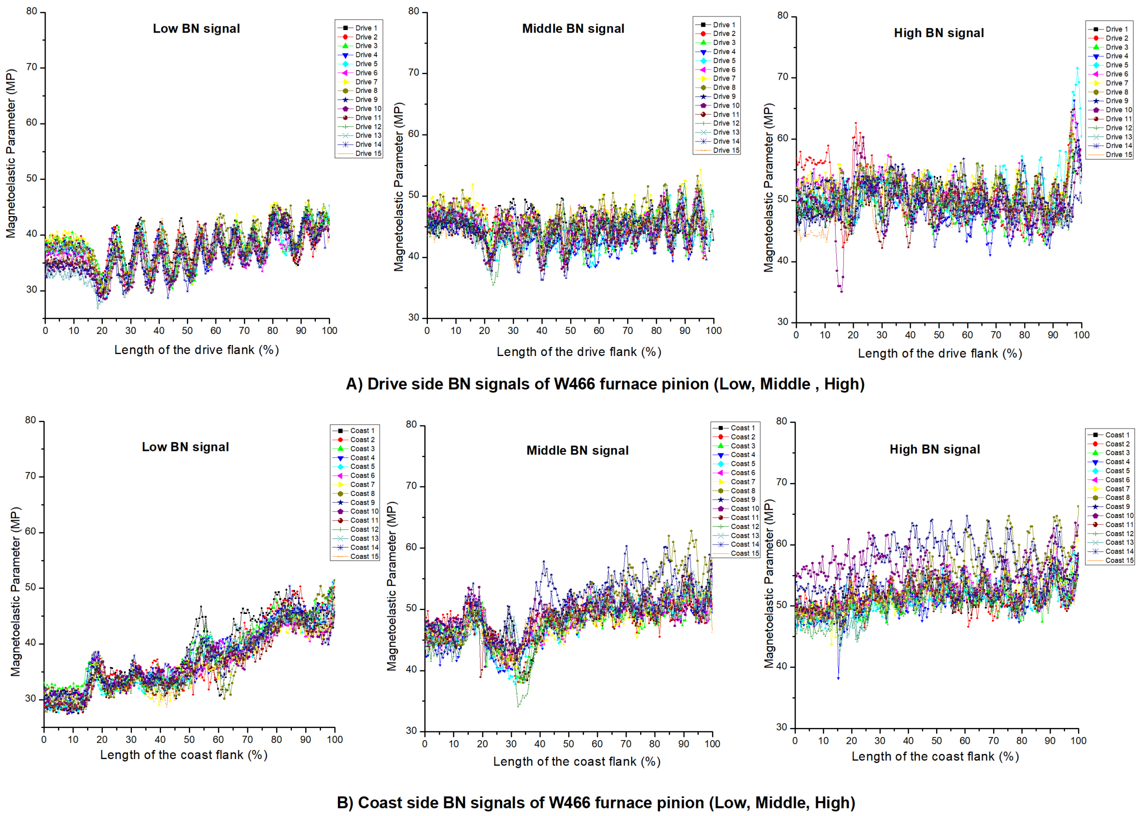

Figure 5.2: BN signal variation of drive and coast flanks of W466 furnace pinion

The main aim of the measurement is to understand the BN signal variation of the heat-treated furnace pinion on drive and coast at the 3 levels. As observed from the figure 5.2 on the drive side, the pattern of signals looks similar with a valley beginning at 20% length of the flank but with varying MP signals. On the coast side of the pinion, the observed pattern is different on all the levels of the flank with large scattering observed on the high level. The Barkhausen noise MP signals follow an increasing trend from the low to high levels of the flank on both the drive and coast side of the pinion. The MP values of all the flanks including drive and coast range between 28 MP to 75 MP. The observed variations in the pinion tooth are in relation to the microstructure and residual stress distribution until 60 - 100 microns depth from the surface. This signal variation explains the slight material in-homogeneity of the furnace pinion on the coast and drive flanks due to the heat treatment process of carburization, quenching & tempering. The locations of the pinions inside the furnace during the quenching process is an important factor as observed from figure 5.2.

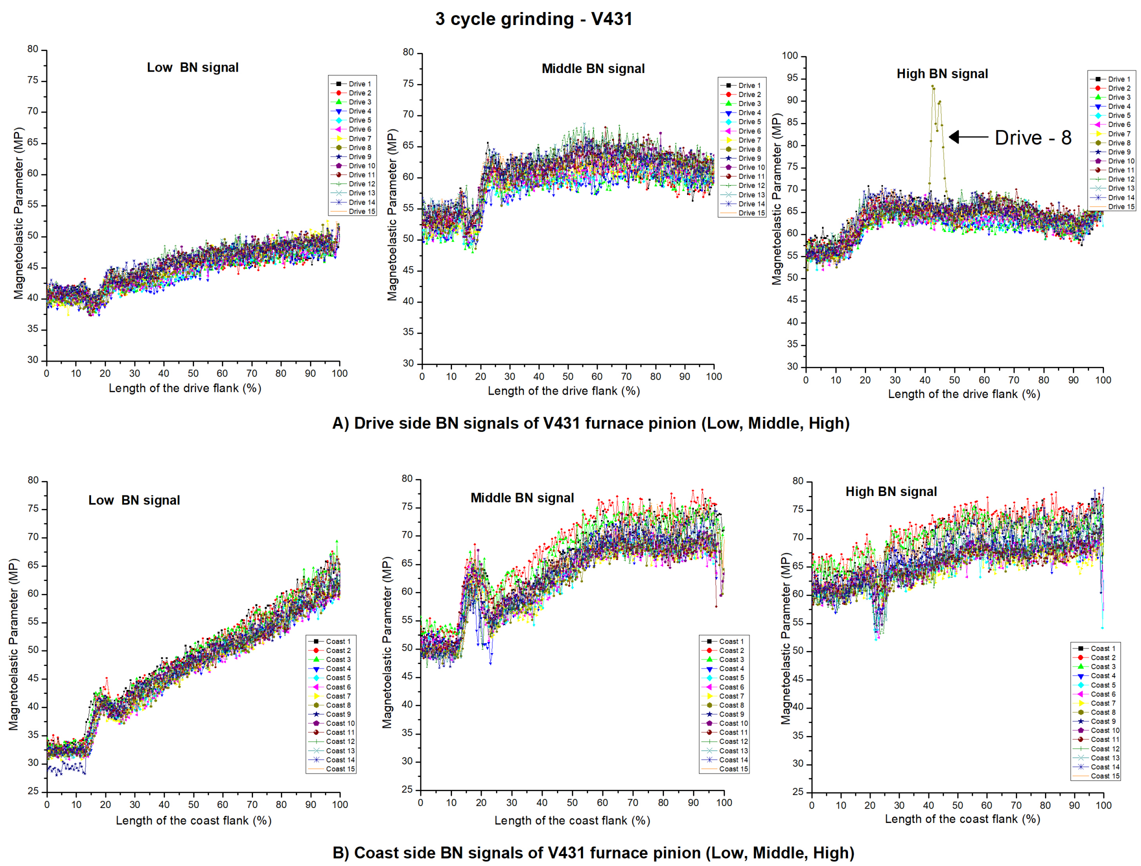

Figure 5.3: BN signal variation of drive and coast flanks of V431 furnace pinion

V431 sample is ground with 3 cycles with a material removal rate of 0.25 mm to 0.30 mm from the surface. Figure 5.3 illustrates the BN signals on the drive and coast flank of the pinion. The figure 5.3 (**A**) illustrates the drive side of the ground pinion on 3 levels. Similar to the W466 pinion, the low level of the flank emitted low BN signals between 35 MP to 50 MP on the 15 drive flanks. The middle and high level of the drive flank observed similar MP values. On the high level of drive flank, tooth 8 detected an unusual MP value between 40% to 50% length of the flank. The tooth has been measured again to check the validity of the signal and re-emitted the similar signal again. The explanation to this behaviour is the relieving of compressive residual stress at that particular location of the flank due to the high localized heat generated by grinding as a result of surface unevenness. The figure 5.3 (**B**) illustrates the coast side of the flank and an increasing trend of MP values are observed from the low to a high level of the flank. The increasing in MP values on the 3 levels of coast flank is due to the varying heat transfer nature on 3 levels. The low-temperature grinding is observed on the lower level of the flank and increasing temperature distribution is observed on the high level of the flank. Interestingly along the coast flank (0% - 100%) at the low level, the mechanical and thermal effects of the grinding process have an influence on the microstructure due to the high deviation in the MP values.

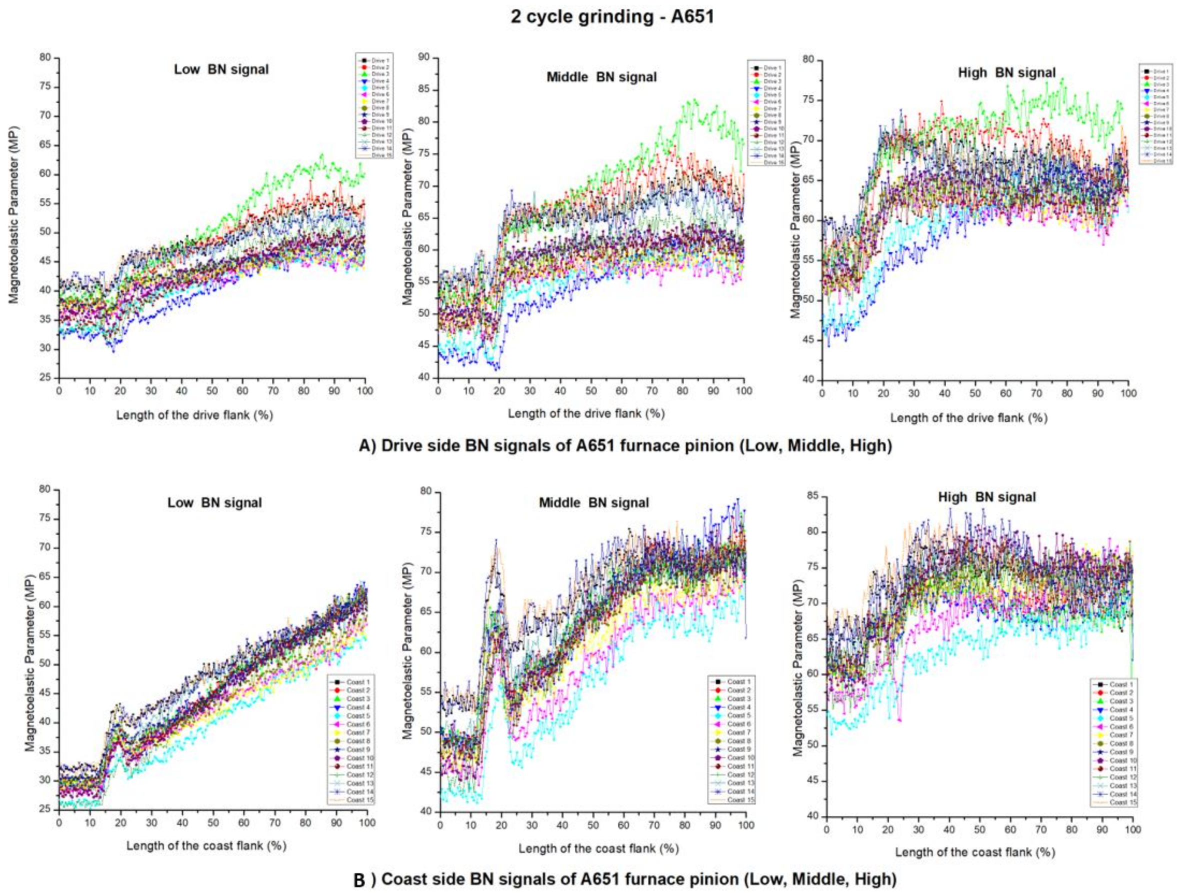

Figure 5.4: BN signal variation of drive and coast flanks of A651 furnace pinion

A651 pinion is ground with 2 cycles with a similar material removal rate of 0.25mm to 0.30 mm from the surface. As the same amount of material is removed from the surface with 2 cycles as compared with 3 cycles, it involves high thermal effects of the grinding process. The pinion speed (deg/sec) for the sample is also increased during the generation grinding process compared to the V431 3 cycle grinding as mentioned in table 5.1. The main objective is to understand the microstructure, residual stresses and retained austenite variations. Figure 5.4 illustrates the MP values of the drive and coast flank on the 3 levels. The figure 5.4 (**A**) analyzes the drive flank on 3 levels for 15 tooth. The low level of the flank detects lower BN signals compared to the middle and high levels. The low level ranges from 30 MP to 65 MP and the middle, high-level MP values ranges from 40 MP to 85 MP. A large scattering is observed on 15 drive flanks when compared with V431 pinion in figure 5.3. Due to the increase in temperature for each tooth gap in the grinding operation as it is a discontinuous generation grinding process (tooth by tooth grinding), the variation of MP values are observed. The figure 5.4 (**B**) reveals the BN signals of coast flank on 3 levels. The middle and high level of the coast flank observed the large scattering similar to the drive flank due to the rise in contact temperature between the pinion and the grinding wheel.

Figure 5.5 displays the comparison of the highest MP values on 3 levels (low, middle, high) for the drive and coast flanks on the 3 pinions. Figure 5.5 (**a,b,c**) illustrates the drive flank and (**a,b,c**) illustrates the coast flank. Comparing the ground pinions with the W466 furnace pinion, the MP values

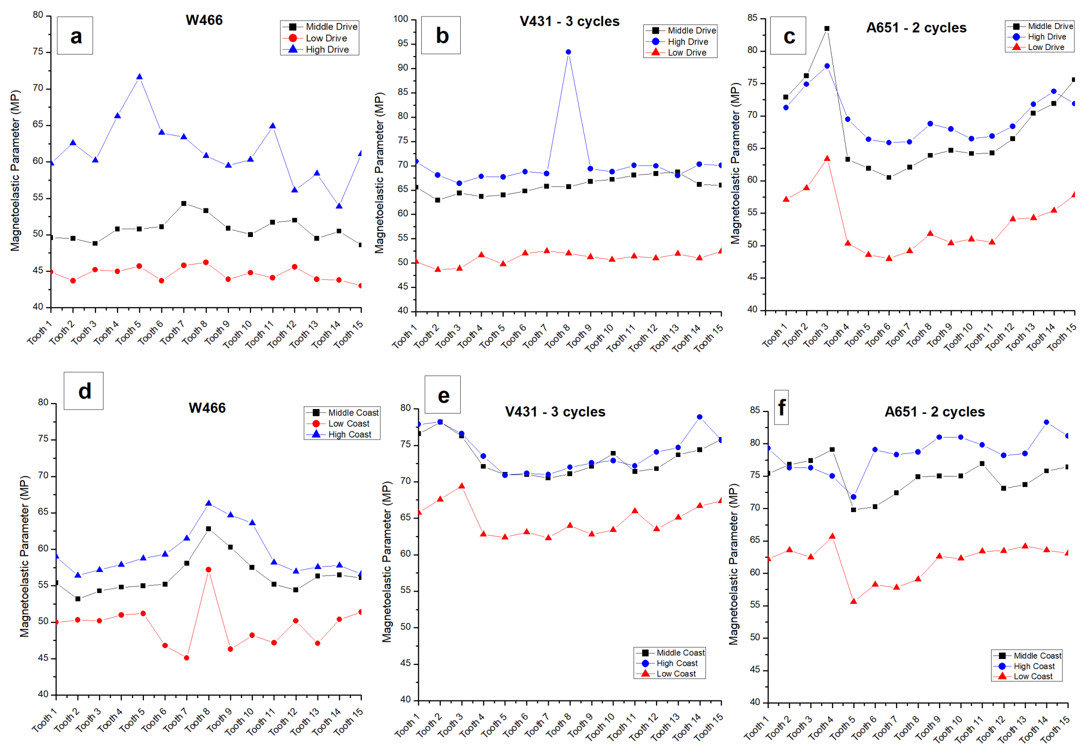

Figure 5.5: (**a,b,c**) illustrates the highest MP values on the drive flanks of W466, V431, A651 pinions & (**d,e,f**) illustrates the highest MP values on the coast flank of W466, V431, A651 pinions

observed the increasing trend due to the temperature rise. The low-level drive and coast flank detected the low MP values in all the cases. After the grinding operation, the middle and high level of the flank followed a similar range of MP values as observed in figure 5.5 (**b,c,e,f**). The grinding wheel forces are much higher on the middle and high level of the flank compared to the low level. In the figure 5.5 (**c**) graph, the MP values begins to increase from the tooth 4 until tooth 3. So the grinding of the tooth has begun from tooth 4 and as the grinding wheel performs the grinding at each individual tooth gap, the temperature rises even though the coolant supply is present.

After analysing the plotted Barkhausen data, it is understood that the 2 cycles grinding process involves high contact temperature compared to the 3 cycle process and the material characterization is needed for further understanding. As the BN signals only present the qualitative data, it is important to quantify and correlate the results. As the increase in contact temperature is observed on the high and middle levels of the flank compared to the low level, the middle level is selected for the further investigation considering the pinion contact pattern area with the crown gear. The mid-level of the pinion is much highly stressed than the other surface levels.

Figure 5.6 illustrates the Barkhausen noise signal variation comparison on 3 drive flanks from each pinion. The signals are detected from the mid-level of the flank as it is considered to be the lethal point due to the high stress zone. So any material damage at this location is considered to be very detrimental for the truck functioning. The furnace sample has the low value ranging between 40 MP - 45 MP and as the pinions undergo the grinding process with 2 different parameters, the MP val-

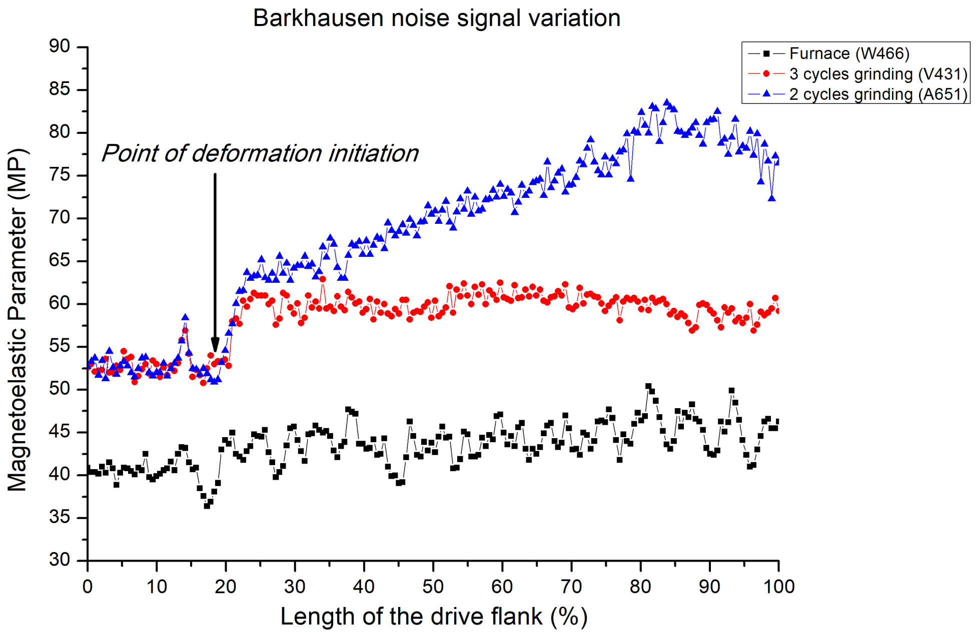

Figure 5.6: Barkhausen noise comparison on 3 samples of W466, V431 (3 cycles grinding) & A651 (2 cycles grinding)

ues increase due to the material transformations with respect to microstructure, hardness, residual stresses and retained austenite. The two different grinding parameters are not affecting the pinion flank until 20% of the length but the variation is seen from that position. At the 20% flank location, the grinding wheel and the pinion movement begins indicating the point of deformation initiation and as the V431 pinion is ground in 3 cycles with the pinion speed of 3.75 °/s, 3.75 °/s, 3.25 °/s the heat energy generated is dissipated with the proper coolant flow and observed constant value of 60 MP ± 2 from the 20% length of the flank. In the A651 flank, the MP values is in line with the V431 until the 20% length but as the movement begins high heat energy is generated and transferred until the length of the flank as observed in the figure 5.6. Even though the coolant supply is available, the heat energy is not completely dissipated and responsible for the high value of 85MP towards the end of the flank by beginning with 53 MP. The pinion speed is also high compared to V431 with 4.5 °/s in the 1st cycle and 3.5 °/s in the 2nd cycle.

5.1.2. Vickers hardness

The Vickers hardness analysis is done on 3 samples beginning at 0.1 mm from the case to 2.150 mm into the core with 33 indentations. Figure 5.7 reveals the Vickers hardness indentations at varying depths on the 3 samples. The average indentations diagonal length is around 20 microns.

The hardness measurements of 3 samples are plotted in the figure 5.8 with depth (mm) on the x-axis and Vickers hardness on the y-axis. The hardness of the W466 furnace sample is lower at the surface compared to the ground samples with 665±10 HV1 at 0.1 mm due to the presence of high fractions of retained austenite. The black dashed line on the W466 sample indicates the amount of surface removed by grinding process which is between 0.25 mm to 0.30 mm. V431 is measured 686.5±7 HV1 at 0.1 mm and the higher hardness values are observed on A651 sample with 723±7.5 HV1 at 0.1 mm. The A651 sample with 2 cycle grinding process observed high hardness fractions through-

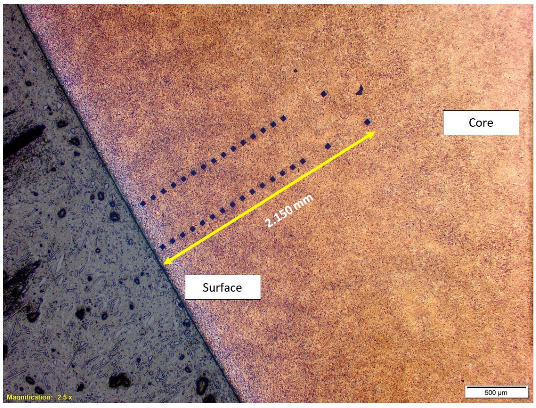

Figure 5.7: The vickers hardness diamond indentations are demonstrated from the surface to the core

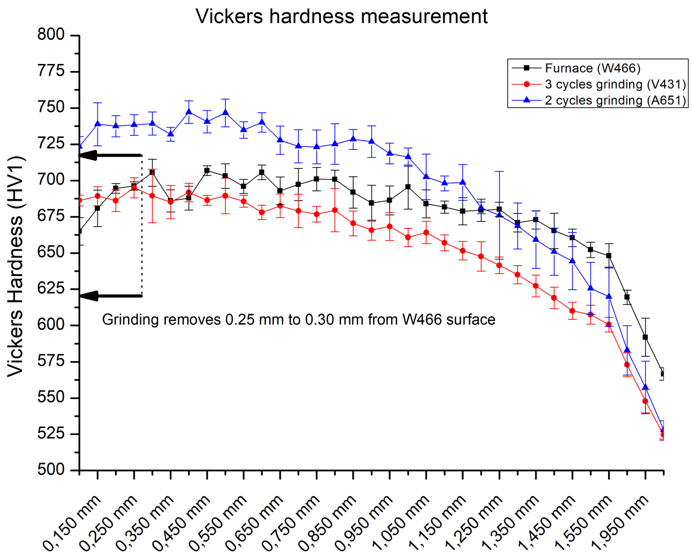

Figure 5.8: Vickers hardness analysis on 3 samples (W466 - black, V431 - red, A651 - blue). The black dashed line indicates the surface removal region by grinding in W466 furnace sample

out the case depth i.e. until 1.9 mm when compared with V431 sample. The plastic deformation generated due to the high material removal rate within 2 cycles resulted in an increase in hardness. The V431 sample exhibited the lower hardness values even though with low BN MP values when compared with A651, which is contradicting the BN principle. The unevenness of hardness fraction throughout the measurement length in all the samples is due to the presence of the amount of tempered martensite & retained austenite fractions at the indentation locations.

5.1.3. Microstructure analysis

The optical microscopic images of the 3 samples are illustrated in the figures below. Figure 5.9 reveals the W466 furnace sample consisting of tempered martensite microstructure, retained austenite and ϵ- carbides due to low-temperature tempering obtained after carburization, quenching and 1st stage tempering. The ϵ- carbides are not visible through optical microscope and even with SEM due to the nanometer (nm) in size. The sample is etched with 4% HNO_3 + 96% ethanol (nital etchant) for 8 seconds. The tempered martensitic microstructure is observed in the light/dark grey in colour and the retained austenite in white colour. There is no apparent visibility of carbide precipitation. The dark colour is due to the precipitation of ϵ- carbides as they etch darkly than untempered martensite. As observed, large fractions of blocky retained austenite are present at the surface of the furnace sample. The retained austenite is present due to the incomplete transformation of austenite to martensite during quenching in the furnace as the M_f temperature is below the room temperature. At the surface, the plate martensite is observed due to the high carbon concentrations and as we go into the core, lath martensite is observed due to the low carbon concentrations. Figure 5.10 illustrates the V431 3 cycle ground sample tempered martensite microstructure. The large fractions of retained austenite present in the W466 sample at the surface are removed by grinding process and as observed visibly, the quantity is decreased. The 2 cycle A651 sample microstructure is observed in figure 5.11 and the plastically deformed region is observed at subsurface due to the high grinding forces generated as a result of higher depth of cut. The ground samples V431 and A651 microstructures are affected with the varying grinding parameters. All the samples consist of MnS inclusions as received by the supplier. In figure 5.11 reveals the two sites where the inclusions are visible.

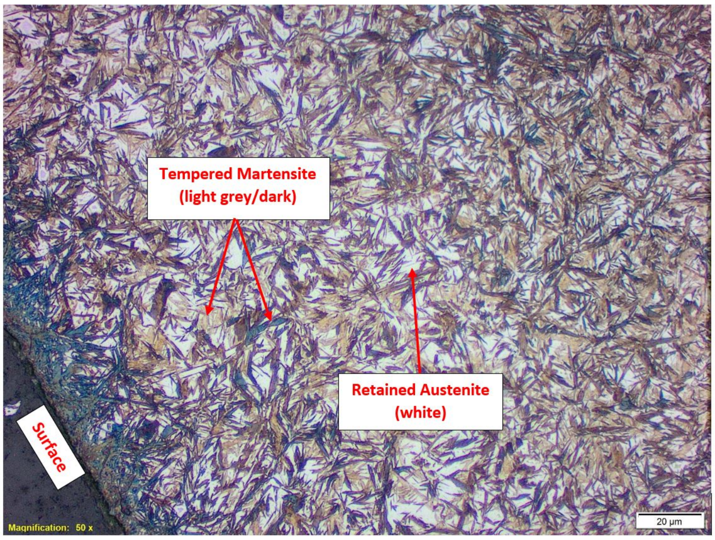

Figure 5.9: W466 Furnace sample microstructure with tempered martensite i light/dark grey and retained austenite in white color

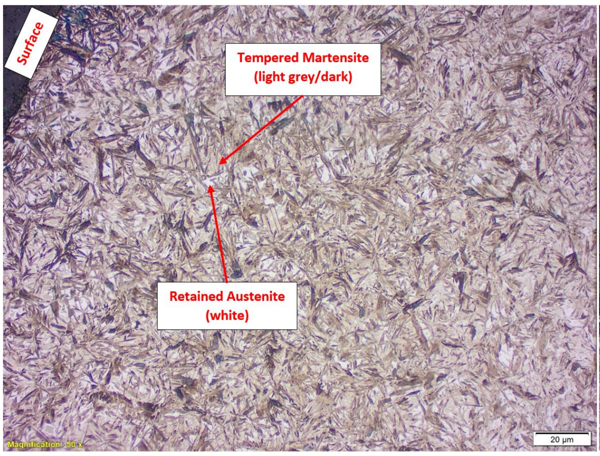

Figure 5.10: V431 (3 cycle ground) sample with tempered martensite and retained austenite microstructure

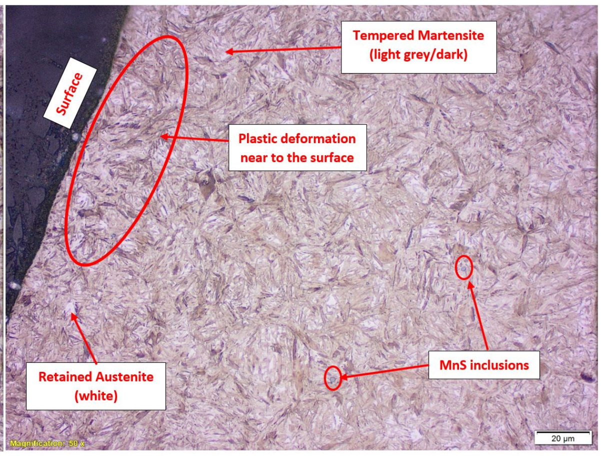

Figure 5.11: A651 (2 cycle ground) sample with plastic deformation region near to the surface and visible MnS inclusions

5.1.4. X-ray diffraction

The x-ray residual stress measurements from the surface to 0.5 mm depth is performed on 3 sample tooth along the longitudinal direction (-90°) which is also defined as along the flank. Figure 5.12 illustrates the plot and as observed, the furnace sample (not ground) has the highest compressive residual stresses of -392 ± 19 MPa on the surface which is generated in the quenched and tempered heat treatment process and the grinding process removes around 0.25 - 0.3 mm surface from the furnace sample to improve the surface topography. This resulted in the reduction of compressive residual stresses on the ground samples. On the V431 surface -138 ± 12.1 MPa is measured and on A651 sample -49 ± 10.1 MPa is measured using x-ray diffraction method. As observed, 3 cycle grinding processes is resulting in better compressive stresses at surface and subsurface regions. Due to the high frictional heat generation on 2 cycle process, the compressive stresses slightly relaxed and shifted towards tensile stress direction near to the surface until 0.05 mm depth.

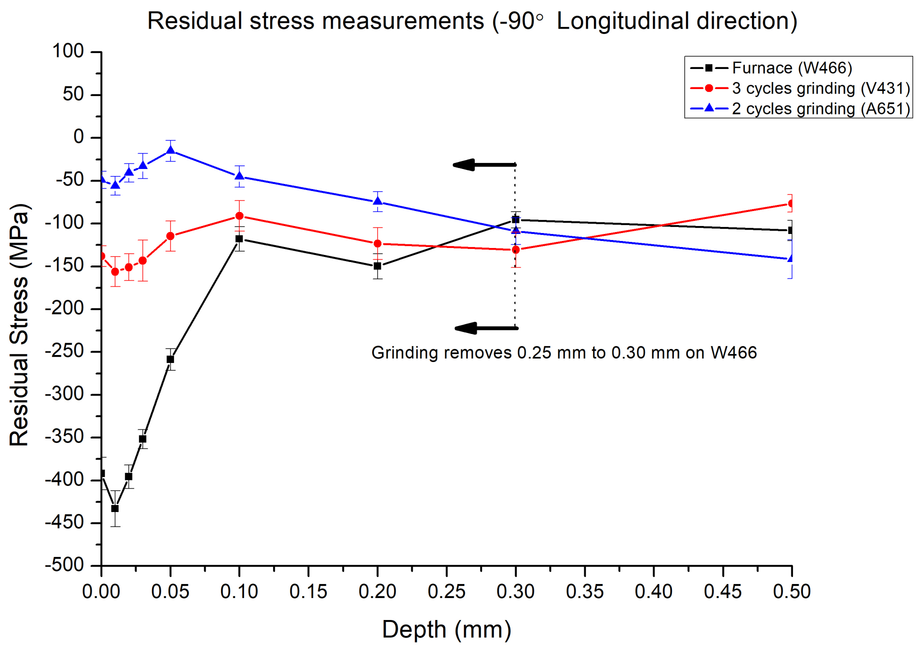

Figure 5.12: Residual stress measurements on 3 samples W466, V431 & A651

The retained austenite fractions of the 3 samples are revealed in figure 5.13. The retained austenite fraction increased from 20.7 ± 1.9 % at the surface to 38 ± 4.6 % at 0.03 mm depth in the furnace sample and observed a decreasing trend until 0.5 mm. As the M_f temperature is below the room temperature on the surface due to high carbon concentration compared to the subsurface and core, large fractions of the retained austenite are observed. For the sample V431 (3 cycles), 37.1 ± 3.4 RA% is observed and as the grinding cycles are reduced to 2 for A651 sample in removing the similar material from the surface, the frictional heat and mechanical forces generated in the rough process transformed the unstable retained austenite into a stable phase with only 24.2 ± 3.5 RA% on the surface. The high pinion speed affected the thermal and mechanical stability of the retained austenite until 0.5 mm when compared to V431 3 cycle grinding process.

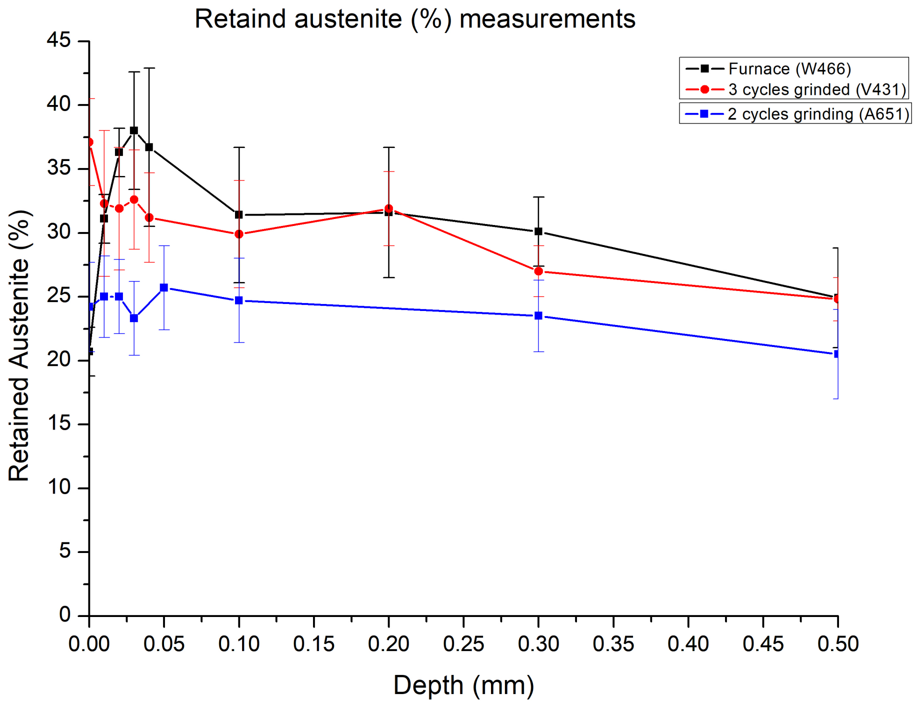

Figure 5.13: Retained austenite fractions on 3samples W466, V431 & A651

5.2. Part 1 : Discussion

In the present research question, 2 samples with varying pinion speed and grinding cycles are examined in comparison with the furnace pinion. The Barkhausen noise analysis indicated that as the pinion speed increases in both the cycles as mentioned in table 5.1, the magnetoelastic parameter (MP) shows an increasing trend due to the variations in residual stresses and microstructure in relation to the magnetic domain pinning. Grinding is basically an abrasive particle interaction on the pinion workpiece. So the total amount of grinding energy produced by the interaction consists of ploughing, sliding and formation of chips [47]. The heat associated with the energy produced is carried away by the pinion, coolant fluid, ground chips and the abrasive grinding wheel. As understood only a fraction of heat generated by grinding energy is observed by the pinion, which is causing the pinion temperature to rise and eventually relax the compressive residual stresses. The Barkhausen noise analysis of W466 pinion (not ground) explains that the furnace heat treatment process on the drive and coast side is not constant. The positioning of the pinions inside the furnace is influenced by the quenching and tempering effect forming varying fractions of retained austenite and tempered martensite. The residual stresses and retained austenite depth profiles vary in the drive and coast flanks which further influence the pinions during the grinding operation.

The variation of Barkhausen noise signals along the flank with high MP value deviation is due to the non-uniform geometry interaction of grinding wheel with the pinion on high, middle and low levels. The low level of the flank always observed low-intensity BN signals due to the proper functioning of grinding coolant flow at the bottom regions and insufficient flow at the high and middle regions. Another perspective is the grinding wheel cutting depth at the certain locations varies from the tip to root of the flank.

In the 2 cycle processed A651 pinion, scattered BN signals from tooth to tooth is observed in figure 5.5 (**C**). With the grinding beginning at tooth 4, the temperature increase resulted in higher BN signal detection until tooth 3 where the grinding stops. The heat dissipation on the grinding wheel or the coolant flow due to the high pinion speed caused this phenomenon. As the depth of cut is large in this process to remove the 0.3 mm surface in two cycles, the pinion experiences plastic deformation at the surface and subsurface regions as observed in figure 5.11 which tends to increase the number of pinning sites like dislocation density, lattice strain due to metastable retained austenite transformation. This behaviour explains the increase in hardness in the A651 2 cycles process compared to the 3 cycle process V431 sample. The retained austenite fraction is also approximately 10% lower at the surface compared with 3 cycle process. The increased BN signal in 2 cycle process is mainly affected due to the reduction of compressive residual stresses with the heat input into the material. So the BN signal MP value will be higher even though the material has higher hardness as it is also dependent on the stress state of the material. This explains us about the easy domain wall motion tending towards the tensile stress zone indicating high MP value. Gorgels and Klocke [19] noticed the similar BN signal increase by varying grinding parameters with increased material removal rate.

5.3. Part 2 : Material characteristics of grinding-induced burns

In this section, the characterization of grinding induced burns are done in relation to Barkhausen noise detection method. Figure 5.14 illustrates the sample flow chart selected for the characterization. K220 pinion is used in this study to understand the microstructural properties with varying intensity of the grinding-induced burn. 3 MP values 125 MP, 165 MP & 35 MP which are detected using Barkhausen noise method on 3 separate teeth is studied in this section. These are the values of each tooth with the highest BN signal at a particular location. At DAF trucks pinions production site, the pinions above 100 MP BN signal is considered to be faulty ones. But the particular features considering microstructure, residual stress, retained austenite is not known for the samples above 100 MP and it is, therefore, a question to investigate its properties.

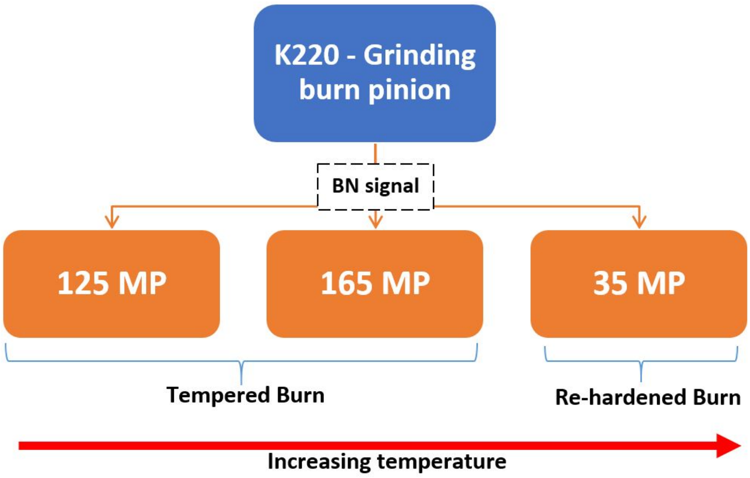

Figure 5.14: Grinding induced burns sample flowchart

5.3.1. Barkhausen noise analysis

The Barkhausen noise signals of K220 pinion after the grinding process are plotted in figure 5.15 using data collected by Viewscan. The x-axis represents the length of the flank and y-axis represents the Magnetoelastic Parameter (MP). As there are 15 tooth on the pinion and each tooth consists of a drive and coast flank, the graph represents 30 measured flanks. As per the quality check, the received signals of a normal pinion must be between 45 MP to 100 MP as shown in figure 5.15 which signifies function-able tempered martensite microstructure. The structure <45 MP signifies hard brittle structure with compressive stresses and >100 MP signifies softer microstructure or possibility of tensile stresses. The pinion clearly indicates the presence of grinding induced burns on half of the flanks.

The detection is also done on the high and low levels apart from the middle level of the flank to observe the area spread of grinding induced burns. The trend of low, middle and high levels of the pinion is plotted in figure 5.16. The trend is plotted for the drive side of the tooth as the coast side didn't generate any thermal damage during the grinding operation. The x-axis represents the highest BN signal on the particular tooth level and the y-axis represents the MP values. As observed the high and middle level observed the thermal damage in all the tooth. The grinding process begins at tooth 1 and as the process continue the MP value increase tooth by tooth indicating the increasing rate of thermal damage. The MP value increases until tooth 8 and begins to drop suddenly to 35 MP on tooth 10 at the middle level. This indicates the tooth 10 has crossed the austenitization tempera-

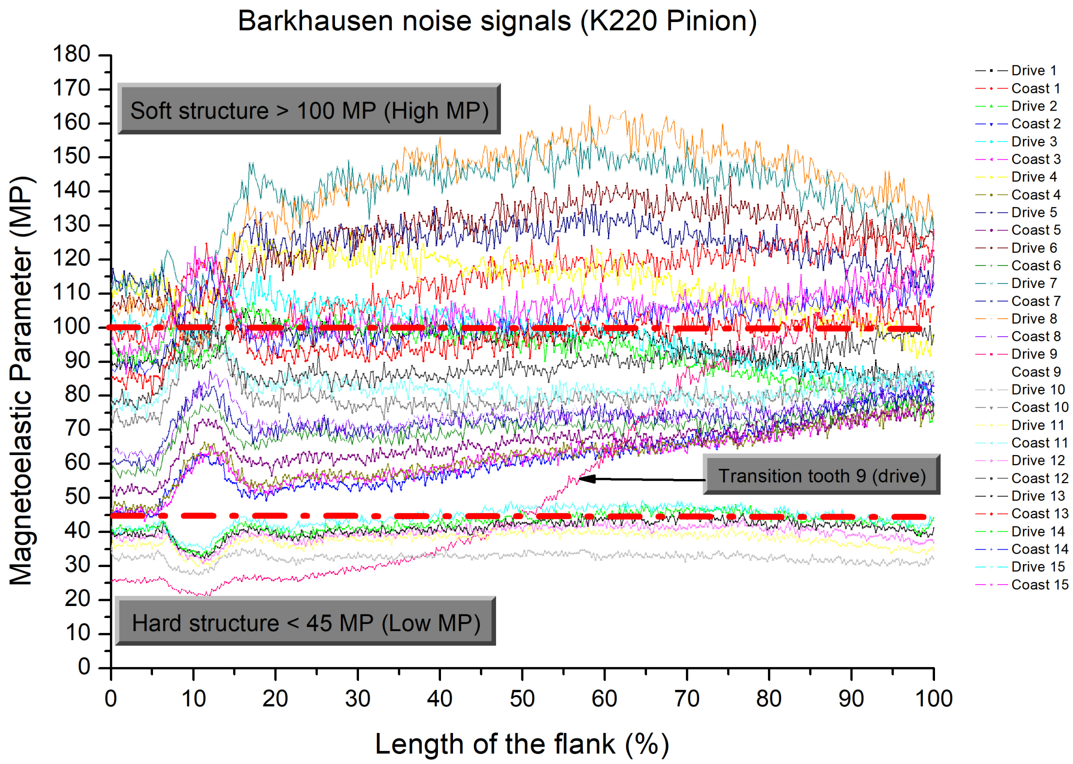

Figure 5.15: Barkhausen noise detection of K220 pinion on middle level (drive and coast)

ture of the steel during the grinding process and quenched in the presence of the coolant creating a hard brittle martensite structure. Until tooth 8 the over-tempering process of the microstructure has occurred. The tooth 9 is the transition tooth where the temperature begins to go above the austenitization range. The transition tooth 9 is also observed in figure 5.15 where the signal on the flank have a curved structure. The exact value of the temperature is unknown as the process takes place in a closed environment. As mentioned in figure 5.16, 3 tooth samples were selected for further investigation.

The Barkhausen signals of the 3 samples are plotted in figure 5.17. The 125 MP and 165 MP samples have a similar pattern until 15% of the length and then the signals vary depending on the thermal damage initiation. The Re-hardened burn is indicated in the blue colour with constant signal detection throughout the flank indicating a uniform microstructural feature.

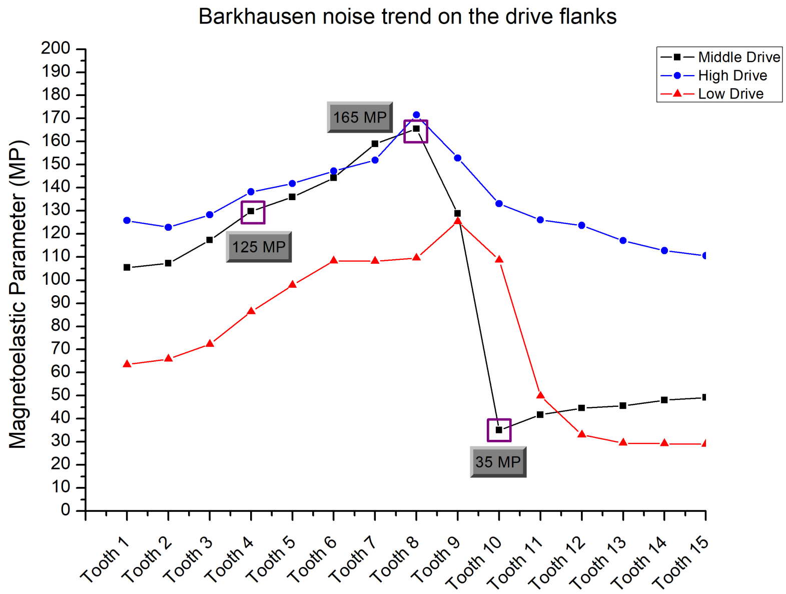

Figure 5.16: BN trend in high, middle and low levels for drive tooth. The selected drive tooth for the material characterization is represented in the box.

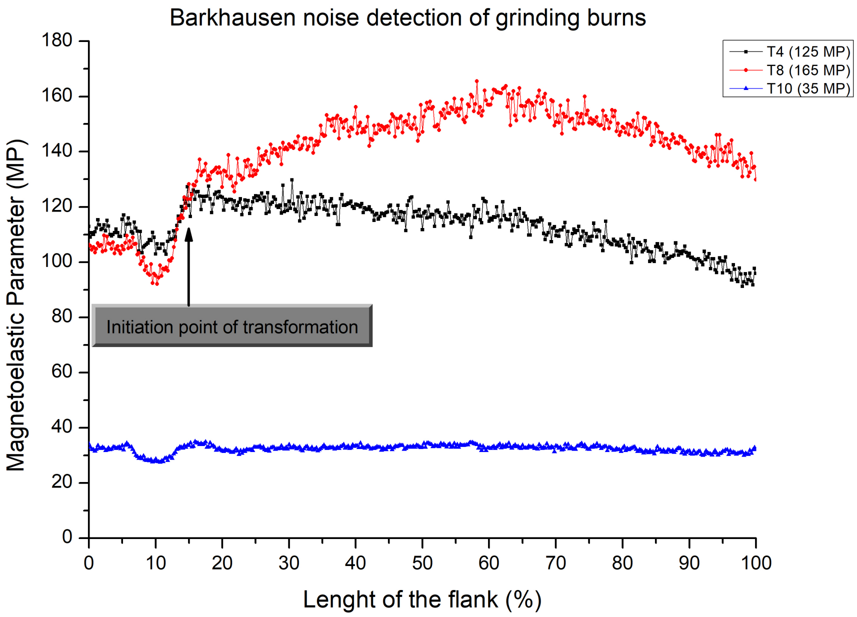

Figure 5.17: Barkhausen noise signals of 3 samples of varying intensities. At 20% length of the flank, the initiation point of deformation begins.

5.3.2. Macro inspection

After the Barkhausen noise detection process, the 3 tooth are etched with nital solution to observe the discolouration. Tooth 4 with 125 MP didn't observe any discolouration indicating no thermal damage on the tooth surface. Figure 5.18 illustrates the 2nd step of the quality check process of pinions using nital without destructing for tooth 8 and tooth 10. In the (**a**) the dark etched region is observed along the flank length for 165 MP value confirming the BN signal detection process of thermal damage. The (**b**) part of the figure reveals the re-hardened burn which also confirms the 35 MP BN signal of hard structure.

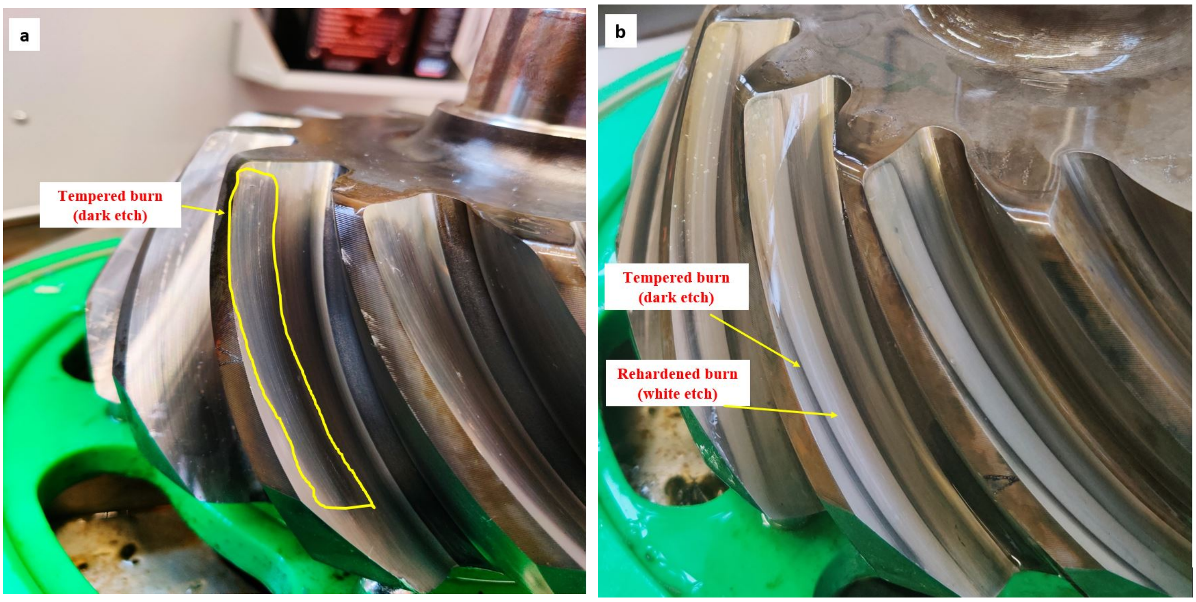

Figure 5.18: Macro etch procedure on the selected tooth **a)** Tooth 8 with 165 MP observed discoloration along the length of the flank, **b)** Tooth 10 with 35 MP indicated re-hardened burn with white etched region surrounded by dark etch region

The pinion is cut-sectioned and the samples are prepared for the Vickers hardness and microstructural analysis. Figure 5.19 reveals the crossectional cut of the samples with **a)** tempered burn on tooth 8 and **b)** re-hardened burn on tooth 10. The nital etch process only discolours the location with thermal damage whereas the Barkhausen noise illustrates the intensity of the burn with varying MP values. This is a useful process in making a qualitative statement about the burns.

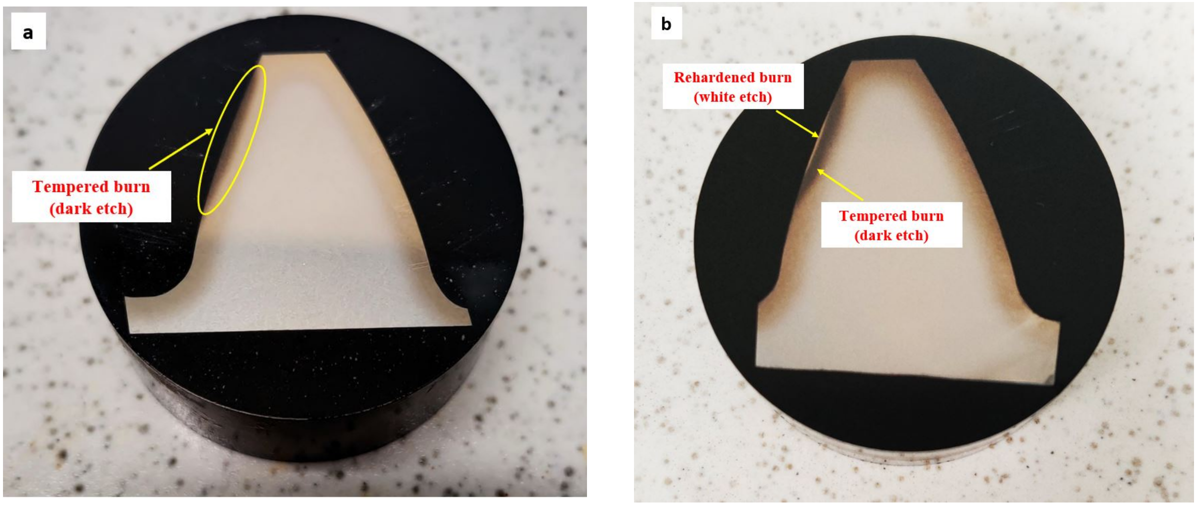

Figure 5.19: Nital etch on the crossection to identify the burn location for hardness and microstructure analysis **a)** Tooth 8 (165 MP) **b)** Tooth 10 (35 MP).

5.3.3. vickers hardness

The hardness profile of the samples is plotted from 0.100 mm depth from the surface to 2.150 mm depth to evaluate the burn depth. The case hardened depth (CHD) of the ideal pinion without burn presence is 1.9 mm with 550 HV1 and the hardness from the surface to 1.1 mm depth has to vary between 660 HV1 - 750 HV1 (i.e 58 - 62 HRC). Figure 5.20 reveals the depth profile for 3 varying BN signals. The tooth 4 with 125 MP value has 706.6 HV1 at the surface and the hardness is above 700 HV1 until 1.1 mm of the CHD indicating no grinding induced burn presence as confirmed by the macro etching process. The tooth 8 with 165 MP value suffered high thermal damage until 1.5 mm depth from the surface. The hardness at 0.1 mm depth from the surface is 603.6 HV1 which is significantly low indicating the softer microstructure. The tempered martensite starts to over-tempering losing its hardness properties by the carbon dissolution into the surrounding matrix. Tooth 10 with 35 MP value measured 771.5 HV1 at 0.1 mm depth from the surface which is beyond the limit indicating a harder brittle martensite structure. Surrounding the re-hardened burn, the tempered burn is observed from 0.25 mm depth damaging the whole case until 1.9 mm from the surface.

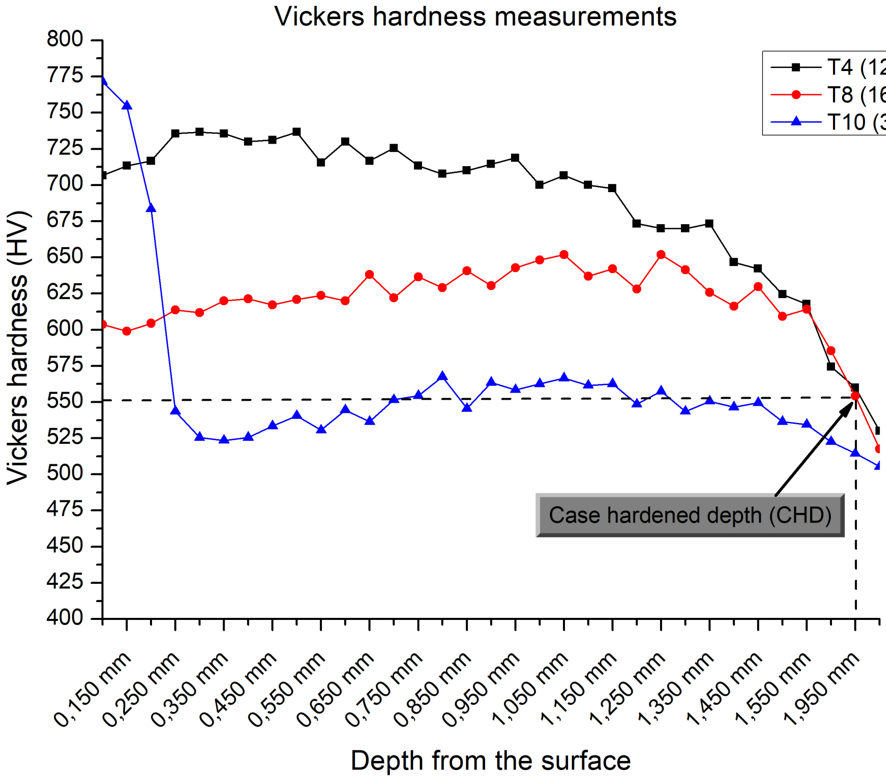

Figure 5.20: Vickers hardness depth profile for the 3 varying BN signals.

5.3.4. Microstructural analysis

Tempered burn

The microstructural analysis of the 125 MP, 165 MP is performed using nital etching technique to reveal the microstructure. Figure 5.21 reveals the microstructure of tooth 4 with 125 MP Barkhausen noise signal. The arrow indicates the direction from the surface to the core as mentioned in the figure. The tempered burn is not present at this 125 MP particular value confirming the Vickers hardness and macro etch process. Even though tooth 4 observed increased value of 125 MP, the microstructure and hardness profile didn't show any significant change compared with ideal pinion below 100 MP values. This theory concludes the necessity to perform the x-ray residual stress analysis to study the domain wall motion of 125 MP sample.

The tooth 8 with 165 MP BN signal sample is etched and revealed in figure 5.22. The dark etched region at the surface indicates the grinding induced over-tempered burn. The thermal damage is observed in figure 5.22(**a**) until 700 microns depth from the surface which is 36% of the CHD. But the Vickers hardness depth profile revealed that the damage is observed until 1.5 mm from the surface as shown in figure 5.20. Figure 5.22(**b**) reveals the tempered burn microstructure with decomposed retained austenite and over tempered martensite. At this magnification range in an optical microscope, it is difficult to observe the carbides precipitation formed due to over-tempering. Figure 5.22(**c**) reveals the microstructure of the burn magnification zone. Even though much of the retained austenite has decomposed, few fractions of blocky retained austenite with high thermal

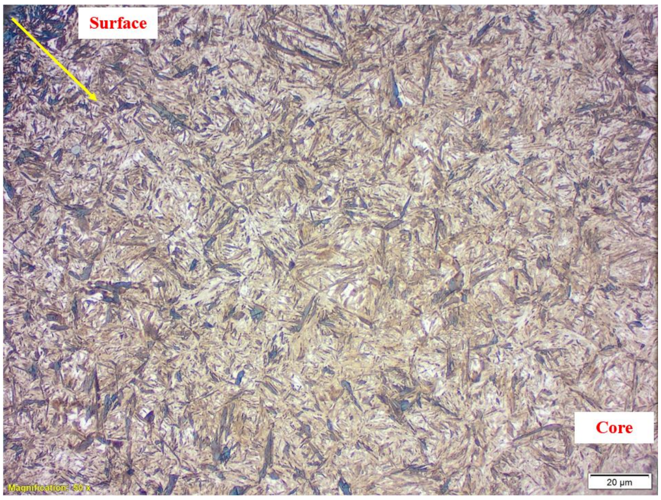

Figure 5.21: Tempered martensite microstructure of 125 MP Barkhausen noise signal at the surface.

stability are visible. The growth of small spherical carbides are seen at few locations as shown in figure 5.22(**c**)). As the grinding process increases the localized temperature to a certain level, the zones experience 3rd stage or 4th stage tempering leading the carbide precipitation.

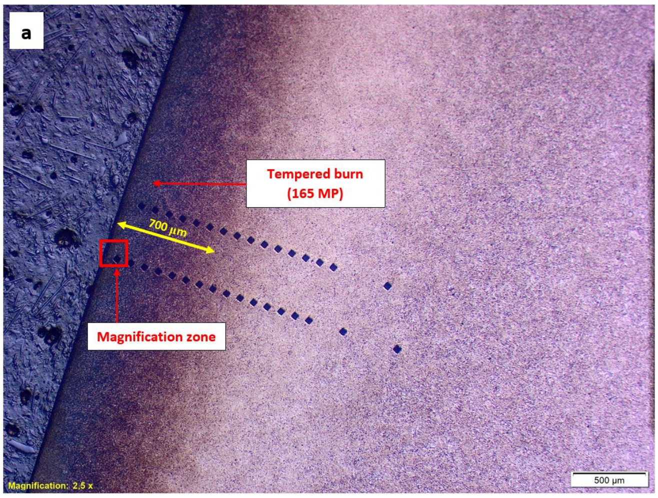

Re-hardened burn

The tooth 10 with a sudden drop in Barkhausen noise signal to 35 MP at the middle level is observed in figure 5.16. The Barkhausen noise detects until 60 to 100 microns from the surface. As revealed in the figure 5.23(**a**)), the white etched re-hardened zone is formed to a maximum depth of 250 microns from the surface and the tempered burn surrounded it until further 400 microns depth. The austenitization temperature generated due to grinding wheel contact with the pinion tooth surface reached only until 250 microns and beyond that, the temperature is just below the austenitization range. When quenched by the grinding coolant flow, the re-hardened zone created at the near-surface surrounded by the tempered burn zone.

Figure 5.23(**b & c)** illustrates the higher magnification optical microscopy and scanning electron microscope images of red square box from figure 5.23(**a**)). The white zone in the (b) is the freshly formed fine plates of martensite with small fractions of retained austenite. The dark region towards the right in (b) is the over-tempered microstructure with higher thermal damage when compared

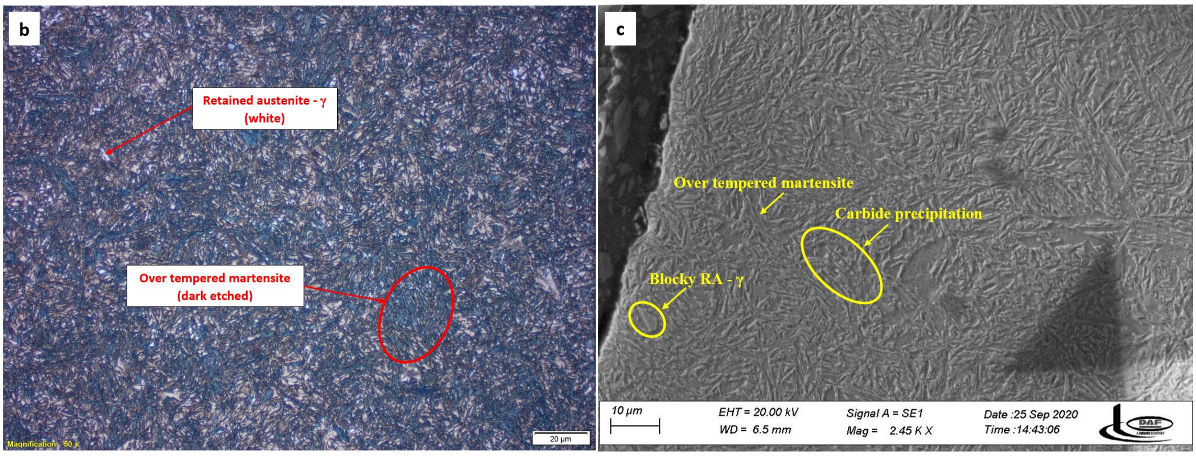

Figure 5.22: Tempered burn on tooth 8 with 165 MP Barkhausen noise signal **a)** 2.5x magnification image of burn site. The red square indicates the magnification zone for **b)** and **c)**. **b)** reveals the optical microscope image of the burn site and **c)** reveals the SEM image with the retained austenite and over-tempered burn.

to tooth 8 165 MP tempered burn. This can be understood by observing the Vickers hardness depth profile from figure 5.20. In the hardness profile, the tempered zone surrounding the re-hardening zone observes hardness below 550 HV1 from the depth of 250 microns which indicates the tempered martensite has completely lost its tetragonally structure by carbon diffusion to form fine phases of ferrite (α) and Fe_3C particles. The figure 5.23(**c**) illustrates the SEM image of the same zone to analyse the freshly formed martensite but it's not clearly visible. The red box indicates the magnified zone of (d) and yellow indicates for (e). In figure 5.23(**d**), the fresh martensite image is obtained through backscattered diffraction (BSD) option in SEM. The fine plates and twinned martensite is observed with blocks of retained austenite distributed randomly and the presence of carbides are not seen. In this zone, high hardness is observed with 770 HV1 at 0.1 mm depth from the surface. The figure 5.23(**e)** is the secondary electron image from SEM of over-tempered structure which has hardness of around 550 HV1 at 0.1 mm depth.

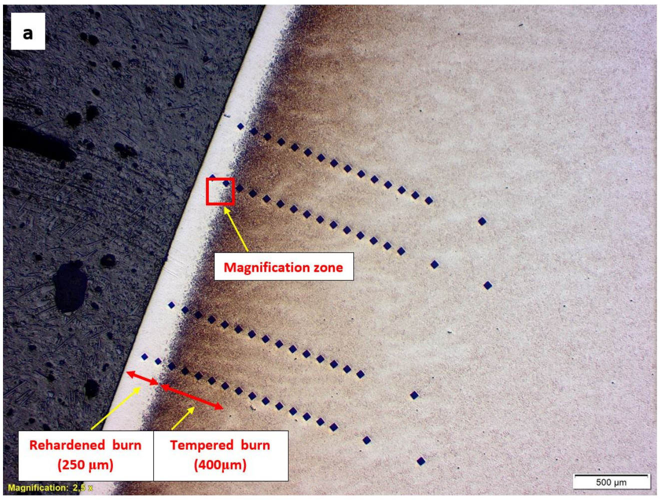

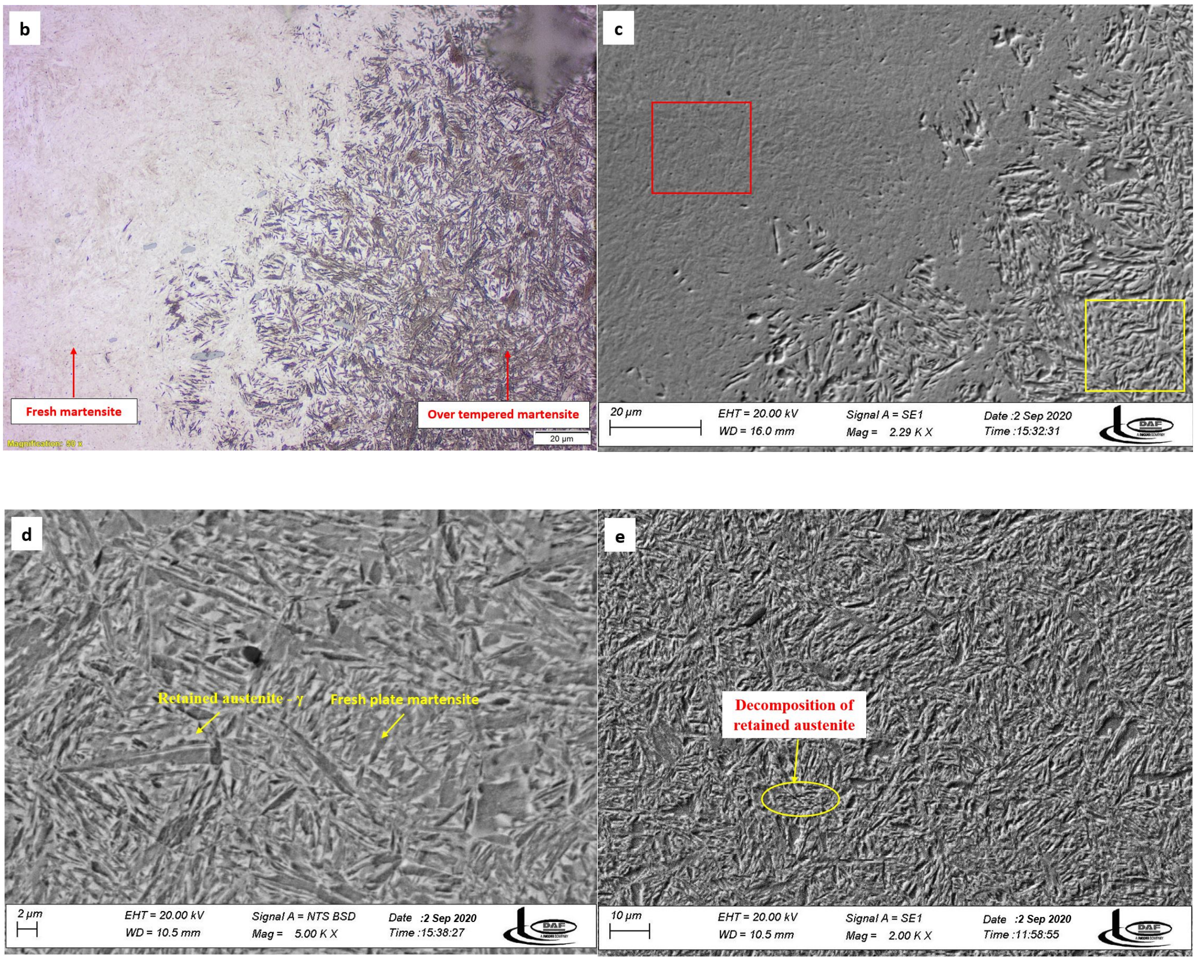

Figure 5.23: Re-hardened microstructure of tooth 10 with 35 MP. (**a**) Burn zone depth profile, (**b**) optical microscope 50x magnification of transition zone between re-hardened burn and tempered burn, (**c**) SEM image and red indicates locations for figure (d) and yellow box indicates the location for figure (e), (**d**) back scattering diffraction image of re-hardened zone and (**e**) reveals the SEM secondary electron image of tempered burn zone.

5.3.5. X-ray diffraction

The x-ray diffraction results of the 3 varying burn intensity samples are illustrated in figure 5.24. Figure 5.24(**a**) represents the residual stress measurements performed along the longitudinal direction. The tooth 4 with 125 MP BN signal consists 90.8 ± 7.1 MPa tensile residual stress at the surface and observed an increasing trend until 0.02 mm with 170.2 ± 10.9 MPa RS and stays in tensile range until 0.3 mm from the surface. Even though, the 125 MP consists of hardness and microstructure similar to BN signals below 100 MP, the presence of tensile residual stress increased the BN signal level. The retained austenite fractions measured using x-ray diffraction resulted 25 ± 1.9 % at the surface which is quite normal as shown in figure 5.24 (**c**)

Tooth 8 with 165 MP value resulted in -100.7 ± 8.6 MPa at the surface and increased significantly to 446.5 ± 8.1 MPa at 0.01 mm depth indicating the enormous thermal damage and at the depth of 0.35 mm 561.7 ± 9.1 MPa is observed and throughout the measurement until 0.5 mm, the residual stress profile is in tensile range as observed in figure 5.24(**a**). The retained austenite fractions in tooth 8 has lowered significantly to 12,9 ± 2 % at the surface as shown in figure 5.24(**c**). The fractions showed a constant trend until 0.5 mm depth. This indicates the decomposition of retained austenite is observed due to the high-temperature involvement.

As the re-hardened burn reached above the austenitization temperature of the steel, when quenched with grinding coolant formed fresh martensite and introduced compressive residual stresses until the depth of 0.10 mm and the tensile residual stress begins from 0.15 mm reaching a maximum of 529.7 ± 6.4 MPa at 0.5 mm as noticed in figure 5.24(**a**). The retained austenite fraction at the surface is 20.6 ± 0.5 % and following a decreasing trend. The decreasing trend is due to the decomposition RA fractions in the tempered burn zone from 0.25 mm depth.

The FWHM results are plotted in figure 5.24(**a**) and the trend is similar to the hardness depth profile observed in figure 5.20.

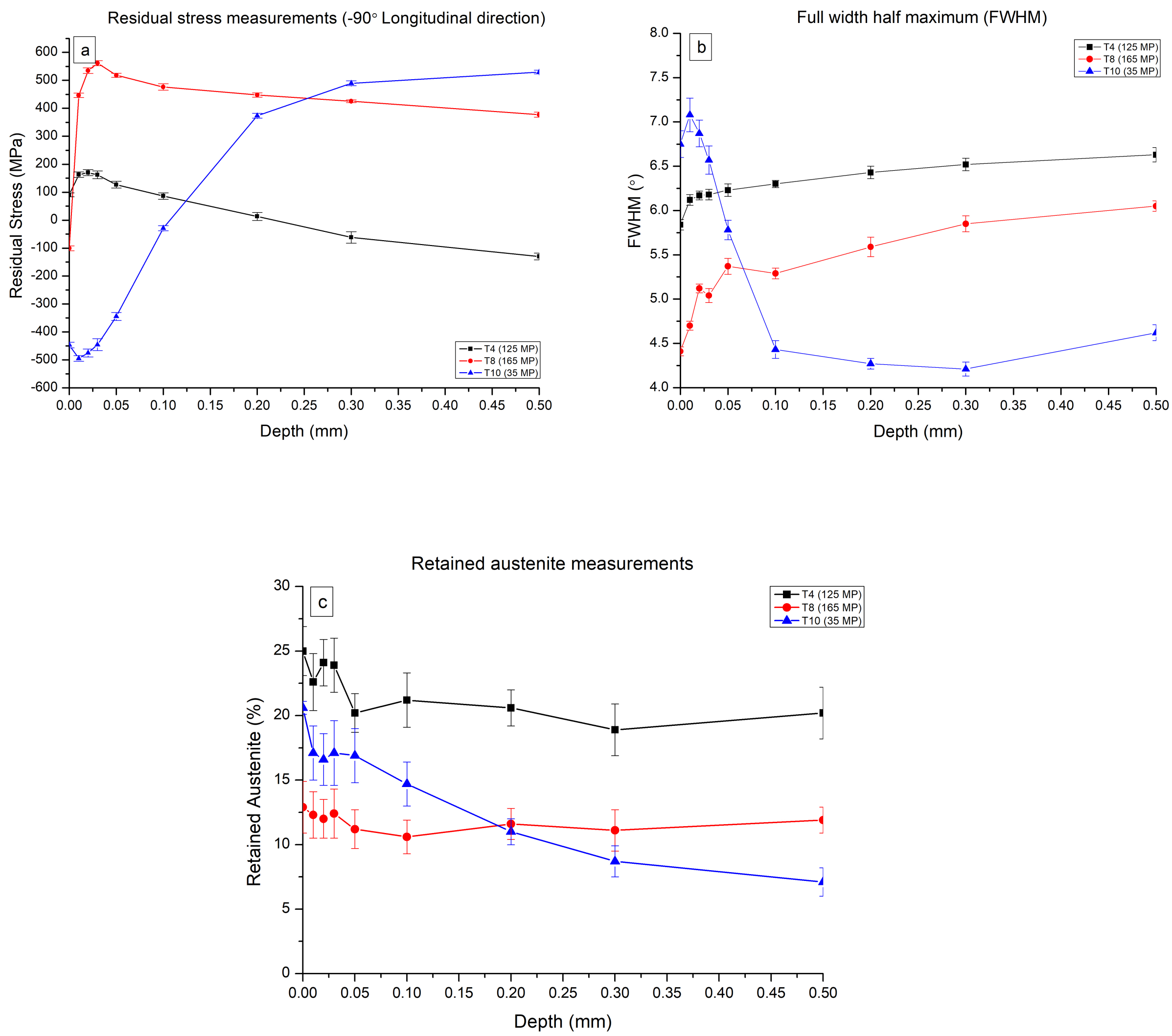

Figure 5.24: The x-ray diffraction results of the grinding burn samples of varying Barkhausen noise intensity. (**a**) residual stress measurement performed on longitudinal direction on 3 samples, (**b**) Full width half maximum depth profile on 3 burn samples, (**c**) Retained austenite fractions measured on 3 samples

5.4. Part 2 : Discussion

The present section discusses the material characterizations of grinding induced burns in 3 varying BN signal intensity samples 125 MP, 165 MP and 35 MP which are the order of increasing temperature. All the samples are from K220 pinion. The Barkhausen noise signal analysis of the K220 pinion is illustrated in figure 5.15 and the pinion tooth flank trend is observed in figure 5.16. The varying intensities of MP values are caused by varying temperature range during the grinding process. The grinding parameters are similar to the A651 (2 cycle process) pinion from part 1 question. Even though the pinion speed and material removal rate is similar during the grinding process, K220 pinion experienced high intensities of thermal damage on most of the tooth when compared to A651 BN signals. This explained about the lack of experimental analysis on the grinding coolant flow, its direction towards the pinions and towards the grinding wheel. Even though the macro-etch process of tooth 4 with 125 MP value doesn't show any discolouration which basically explains the absence of burn, the residual stresses have been altered by the introduction of tensile residual stresses at the surfaces due to the thermal damage. This clearly indicates that BN analysis is capable to identify the pinions with slight microstructural or stress state variation. With the ISO 14104 nital etch standard, the beginning phase of thermal damage is never identified. The exact temperature distribution with respect to the Barkhausen noise analysis is not examined and is still a potential question.

The hardness depth profile, microstructure and retained austenite fractions are in the normal range for 125 MP BN signal except for the presence of tensile residual stresses until 0.3 mm depth. The tooth 8 with 165 MP value showed a dark-etched microstructure indicating the over-tempered burn. From the x-ray retained austenite measured in figure 5.24 (**c**), the retained austenite fraction is in decreasing order indicating the decomposition of the γ_R phase. As observed in the microstructure, the white colour retained austenite is not observed in high fractions and it's been clear with the x-ray measurements about the decomposition of the γ_R phase from 25% RA observed in A651 sample to 12.9 $\pm$ 2 %. From the literature, it is known that the decomposition of retained austenite into a mixture of ferrite and cementite phases occurs between the temperature range of 200° C to 300° C [61]. figure 5.22 (**c**) illustrates the carbide precipitation between the martensite plates and appear to be spherical in shape. As the carbon atoms migrate from the tempered martensite structure to the retained austenite, during the over-tempering in the grinding process, the enhanced carbon percentage in the retained austenite increases its thermal stability. The martensite peak shape changes during the tempering process to become sharper representing the decrease in the martensite crystalline and this behaviour is observed in figure 5.25 martensite/ferrite (200) peak in tooth 8 with 165 MP.

The re-hardening burn is the consequence of the surface layer transforming above the austenitization range and its subsequent quenching forming untempered martensite. Due to the high localized pressure of the abrasive grains exerting on the pinion, the austenitization temperature is shifted towards a lower region [45]. The heating rates and cooling rates are so high that the transformation takes place in a few seconds of the contact between the grinding wheel and pinion tooth flank. For the 0.68% carbon at the surface, the para-equilibrium thermocalc calculations estimated about 740° C as the austenitization range. The grinding process heating rates are estimated as $10^{6\circ}$ C/s [44]. The formation of austenite from the tempered martensite involves the diffusion decay of tempered martensite which leads to the formation of α and Fe_3C structure and then further to austenite above the Ac1 range. As observed in the figure 5.23 (**a**), the re-hardened zone is only formed until the depth of 250μm followed by the tempered burn. This is particularly due to the heat flux generated at varying levels at the surface and subsurface regions. At the re-hardened zone, the temperature reaches to approximately around 800° C with heating rates around 1.3x10^6 - 1.1x10^{14} ° C/s for the martensite diffusion to occur and at the subsurface the temperature reaches to around 400 ° C with heating

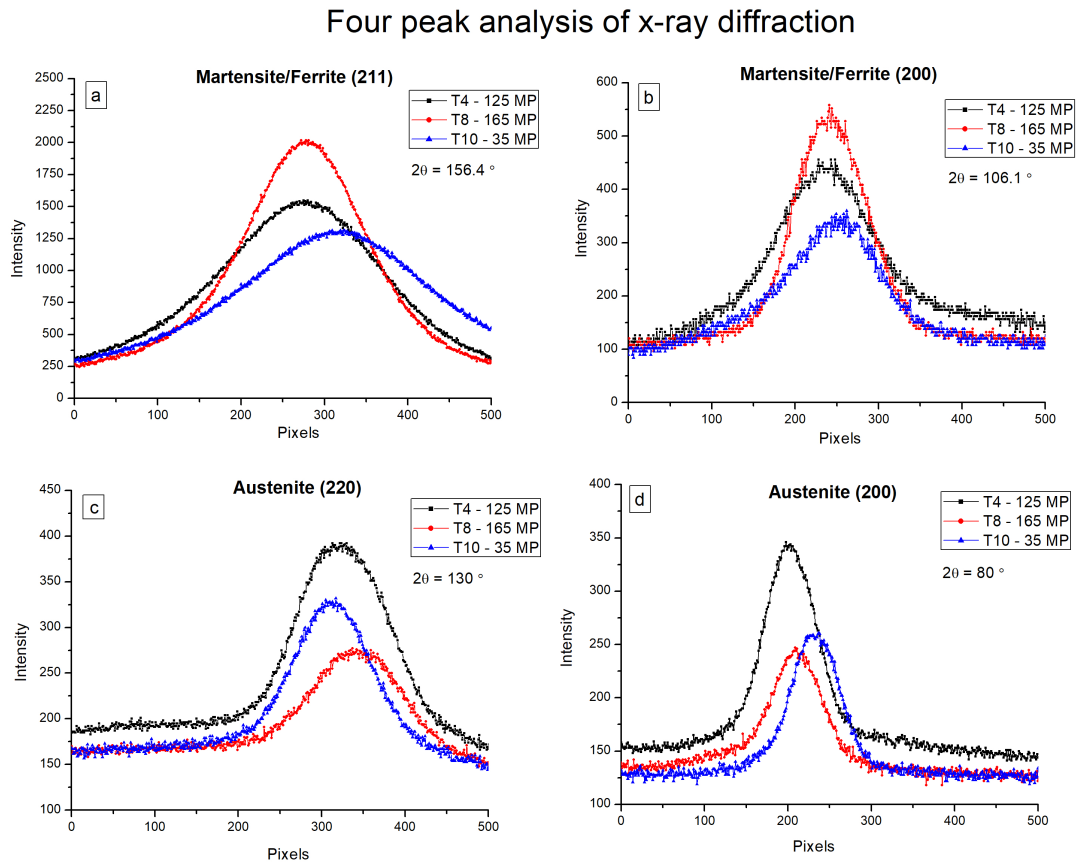

Figure 5.25: The x-ray intensities of martensite/ferrite (**a**) (211), (**b**) (200), (**c**) Austenite (220), (**d**) Austenite (200) peaks. Tooth 8 (165 MP) observed decreased retained austenite fractions in the both the diffraction planes signifying the RA decomposition

rates around 1.8x10^{6} - 1.6x10^{10} ° C/s [45]. The resultant microstructural features are observed in figure 5.23 (**b,c**). The Vickers hardness, microstructural features, retained austenite fractions, residual stresses and full-width half maximum (FWHM) results are totally in agreement with the Barkhausen noise high and low BN signal of 165 MP and 35 MP value respectively.

5.5. Part 3 : Characterization of axle tested pinions

The results of the axle test performed on the grinding induced burns are presented in this section. The material characteristics of the pinion before and after testing is summarized. 3 pinion are characterized and the results are plotted. Figure 5.26 illustrates the flow chart of the sample. P009 is the prototype pinion without burns and K041, K905 are pinions with grinding induced burns. The drive test indicates the pinions tested in the drive flank which makes the truck directs in forward direction. The coast test indicates the pinions tested on the coast flank where the truck directs backward. The grinding induced burn intensity of the pinion tooth tested are at a maximum of 140 MP values.

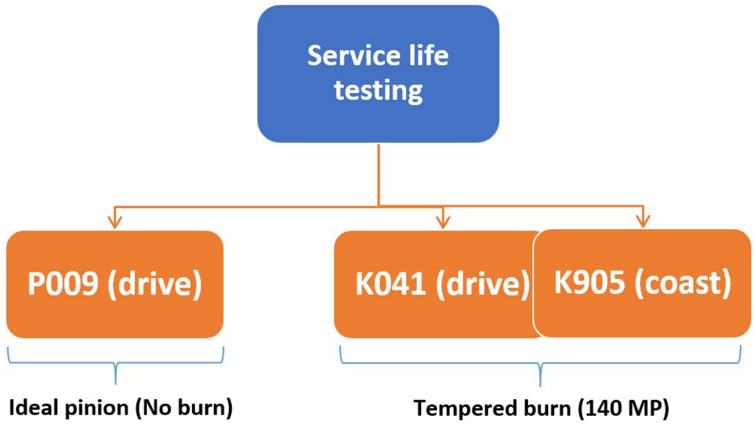

Figure 5.26: Flow chart of the pinions tested for service life. P009 (drive), K041 (drive) and K905 (coast)

5.5.1. Axle test-rig results

The axle test is performed on K041 and K905 pinion with a Barkhausen noise intensity 140 MP as maximum. The table 5.2 represents the test parameters and the results obtained. The required time and load cycles indicate the 100% life without accounting statistics, confidence limit and a number of test pieces. The run time represents the actual running time of pinion in the test rig. The P009 sample runs for 655 hours and K041, K905 performed for 345.2 hours. The truck design torque is 46000 Nm, but the pinion reference torque is 19558 Nm after dividing the design torque with 2.40 gear ratio to calculate the reference level for the pinion. The test has been stopped to prevent the damage caused by bearing failure on the pinion tooth flank. As this damage affects the pinion test data to interpret and characterize the pinion material with grinding induced burns.

The figure 5.27 represents the tooth face damage plot with torque on the y-axis and load cycles on the x-axis. The positive torque indicates the drive test and the negative torque represents the coast test. The figure has two plots representing K041 (drive) and K905 (coast) in 1 picture and P009 (drive) pinion in another image. The red dots indicate the test results as pointed by the arrow. The uncorrected SN - curve with a K-factor of 12 for pitting failures is represented by red dotted lines. The straight red line is the corrected SN-curve (corrected with spread, confidence level, number of test pieces and the probability of failure) and the requirements are represented by the blue straight lines. The blue dotted lines simulate the load spectra of 95% vehicle.

As observed, the grinding burn pinions K041 and K905 also survived the lifetime test. From figure 5.27 it is clearly seen that the run-time of the pinions is greater than the required time. When compared with the pinion P009 which has run for 655 hours, the surface of the pinion didn't observe any severe micropitting as observed in K041 and K905 9figure 5.31. The gear oil during the tests is maintained at 80° C.

Pinion	Req. time (h)	Req. load cycles	Run-time (h)	% of 46 kNm	Pinion torque (Nm)	Pinion speed (rpm)	Stress (N/mm^2)
P009	150.3	3155398	655	55	10,542	355	1676
K041	158.4	3325978	345.2	55	10,542	355	1676
K905	45.6	1555005	345.2	-34	-6588	568	1708.3

Table 5.2: DAF Trucks axle test parameters

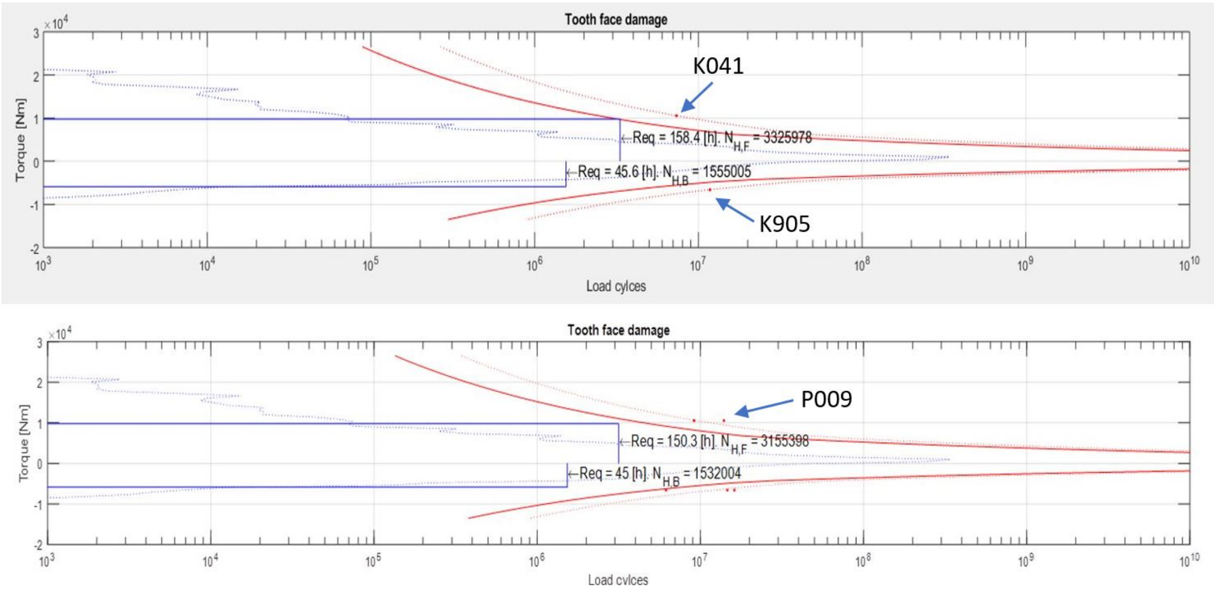

Figure 5.27: Test results of axle test rig experiments performed on P009 (drive), K041 (drive) and K905 (coast).

5.5.2. Barkhausen noise analysis

The Barkhausen noise signals from the P009 after drive axle testing is plotted in figure 5.28(**a**). For the ideal pinion, the BN signals as observed don't scatter much and all the drive tooth are in the range between 65 MP to 80 MP values which is quite normal and excellent for the truck functionality.

The K041 and K904 BN signal detection before and after the axle test is showed in figure 5.28 (**b,c,d,e**). The K041 pinion as shown in figure 5.28 (**b,c**) before testing has MP value scattering from 65 MP to 140 MP at 65% flank length and after the testing, all the tooth signals has the value below 100 MP indicating an increase in hardness and introduction of compressive residual stresses due to the retained austenite transformation to martensite structure.

The K905 pinion as shown in figure 5.28 (**d,e**), before testing has a lot of scattering in the tooth with the uniform pattern along the flank and after the -34% torque test, the BN signals don't change a lot but shows a compressed signal behaviour at 50% length of the flank indicated in the box of the figure 5.28 (**e**).

Further analysis is performed on K041 tooth 11 to study it's after test properties. The tooth 11 initially has 140 MP BN signal and after performing the axle test, the MP value showed a 34% decreasing rate to 90 MP at 60% length of the flank as shown in figure 5.29.

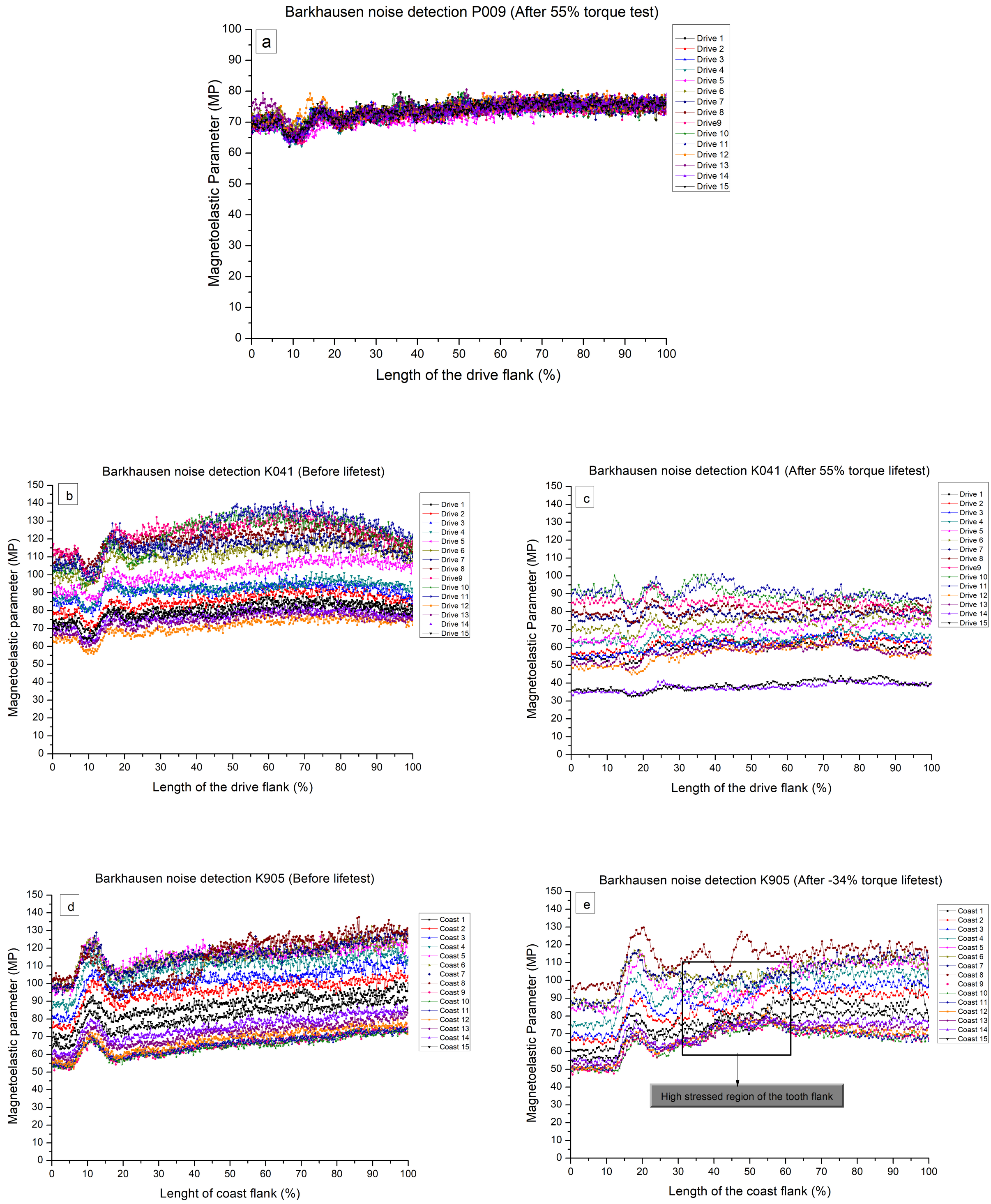

Figure 5.28: Barkhausen noise detection on drive side of P009, K041 pinion and coast side of K905 pinion. (**a**) P009 BN signals after axle test, (**b**) K041 BN signals before axle test, (**c**) K041 BN signals after axle test, (**d**) K905 BN signals before axle test, (**e**) K905 BN signals after axle test and the black square box indicating the high stressed zone of the flank where all the signals trying to compress sue to the applied stress

5.5.3. Surface analysis

The surface roughness profile on the 3 pinions is performed using KLINGELNBERG precision measuring centres (P65) machine. The Rz in microns of the pinion tooth is measured and shown in

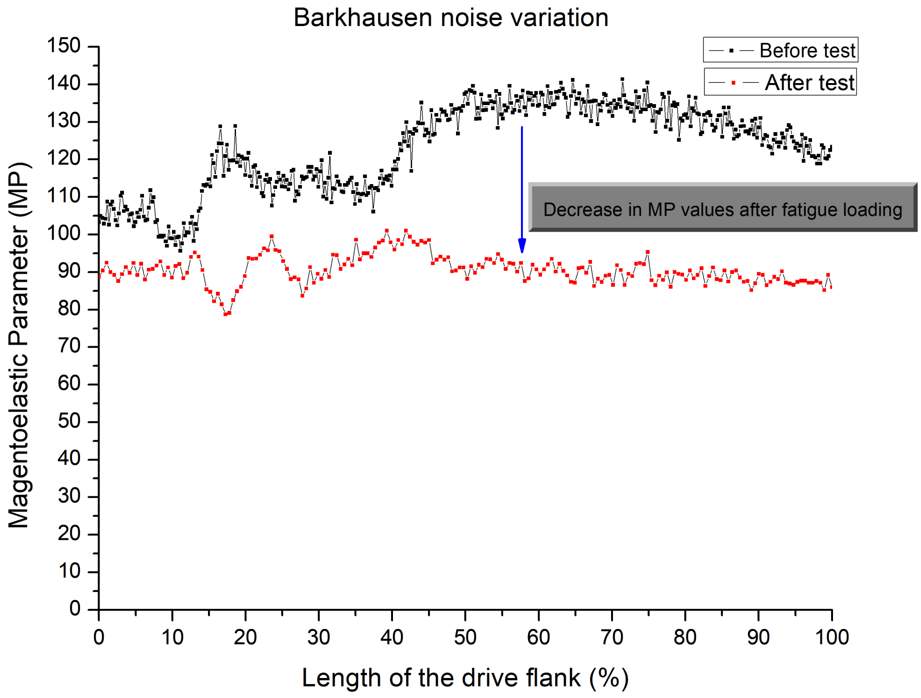

Figure 5.29: Tooth 11 Barkhausen noise signal of K041 drive tested pinion.

figure 5.30. The grinding induced burn K041 doesn't affect the roughness properties and is inside the limit of 6 microns. The ideal pinion P009 even after the testing shown safer limit and on the other side, the grinding induced burn pinion after the axle test showed higher roughness levels (Rz) indicating the micropits formation even after the successful life test. The tooth 11 with high MP value has the roughness of Rz = 3.65 microns and after the drive axle test, it increased to Rz = 10.77 microns. Even though the pinions survived the life test, the surface damage is observed on the soft tempered burn tooth.

Figure 5.31 shows the tooth flank of P009 and K041 pinion. The P009 pinion after the test produce a shiny surface and as observed the surface roughness (Rz) values are below 5 microns as shown in figure 5.31 (**a**). The K041 grinding induced burn pinion after the test observed the micropitting mostly near to the beginning of the contact region. At the end of the contact region, the pinion observed wear with scratches visible on the surface as observed in figure 5.31 (**b**).

The SEM images of the two pinions P009 and K041 are shown in figure 5.32. As observed, the micropitting is not observed particularly on P009 tooth surface due to its excellent 5 cycle grinding process which involves low temperature grinding and better surface topography. On the other hand, K041 grinding induced burn pinion experienced a large pitting surface area when compared to P009 due to its abusive grinding conditions. The formed micropits are only towards the longitudinal direction.

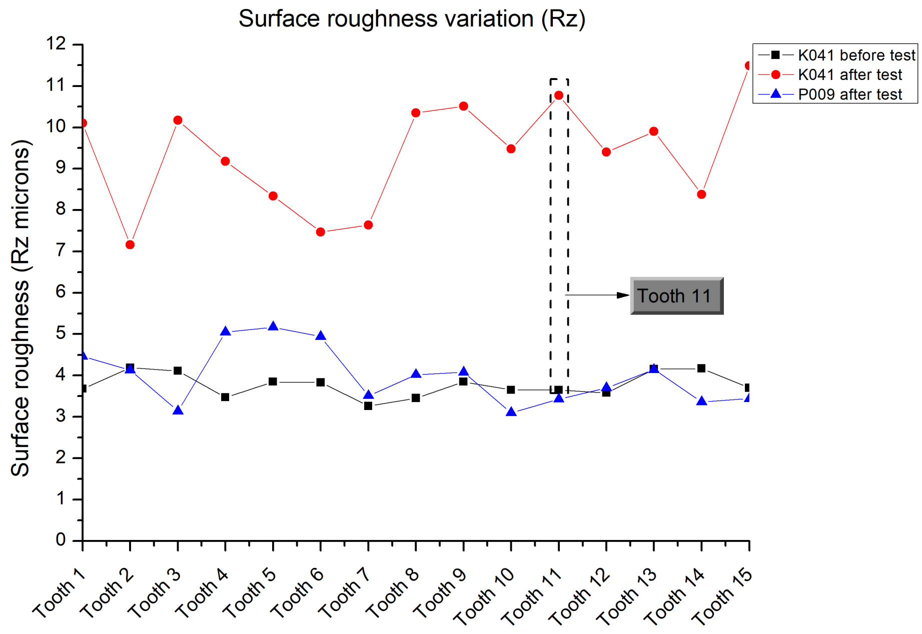

Figure 5.30: Surface roughness measurement (Rz) analysis on P009 (after), K041 (before and after) drive testing

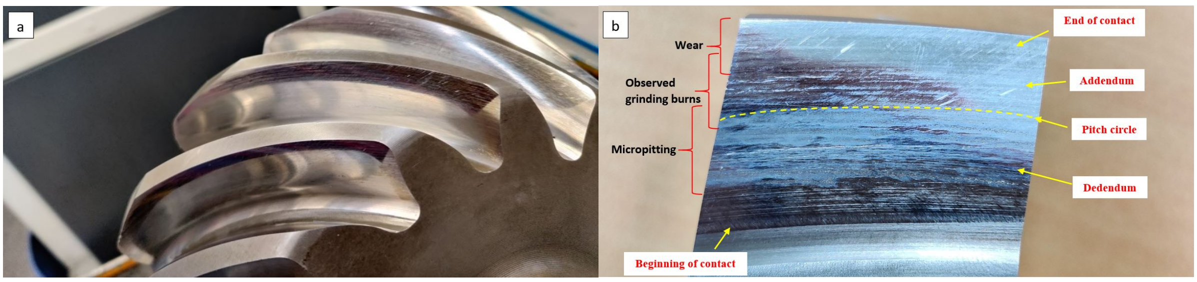

Figure 5.31: Macro inspection of P009 and K041 after drive testing. The visible contact pattern is observed on the two pinion surfaces. (**a**) P009 sample after the drive test. The surface looks shiny at the contact zone without any observed micropitting, (*b*) K041 drive tested pinion with observed micropitting and wear.

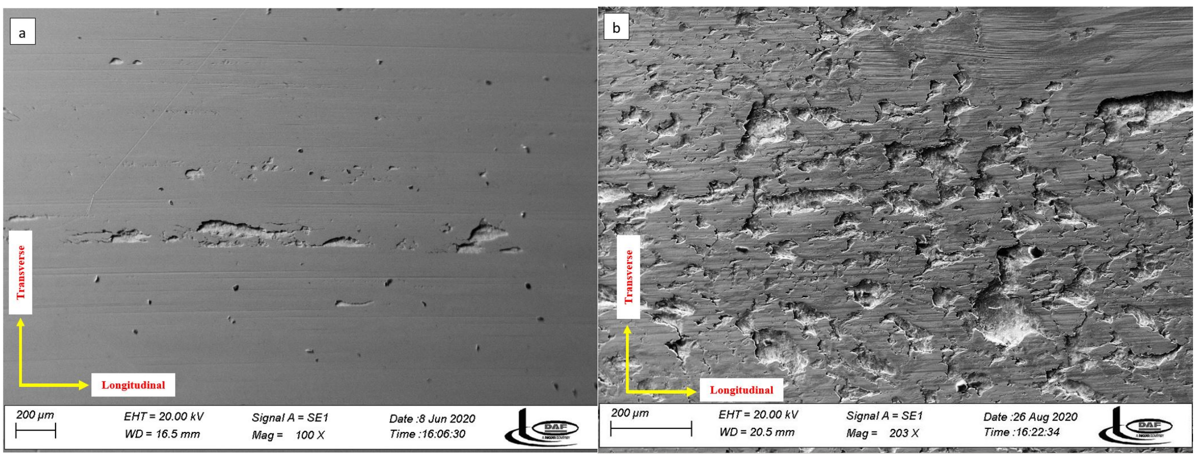

Figure 5.32: SEM image of the pinion surfaces after performing the drive axle test. The observed pitting is along the longitudinal direction. (**a**) P009 pinion tooth flank, (**b**) K041 pinion tooth flank.

5.5.4. Vickers hardness

The hardness depth profile of the 140 MP BN signal of another sample is compared to the tooth 11 140 MP → 100 MP after testing as shown in figure 5.33. The increase in hardness at the subsurface region is observed until 0.5 mm depth. At the 0.1 mm depth, the hardness increased from 621 HV1 to 676 HV1. The stress-induced transformation of retained austenite behaviour is particularly observed.

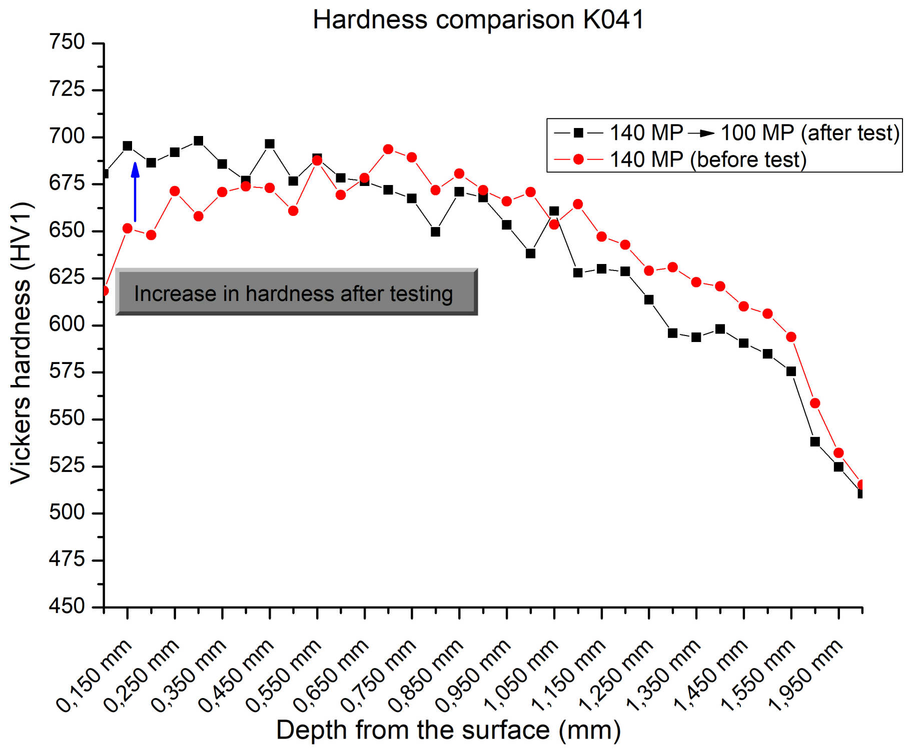

Figure 5.33: Vickers hardness depth profile comparison of before and after axle drive test of grinding induced burn sample

5.5.5. Microstructure analysis

The microstructural features of P009 and K041 pinion after the axle testing is studied in this section. P009 sample is shown in figure 5.34 (**a**) and the microstructure comprises of tempered martensite and few volumes of retained austenite fractions. The light/dark grey indicates the tempered martensite and the white colour indicates the retained austenite fractions. Figure 5.32 (**b**) sample is cut in transverse direction to evaluate the depth and angle of micropitting. The crossectional view of K041 sample is shown in figure 5.34 (**b,c**). The optical microscope image of K041 reveals the micropits generated in the plastically deformed region if tempered martensite as shown in figure 5.34 (**b**). The micropits initiate the surface or subsurface and grow at a certain angle to the surface into the material. The plastically deformed region is observed until the depth of 20 - 30 μ m into the material with pits forming into less than 10μ m depth. The SEM image of K041 in figure 5.34 (**c**) reveals the crack branching into the material.

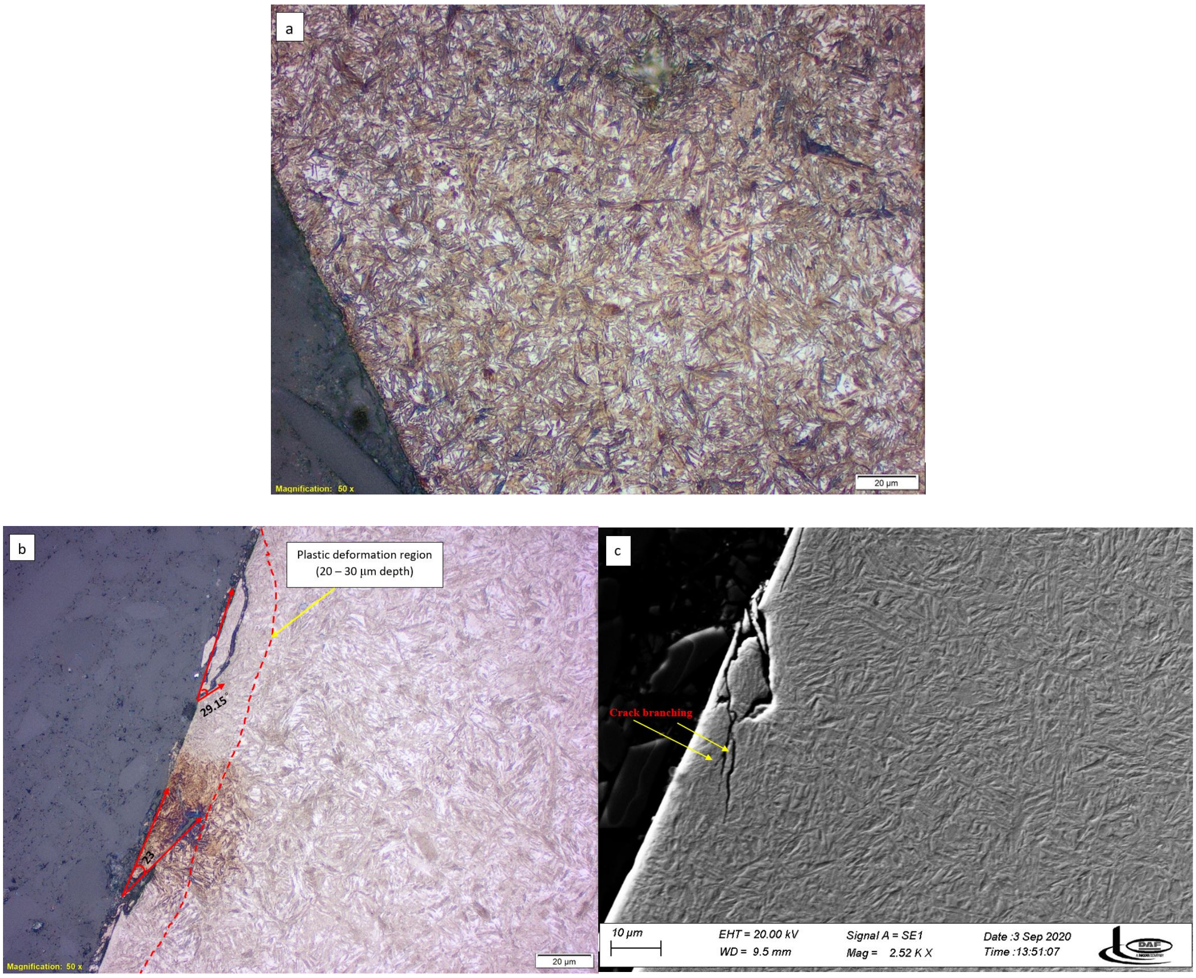

Figure 5.34: (**a**) Optical microscope image of P009 sample, (**b**) Optical microscope image of K041 sample. 2 micropits of depth less than 10μ m is observed with angles of 23° and 29° from the surface. The red dashed line indicates the zone of plastic deformation region, (**c**) SEM image of micropitting crossection. The depth of the pit is around 10μ m and the branching of cracks is also visible.

5.5.6. X-ray diffraction

The x-ray diffraction analysis of the P009 and K041 drive tested pinions are performed and plotted in figure 5.35 (**a,b**). The K041 grinding induced burn pinion 140 MP after testing shows high compressive stress until 0.3 mm depth into the surface. At the surface -600 ± 6.8 MPa is present. Basically as observed from figure 5.24 (**a**), the tensile residual stresses are present at the surface of 125 MP, so when analyzed 145 MP value should have higher tensile stresses at surface and subsurface due to the high intensity of the grinding burn. But during the testing, the unstable retained austenite has transformed to martensite generating high compressive residual stress until 0.3 mm and from that point, tensile residual stresses are presented. In figure 5.35 (**b**), the retained austenite fractions at surface is 9.5 ±1.6% and below 20 % until 0.3 mm generating compressive residual stresses as per the RA transformation fractions. The ideal P009 after the axle test has also generated -611 ± 11.3 MPa compressive residual stress but only at the surface. From the 0.01 mm depth, the compressive residual stress just normal between -100 MPa and -10 MPa until the 0.1 mm depth. This is also in line with the lower retained austenite fraction of 17.2 ± 1.3 % at the surface and maintaining around 25 ± 3% RA fraction until 0.1 mm.

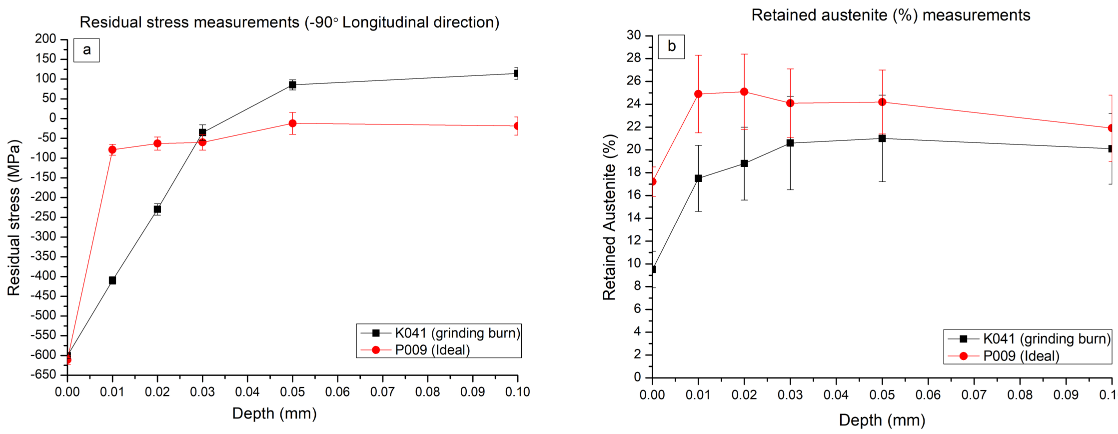

Figure 5.35: (**a**) Residual stress and (**b**) retained austenite depth profile of drive tested pinion P009 and K041

5.6. Part 3 : Discussion

The section discusses the characteristics of the fatigue tested grinding induced burn pinions. The Barkhausen noise analysis resulted in the lowered MP values after 345.2 hours of testing with 10,542 Nm torque on the drive side and -6588 Nm torque on the coast test. The maximum stress applied on the drive flank is 1676 Nmm^2 and coast flank is 1708.3 Nmm^2 at the pitch. The K041 pinion is loaded for around 6x10^6 cycles and K905 pinion loaded for 10^7 cycles. P009 pinion is loaded on the drive side with around 10^7 cycles. As observed in the figure 5.32 (**a**), the ideal pinion P009 without grinding induced burns, hasn't experienced any surface or subsurface damage. But the pinion K041 observed the micropitting on the surface as seen in figure 5.32 (**b**). The lowered BN signals observed after the fatigue testing indicating the microstructural variation or much higher compressive residual stresses at the surface and sub-surface region. But as understood, the Barkhausen noise signals only give qualitative information but no quantitative data about the hardness and residual stress information. So the material characterization analysis is performed on tooth 11 with 140 MP before the drive test and later detected with 100 MP value. The observed increased values of hardness are due to the transformation of the retained austenite into deformation-induced martensite. This result is confirmed with the residual stress and retained austenite measurements using x-ray diffraction in figure 5.35. The surface observed high compressive residual stress due to the retained austenite transformation by the application of load.

As observed in grinding induced burn sample K041, micropitting is recognised on the lower part of the gear tooth flank which is called as dedendum and it is known to be the common failure in gear rolling sliding contact behaviour. The negative sliding in the dedendum region is the reason for the micropitting initiation [60]. The initiation of micro-cracks occurs at the surface or subsurface region opposite to the pinion sliding direction and follows to grow into the surface at an angle again until the surface to form a pit[46]. The size of the pits are in order of 10 or 20μ microns as observed in figure 5.34 (**b,c**).

The observed plastic deformation is observed predominantly in the dedendum region of the gear tooth where the micropitting is severely seen in figure 5.34 (**b**). The high plastic deformation region is observed for K041 with 6x10^6 cycles than P009 ideal pinion which has loaded for 10^7 cycles. The crossectional analysis of the K041 observed the association of the micropitting in the plastic deformation region. The 140 MP grinding induced burns hasn't affected the service lifetime but has observed micropitting at 345.2 hours where the P009 with similar loading conditions and 655

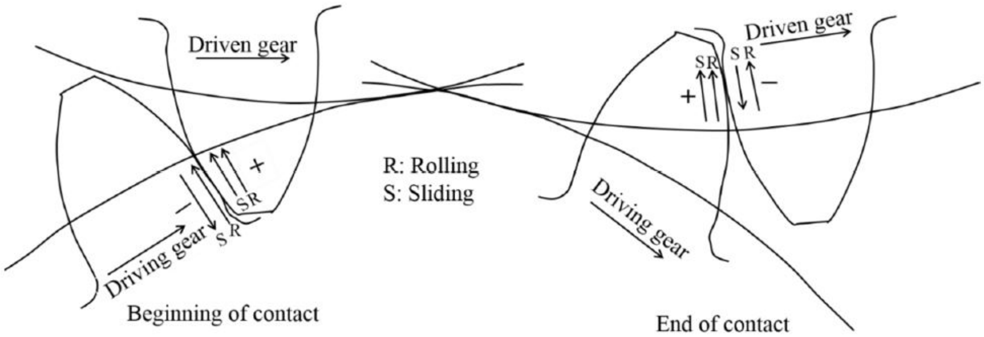

Figure 5.36: Pinion and gear contact regions at the beginning and end of contact. At the beginning of the contact, the driving gear is the pinion and the negative sliding is observed below the pitch circle which is the dedendum region [25]

hours running time hasn't damaged the pinion surface. The observed surface roughness (Rz) of the K041 pinion tooth is around 4μ m before the test and after the test, it measured 11μ m on tooth 11. So the ground gear observed irregular surface asperities and the observed asperities begin to plastically deform in the sliding directions and when the asperities couldn't afford to further plastic deformation, the crack begins to initiate at the subsurface region in plastic deformation region at a particular angle [68]. In the K041 it is measured to be 29° and 23° to the surface. Then the crack begins to propagate at a lower velocity towards the surface. At the similar time, due to the tensile stresses on the tooth surface and soft tempered burn microstructure, the surface cracks initiate and propagates downwards and at the contact of both the crack regions, the micropits formed [68] [39].

As the test is done continuously for the running time hours, it was difficult to observe the beginning of the micropitting formation on the surface. As the retained austenite transformation introduced compressive residual stresses due to the volume expansion at the surface and subsurface until the depth of 0.03 mm, the contact fatigue resistance intends to develop stopping the pinion to failure before the required time. The martensite formation increased the hardness and wear properties stopping the propagation of cracks. However the TEM investigation is needed to observe the true morphology of the plastically deformation region as with SEM and optical microscope, the morphology is not been clearly observed.

The high cyclic loaded pinion P009 with 10^7 cycles, the transformation of retained austenite only occurred at the surface level and from the depth of 10μ m, the normal level compressive residual stresses are observed. The mechanical stability of the retained austenite has a major role in this process. During the low temperature grinding process as it is in the region of 1st stage tempering step (80° C - 200° C), the martensite solid solution carbon contents decrease and as a result, the compressive stress on the retained austenite is reduced which leads to the reduction of mechanical stability[55]. As the P009 pinion lies in the 1st stage tempering region, the RA mechanical stability is decreased only at the surface and the rest of the RA fractions present inside the surface is stabilised and needs much higher activation energy for the phase transformation to occur. In the case of K041 pinion, the over tempering process has occurred and few fractions of retained austenite at the burn sites become relaxed and mechanically unstable as the martensite loses its trapped carbon from the BCT phase. So until the depth of 0.03 mm from the surface, with lower loading cycles compared with the P009 pinion, large fractions of retained austenite transformation is observed and subsequently resulted in the increase of hardness and compressive stresses.

5.7. Barkhausen noise correlation

The correlation of the Barkhausen noise with the Vickers hardness, residual stress and retained austenite is illustrated to identify the safe limits for the DAF production site. 6 samples data out 9 are used in this analysis. The other 3 are the fatigue tested pinion samples, where the stress-induced transformation generates BN signal in relation to the load cycles, transformed retained austenite. The x-axis represents the pinion numbers followed by the Barkhausen noise MP values. Figure 5.37 (**a**) illustrates the Vickers hardness trend with the increasing Barkhausen noise values. The BN signals generate low MP values for the harder structures. But as seen in the figure 5.37 (**a**) for W466, V431 and A651, the hardness observed is in the allowed acceptable limit between 660 HV1 and 750 HV1. But the BN signal increases with the increased hardness for these 3 samples which contradicts the Barkhausen principle. Actually, BN generated signals are influenced by both the microstructure and residual stress state of the material. So in the figure 5.38 observed, for the 3 samples W466, V431 and A651, compressive residual stresses are influencing the BN noise signals by generated low signal amplitude for the highest compressive stress state. As the compressive stress state begins to relax and rises towards tensile stress state, the BN MP values begin to rise. This is in relation to the Barkhausen principle. As the signals begin to cross 100 MP, the BN MP values are in correlation with hardness and stress state by indicating the observed lower hardness and increased tensile residual stresses. Even though the re-hardened zone generates compressive residual stresses at the near-surface and exhibits higher hardness features due to formation of untempered martensite, the sample is rejected due to its brittle nature and lower toughness. But the service lifetime test of the re-hardened zone is not done to exactly understand its failure behaviour. As shown in figure 5.37 (**b**), the relation with Barkhausen noise with the retained austenite fraction theoretically doesn't work due to the fact that the Barkhausen noise signals only affects the ferromagnetic materials, but the austenite being FCC paramagnetic phase, the conclusive relations cannot be drawn.

As the grinding process temperature exceeds the tempering heat treatment stage of the sample which is 210° C, the reduction of carbon content is observed in the martensite phase. The increasing temperature is related to a decrease in hardness below the austenitizing temperature due to the reduction in dislocation density and generation of softer phase like α ferrite. The magnetic domain walls in the softer structure, move easily without any pinning sites obstacles generating high BN signal amplitude [32].

Even though the 125 MP is mentioned in the safe limit zone by considering the hardness, when it comes to tensile stress state condition, it is not considered to be in the safe zone. So the BN signals generating between 50 MP and 100 MP is considered to be a safe signal profile taking into considerations of residual stresses and hardness values.

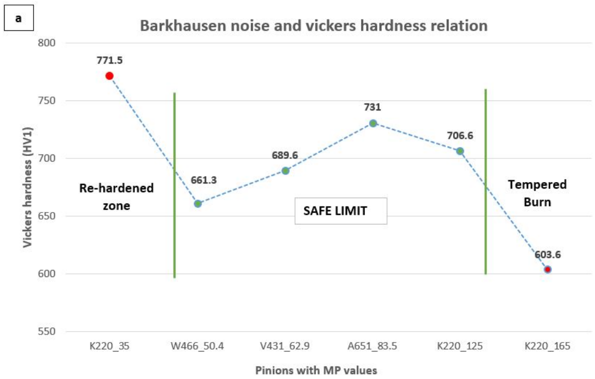

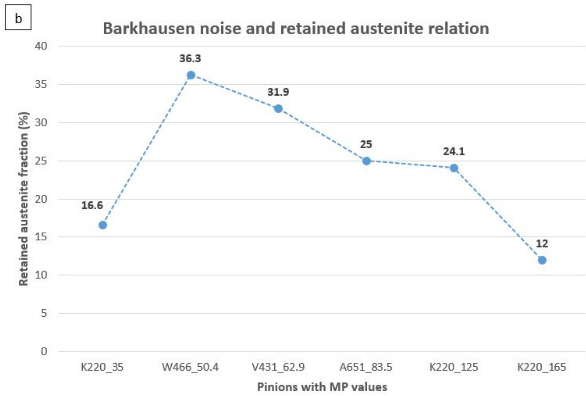

Figure 5.37: (**a**) BN relation with vickers hardness at 0.1 mm depth, (**b**) retained austenite relation with BN signals at 0.020 mm depth from the surface

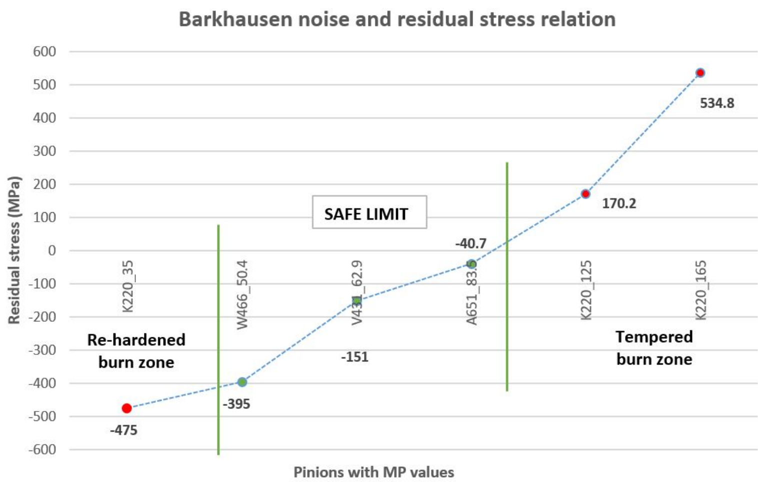

Figure 5.38: BN signals relation with XRD residual stresses at 0.020 mm depth from the surface

6

Conclusions and Recommendations

6.1. Conclusions

The conclusions of this thesis will be presented in this chapter based on the research questions which were defined in Chapter 3

Part 1: How the different grinding parameters are effecting the material deformation and the generation of grinding induced burns?

- The variation of drive and coast BN signal intensity of heat treated furnace sample W466 is due to the amount of martensite formed during quenching process as it affects the microstructure and residual stress state which influences the BN signal.
- The 2 cycle grinding process with the 4.5 °/s and 3.5°/s resulted in high intensity Barkhausen noise signals compared to the 3 cycle process with 3.75 °/s, 3.75 °/s, 3.25 °/s due to high localized heat generation.
- Plastic deformation caused due to 2 cycle grinding process near the surface increased the hardness properties but observed the relaxation of compressive residual stresses in comparison with the 3 cycle process.
- However, the increase in pinion speed and reducing grinding cycles didn't generate grinding induced burns but the process is favourable in generating as observed in high BN signal intensity values.
- The rise in thermal damages are not completely dependent on pinion speed and grinding cycles but the collective factor of all the grinding parameters. The similar 2 cycle process generated tempered and re-hardened burn previously, but not observed now. It is clearly indicating the effect of other grinding parameters including depth of cut, coolant flow rate and flow direction.

Part 2: Investigating the material characteristics of the different intensities of tempered and re-hardened grinding burns and set an accepting safe limit of Barkhausen noise signals

- The microstructural characterization of 125 MP observed the required hardness depth profile until 1.9 mm, no discolourations during the nital etch process but the X-ray diffraction measurement at surface observed tensile stresses of 90.8 ± 7.1 MPa indicating the beginning of thermal damage.
- Retained austenite decomposition is observed on tooth 8 with 165 MP Barkhausen signal indicating the second stage of tempering with temperature rise to 300° C and the hardness profile damaged is observed until the depth of 1.5 mm. The 10% reduction of RA fraction is noticed using X-ray diffraction technique. The hardness at 0.1 mm is dropped to 603.6 HV1 indicating the softer microstructure.
- The re-hardened zone is identified with 35 MP Barkhausen noise signal with a hardness of 771.5 HV1 at 0.1 mm depth. The freshly formed brittle structured plate martensite generates compressive stress of -446.5 ± 10 and retained austenite fraction of 20.6 ± 0.5 %. The abusive grinding process generated 250 μ m re-hardened zone at the surface followed by 400 μ m depth tempered burn with hardness below 550 HV1 observing 3rd stage of tempering by carbide precipitation.
- The Barkhausen noise signals between 50 MP and 100 MP is considered to be the accepted safe limit for the grinding induced burn detection technique based on the experimental results.

Part 3: How the grinding induced burn microstructure is initiating the micropitting and affecting the fatigue lifetime of pinions

- The service lifetime testing of drive and coast pinions with a tempered burn intensity of 140 MP Barkhausen signal was successful without any breakage observed. The micropitting is observed at the dedendum region of the pinion where the contact begins.
- The BN signal on K041 sample after service testing reduced from 140 MP to 100 MP with observed microstructural and residual stress variation due to the retained austenite transformation to martensite. The transformation increased the hardness from 620 HV1 to 676 HV1 and the volume expansion created compressive residual stress until the depth of 0.03 mm from the surface which eventually increased the contact fatigue resistance.
- The micropitting is initiated in the plastic deformation region and crack branching is developed due to the varying stress field at a certain depth from the pinion/gear contact.

6.2. Future recommendations

Based on the present research on grinding-induced burns, the following interesting possibilities can be explored for further research:

- The thermal modelling of the grinding operation can be done to study the temperature rise, heating rates and cooling rates in the short span of the contact zone of grinding wheel and pinion. This will help to determine the maximum grinding zone temperature, moving heat source and able to vary the parameters as per the grinding requirement.
- The service lifetime testing with 100% torque is to planned for the grinding induced burn pinions to analyse the bending failure and study the fracture behaviour.

Bibliography

[1] Temperatures in high efficiency deep grinding (HEDG).

[2] Stresstech Group/Rollscan 350. *Operating instructions, V.2.0*, (February), 2018.

[3] 3M. Gear grinding handbook. 2014.

[4] K W Andrews. JISI. (203):721, 1965.

[5] R. Atraszkiewicz, B. Januszewicz, Ł. Kaczmarek, W. Stachurski, K. Dybowski, and A. Rzepkowski. High pressure gas quenching: Distortion analysis in gears after heat treatment. *Materials Science and Engineering A*, pages 550–557, 2012.

[6] HS Avner. Introduction to physical metallurgy. *Tata McGraw-Hill*, 2002.

[7] Jeffrey A Badger and Andrew Torrance. Burn awareness. *Cutting Tool Engineering*, 52(12):40, 2000. ISSN 00114189.

[8] G. Badinier, C.W. Sinclair, S. Allain, F. Danoix, and M. Gouné. *The Mechanisms of Transformation and Mechanical Behavior of Ferrous Martensite.* Number January 2016. 2017.

[9] A C Batista, A M Dias, J L Lebrun, J C Le flour, and G Inglebert. Contact fatigue of automotive gears : evolution and effects of residual stresses introduced by surface treatments. pages 217–228, 2000.

[10] E Brinksmeler and A Glwerzew. Chip Formation Mechanisms in Grinding at Low Speeds. *CIRP Encyclopedia of Production Engineering*, 52(1):253–261, 2003.

[11] E.; Dehner and F Weber. Experience with Large high-Speed Load Gears. *GearTechnology*, pages 42–52, 2007.

[12] Murat Deveci. Grinding Residual Stresses.

[13] Song Ding, Guiyun Tian, and Ruslee Sutthaweekul. Non-destructive hardness prediction for 18CrNiMo7-6 steel based on feature selection and fusion of Magnetic Barkhausen Noise. *NDT and E International*, 107(July 2018):102138, 2019.

[14] E.C.Bain. Trans. AIME,. 70(25), 1924.

[15] Fernandes. High cycle and impact fatigue behavior of carburized steels. *Engineering Failure Analysis*, 3(3):219, 1996.

[16] Andrew Freborg. Investigating and understanding the role of transformation induced residual stress to increase fatigue life of high strength steel used in transmission gears. 2013.

[17] Robin Frisk. Distortion Analysis of Low Pressure Carburized Components. 2016.

[18] P.Q. Ge, J.F. Li, C.H. Lu, and Z.C. Liu. Performance evaluation and action mechanism analysis of extreme pressure additives used for oil-based cutting fluids. *Key Engineering Materials*, pages 281–286, 2003.

[19] C Gorgels and F Klocke. Influence of the Process on the Material Properties in Gear Profile Grinding and its Detection using Barkhausen Noise Analysis. *Proceedings of the 5th International Conference on Barkhausen Noise and Micromagnetic Testing*, 2005.

[20] G. Gottstein. Physical foundations of materials science. *Springler Verlag*, 2004.

[21] G.R.Speich. Tempering of low-carbon martensite. *Transactions of the Metallurgical Society*, pages 2553–2564, 1969.

[22] J.R.C. Guimaraes and P.R. Rios. Quantitative interpretation of martensite microstructure. *Materials Research*, 14(1):97–101, 2011.

[23] Christian Güntner, Thomas Tobie, and Karsten Stahl. Alternative microstructures and their influence on mechanical properties of case-hardened gears. *Forschung im Ingenieurwesen/Engineering Research*, 81(2-3):245–251, 2017.

[24] Baofeng He, Cui'e Wei, Siyuan Ding, and Zhaoyao Shi. A survey of methods for detecting metallic grinding burn. *Measurement: Journal of the International Measurement Confederation*, 134: 426–439, 2019.

[25] Daniel H Herring. Gear Materials and their Heat Treatment. pages 1–8, 2020.

[26] Richard P. Vinci Hertzberg, Richard W. and Jason L. Hertzberg. Deformation and Fracture Mechanics of Engineering Materials. *Wiley*, 2013.

[27] V. Heuer, D. Faron, D. Bolton, M. Lifshits, and K. Loeser. Distortion Control of Transmission Components by Optimized High Pressure Gas Quenching. *ASM International*, pages 1833–1838, 2013.

[28] F. Hoffmann, O. Kessler, T. Lübben, and P. Mayr. Distortion engineering-distortion control during the production process. *Heat treatment of metals*, pages 61–66, 2004.

[29] R. A. Irani, R. J. Bauer, and A. Warkentin. A review of cutting fluid application in the grinding process. *International Journal of Machine Tools and Manufacture*, 45(15):1696–1705, 2005.

[30] S. Jermolajev, J. Epp, C. Heinzel, and E. Brinksmeier. Material Modifications Caused by Thermal and Mechanical Load during Grinding. *Procedia CIRP*, 45:43–46, 2016.

[31] D Jiles. Introduction to Magnetism and Magnetic Materials. *London: Chapman & hall*, page 536, 1998.

[32] Tan Jin, Jun Yi, and Siwei Peng. Determination of burn thresholds of precision gears in form grinding based on complex thermal modelling and Barkhausen noise measurements. *The International Journal of Advanced Manufacturing Technology*, pages 789–800, 2017.

[33] D. Ju, M. Sahashi, T. Omori, and T. Inoue. Residual stresses and distortion of a ring in quenching-tempering process based on metallo-thermomechanics. *ASM International*, 1996.

[34] O. Karabelchtchikova. Fundamentals of Mass Transfer in Gas Carburizing. *Worcester Polytechnic Institute*, 2007.

[35] B. Karpuschewski. Residual Stress Generation in Grinding Processes, in Lu J, (Ed.) Handbook on Residual Stress. *Society for Experimental Mechanics (SEM)*, pages 56–69, 2005.

[36] B Karpuschewski, O Bleicher, and M Beutner. Surface integrity inspection on gears using Barkhausen noise analysis. *Procedia Engineering*, 19(0):162–171, 2011.

[37] F Klocke. Manufacturing Process 2: Grinding, Honing, Lapping. *Springer-Verlag*, 2009.

[38] D. Koistinen and R. Marburger. A general equation prescribing the extent of the austenite–martensite transformation in pure iron–carbon alloys and plain carbon steels. *Acta Metall*, 7(1):59–60, 1959.

[39] Timothy Krantz and Brian Tufts. Pitting and bending fatigue evaluations of a new case-carburized gear steel. *2007 Proceedings of the ASME International Design Engineering Technical Conferences and Computers and Information in Engineering Conference, DETC2007*, 7:863–869, 2008.

[40] G. Krauss. Principle of heat treatment of steels. *American Society of Metals*, 1980.

[41] G. Krauss. Heat Treatment, Microstructures, and Residual Stresses in Carburized Steels. In *Quenching and Distortion Control Conference Proceedings*, pages 181–191, 1992.

[42] George Krauss. Microstructures and Properties of Carburized Steels. 4, 2014.

[43] P. Kula, K. Dybowski, E. Wolowiec, and R. Pietrasik. Boost-diffusion vacuum carburizing - Process optimisation. *vaccum*, 99:175–179, 2014.

[44] V Lebedev, N Klimenko, I Uryadnikova, T Chumachenko, and A Ovcharenko. TRANSFORMATIONS IN THE SURFACE LAYER AT GRINDING OF PARTS OF HARDENED STEELS. 2(21): 176–181, 2017.

[45] V.G Lebedev. Mechanism of formation of burns during grinding of parts from hardened steels. *Scientific notes*, (40):141 –144, 2013.

[46] Jacky Lesage and Didier Chicot. Role of microstructure and residual stresses on fatigue crack initiation of carbonitrided steels. 60(8), 1989.

[47] S Malkin. Grinding Technology – Theory and Applications of Machining with Abrasives. *Second edition Industrial Press*, 2008.

[48] S Malkin and C Guo. Grinding Technology: Theory and Application of Machining with Abrasives. *Industrial press*, 2008.

[49] AG Mamalis, J Kundrák, DE Manolakos, K Gyani, A Markopoulos, and M Horvath. Effect of the workpiece material on the heat affected zones during grinding: a numerical simulation. *International Journal of Advanced Manufacturing Technology*, 22:761–770, 2003.

[50] P. Mason and P. Prevéy. Iterative Taguchi Analysis: Optimizing the Austenite Content and Hardness In 52100 Steel. *Journal of Materials Engineering and Performance*, 10(1):14–21, 2001.

[51] Dana J Medlin, Bastiaan E Cornelissen, David K Matlock, G Krauss, and Raymond J Filar. Effect of thermal treatments and carbon potential on bending fatigue performance of SAE 4320 gear steel. *SAE Technical Papers*, (724), 1999.

[52] B. Moiseev, Y. M. Brunzel, and L. Shvartsman. Kinetics of carburizing in an endothermal atmosphere. *Metal Science and Heat Treatment*, 21(6):437–442, 1979.

[53] P V Morra. *Thermo-mechanical loading response of hardened and tempered iron-carbon based alloys.* 2004.

[54] R. Norton. Spur Gears. *Machine Design, An Integrated Approach*, 3:635–700, 2006.

[55] Xun Qiao, Lizhan Han, Weimin Zhang, and Jianfeng Gu. Thermal stability of retained austenite in high-carbon steels during cryogenic and tempering treatments. *ISIJ International*, 56(1): 140–147, 2016.

[56] A. K Rakhit. Heat Treatment of Gears : A Practical Guide for Engineers. *ASM International*, 2000.

[57] Luciana S Rossino, Danilo Borges Villarino de Castro, Jeferson Aparecido Moreto, Dirceu Spinelli, and José Ricardo Tarpani. Surface contact fatigue failure of a case hardened pinion shaft. *Materials Research*, 17(3):535–541, 2014.

[58] W Brian Rowe. Thermal Damage. *Principles of Modern Grinding Technology*, pages 113–122, 2014. doi: 10.1016/b978-0-323-24271-4.00007-5.

[59] W.B. Rowe and T. Jin. Temperatures in high efficiency deep grinding (HEDG). *Manufacturing Technology*, 50(1):205–208, 2001.

[60] Satyam S Sahay. Heat Treatment of Steel Gears. *Heat Treating of Irons and Steels*, 4:204–218, 2018. doi: 10.31399/asm.hb.v04d.a0005987.

[61] Leonard E. Samuels. Tempering of Martensite. *Metallography, Microstructure, and Analysis*, 3 (1):70–90, 2014.

[62] B. Schotsman. Spalling defects in mhh steel rails. 2017.

[63] T. Sourmail and C. Garcia-Mateo. A model for predicting the Ms temperatures of steels. *Comp.Mater.Sci.*, 34(2):213–218, 2005.

[64] Kiruthika Devi Sundarrajan. Study of Grinding Burn Using Design of Experiments Approach and Advanced Kaizen. page 57, 2012.

[65] Seyyed Hesamodin Talebi, Mohammad Jahazi, and Haikouhi Melkonyan. Retained austenite decom-position and carbide precipitation during isothermal tempering of a medium-carbon low-alloy bainiticsteel. *Materials*, 11(8), 2018.

[66] Z Tao, S Yaoyao, S Laakso, and Z Jinming. Investigation of the Effect of Grinding Parameters on Surface Quality in Grinding of TC4 Titanium Alloy. *Procedia Manufacturing*, 11, 2017.

[67] Thomas Tobie, Frank Hippenstiel, and Hardy Mohrbacher. Optimizing gear performance by alloy modification of carburizing steels. *Metals*, 7(10), 2017.

[68] Ryan M Wagar, John G Speer, David K Matlock, and Patricio F Mendez. Examination of Pitting Fatigue in Carburized Steels with Controlled Retained Austenite Fractions. 2006.

[69] Long Wang, Xiujian Tang, Liuying Wang, Nengjun Yang, Xiaohu Chen, Ping Li, Gu Liu, and Guohao Liu. Mechanism of grinding-induced burns and cracks in 20CrMnTi steel gear. *Materials and Manufacturing Processes*, 34(10):1143–1150, 2019.

[70] M.A. Zaccone, J.B. Kelley, and G. Krauss. Strain Hardening and Fatigue of Simulated Case Microstructures of Carburized Steels. *Industrial heating*, pages 38–51, 1989.